NASA CONTRACTOR REPORT

NASA CR-1967



# SPIN TEST OF TURBINE ROTOR

*by Michael H. Vavra, James E. Hammer, and Lawrence E. Bell*

*Prepared by*
NAVAL POSTGRADUATE SCHOOL
Monterey, Calif. 93940
*for*

NATIONAL AERONAUTICS AND SPACE ADMINISTRATION • WASHINGTON, D. C. • FEBRUARY 1972

| 1. Report No. | 2. Government Accession No. | 3. Recipient's Catalog No. |
|---|---|---|
| NASA CR-1967 | | |

| 4. Title and Subtitle | 5. Report Date |
|---|---|
| SPIN TEST OF TURBINE ROTOR | February 1972 |
| | 6. Performing Organization Code |

| 7. Author(s) | 8. Performing Organization Report No. |
|---|---|
| Michael H. Vavra, James E. Hammer, and Lawrence E. Bell | NPS-57VA71061B |
| | 10. Work Unit No. |
| 9. Performing Organization Name and Address | |
| Naval Postgraduate School<br>Monterey, California 93940 | 11. Contract or Grant No.<br>NASA Defense Purchase Request C-10836 |
| | 13. Type of Report and Period Covered |
| 12. Sponsoring Agency Name and Address | Contractor Report |
| National Aeronautics and Space Administration<br>Washington, D.C. 20546 | 14. Sponsoring Agency Code |

15. Supplementary Notes

Project Manager, Charles F. Zalabak, Chemical Rocket Division, NASA Lewis Research Center, Cleveland, Ohio

16. Abstract

This report presents experimental data of the tangential and radial stresses in the disks of the 36 000 horsepower, 4000 rpm turbine for the M-1 Engine Oxidizer Turbopump. The two-stage Curtis turbine is a special light-weight design utilizing thin conical disks with hollow sheet-metal blades attached by electron-beam welding techniques. The turbine was fabricated from Inconel 718, a nickel-chromium alloy. The stresses were obtained by strain-gage measurements using a slip-ring assembly to transmit the electrical signals. Measurements were made at different rotative speeds and different thermal loads. In addition to presenting test data, the report describes test equipment, design of associated hardware, test procedures, instrumentation, and tests for the selection and calibration of strain gages.

| 17. Key Words (Suggested by Author(s)) | 18. Distribution Statement |
|---|---|
| Turbine rotor; Concial disks; Inconel 718; Electron beam welds; Hot spin test; Centrifugal stress; Thermal stress; Slip rings; Strain gage; Thermocouple; Induction heater | Unclassified - unlimited |

| 19. Security Classif. (of this report) | 20. Security Classif. (of this page) | 21. No. of Pages | 22. Price* |
|---|---|---|---|
| Unclassified | Unclassified | 147 | $3.00 |

* For sale by the National Technical Information Service, Springfield, Virginia 22151

1. Turbine blades -- Effects of stress and strain

27 Jun 72

TABLE OF CONTENTS


I. SUMMARY . . . . . 1

II. INTRODUCTION . . . . . 2

III. HARDWARE DESCRIPTION . . . . . 4

A. TEST ROTOR . . . . . 4

B. EXISTING SPIN TEST FACILITY . . . . . 4

C. SPECIAL EQUIPMENT AND MODIFICATIONS . . . . . 7

1. Drive Turbine . . . . . 7

2. Rotor Suspension System . . . . . 8

3. Measuring and Balancing Rig . . . . . 9

4. Rotor Handling Rig . . . . . 10

5. Heating and Cooling Coils . . . . . 10

6. Calibration Beam . . . . . 11

IV. PRELIMINARY AND FABRICATION-EVALUATION SPIN TESTS . 12

A. INSTRUMENTATION . . . . . 12

B. PRELIMINARY SPIN TESTS . . . . . 13

1. Preparations and Test Procedures . . . . . 13

2. Test Results . . . . . 16

3. Spin Test for Fabrication Evaluation . . . . . 16

a. Test Preparation and Procedure . . . . . 16

b. Results . . . . . 17

C. DISCUSSION OF HUB-BOLT BEHAVIOR . . . . . 18

V. HIGH-TEMPERATURE INSTRUMENTATION . . . . . 20

A. STRAIN-GAGE SELECTION . . . . . 20

1. Gage Availability . . . . . 20

2. Tests for Gage Selection . . . . . 21

B. DETAILED EVALUATION OF SELECTED STRAIN GAGE . . 23

1. Signal Conditioning . . . . . 24

2. Gage Performance Evaluation at Ambient Temperature . . . . . 25

3. Gage Performance Evaluation at Elevated Temperature . . . . . 26

a. Evaluation of Apparent Strains . . . . . 27
b. Evaluation of Gage Stability . . . . . 28
c. Variation of Gage Factor with Temperature . . . . . 28
4. Summary . . . . . 29
C. DATA LOGGING SYSTEM . . . . . 30
D. INSTRUMENTATION OF TEST ROTOR . . . . . 31
VI. ROOM-TEMPERATURE SPIN TESTS . . . . . 33
A. EQUIPMENT CHANGES . . . . . 33
B. TEST PROCEDURE . . . . . 34
C. RESULTS AND DISCUSSION . . . . . 35
VII. ELEVATED-TEMPERATURE STATIC TESTS . . . . . 41
A. PREPARATION FOR TEST AND PRELIMINARY RUNS . . . 41
B. TEST PROCEDURES . . . . . 43
C. RESULTS AND DISCUSSION . . . . . 44
VIII. ELEVATED-TEMPERATURE SPIN TESTS . . . . . 50
A. TEST PROCEDURES . . . . . 50
B. RESULTS AND DISCUSSION . . . . . 51
IX. CONCLUSIONS . . . . . 52
X. REFERENCES . . . . . 99
APPENDIX A DESIGN OF SPECIAL EQUIPMENT . . . . . 100
A.1 Rotor Suspension System . . . . . 100
A.2 Measuring and Balancing Rig . . . . . 102
A.3 Rotor Handling Rig . . . . . 105
APPENDIX B STRESS CALCULATIONS . . . . . 109
B.1 Centrifugal Stress Due to Balance Weights. . 109
B.2 Stress Distributions in a Straight Replacement Model of the Second-Stage Rotor . . . . . 111
APPENDIX C HUB BOLT TEST PROGRAM . . . . . 124
APPENDIX D DRAWINGS . . . . . 132

LIST OF FIGURES


| Figure | | Page |
|---|---|---|
| 1 | Test Rotor Mounted in Measuring and Balancing Rig | 54 |
| 2 | Oxidizer Turbopump Assembly | 55 |
| 3 | M-1 Engine Mockup | 56 |
| 4 | Inner Face of Second-Stage Turbine | 57 |
| 5 | Strain Gage and Thermocouple Locations -- High-Temperature Instrumentation | 58 |
| 6 | Cross Section of Test Rotor in Spin Pit | 59 |
| 7 | Overall View of Hot Spin Test Facility | 60 |
| 8 | Hot Spin Test Unit Control Console | 61 |
| 9 | Test Rotor Supported in Handling Rig | 62 |
| 10 | Cross Section of Heating Coils and Hub Cooling Plates | 63 |
| 11 | Upper Heating Coil and Insulation Surrounding Test Rotor | 64 |
| 12 | Upper Hub Cooling Plate | 65 |
| 13 | Cantilever Beam Test Jig and Uniform-Stress Beam | 66 |
| 14 | Microdot SG-180 Gage Configuration | 67 |
| 15 | Standard Three-Wire Circuit Illustrating Lead-Wire Resistance and Input Conditioning | 68 |
| 16 | Mean Apparent Strain With Temperature Curve Based on Tests of Eight Gages Mounted on Calibration Beam | 69 |
| 17 | Typical Gage Installation (Microdot SG-180) on Rotor Disk | 70 |
| 18 | Thermocouple Circuit Showing Reference Junction Arrangement | 71 |
| 19 | Strain Data Scatter Bands for Typical Face-1 Gages | 72 |
| 20 | Averaged and Zeroed Strain Data for Typical Face-1 Gages | 73 |

| | | |
|---|---|---|
| 21 | Centrifugal Strains on First-Stage Disk at 4,000 RPM . . . . . | 74 |
| 22 | Centrifugal Strains on Second-Stage Disk at 4,000 RPM . . . . . | 75 |
| 23 | Dimensionless Centrifugal Stresses on First-Stage Disk . . . . . | 76 |
| 24 | Dimensionless Centrifugal Stresses on Second-Stage Disk . . . . . | 77 |
| 25 | Centrifugal Stresses on First-Stage Disk at 6,100 RPM . . . . . | 78 |
| 26 | Centrifugal Stresses on Second-Stage Disk at 6,100 RPM . . . . . | 79 |
| 27 | Temperature Distributions on Outer Face of Second-Stage Disk at Various Times During a Standard Run | 80 |
| 28 | Temperature Gradients after 2.0 Hours at 6 KW . . | 81 |
| 29 | Dimensionless Temperature Distributions for 2.0 Hours at 6 KW . . . . . | 82 |
| 30 | Dimensionless Temperature Distributions for 2.0 Hours at 6 KW Plus 1.0 Hour at 0 KW . . . . . | 83 |
| 31 | Variation of Young's Modulus and Poisson's Ratio With Temperature . . . . . | 84 |
| 32 | Thermal Strains on First-Stage Disk After 2.0 Hours at 6 KW . . . . . | 85 |
| 33 | Thermal Strains on Second-Stage Disk After 2.0 Hours at 6 KW . . . . . | 86 |
| 34 | Thermal Strains on First-Stage Disk After 2.0 Hours at 6 KW Plus 1.0 Hour at 0 KW . . . . . | 87 |
| 35 | Thermal Strains on Second-Stage Disk After 2.0 Hours at 6 KW Plus 1.0 Hour at 0 KW . . . . . | 88 |
| 36 | Dimensionless Thermal Stresses on First-Stage Disk After 2.0 Hours at 6 KW . . . . . | 89 |
| 37 | Dimensionless Thermal Stresses on Second-Stage Disk After 2.0 Hours at 6 KW . . . . . | 90 |
| 38 | Dimensionless Thermal Stresses on First-Stage Disk After 2.0 Hours at 6 KW Plus 1.0 Hour at 0 KW | 91 |

39 Dimensionless Thermal Stresses on Second-Stage Disk After 2.0 Hours at 6 KW Plus 1.0 Hour at 0 KW . . . . . 92

40 Stresses on Second-Stage Disk Due to Combined Thermal and Centrifugal Loands of 2.0 Hours at 6 KW and 3,000 RPM . . . . . 93

A1 Principle of Rotor Balancing System . . . . . 107

A2 Mass Moment of Inertia of Body of Revolution . . . . . 107

A3 Evaluation of Bearing Flexures . . . . . 108

B1 Model of Blade Segment with Balance Weight Attached . . 119

B2 Constant Cross Section Model of Second-Stage Disk . . 120

B3 Equilibrium Conditions at Radius $r_2$ . . . . . 121

B4 Centrifugal and Thermal Stress Distributions in Replacement Model of Second-Stage Rotor . . . . . 122

C1 Comparison of Hub Bolts Before and After Tensile Test . . . . . 127

C2 Load-Elongation Curves from Tensile Tests of Hub Bolts . . . . . 128

C3 Load-Strain Curve from Tensile Test of Hub Bolt Material Specimen . . . . . 129

C4 Load-Strain Curve from Tensile Test of Age-Hardened Hub Bolt Material Specimen . . . . . 130

LIST OF TABLES


| | | |
|---|---|---|
| 1 | Strain Data from Preliminary Spin Tests . . . . . | 94 |
| 2 | Test-Rotor Dimensional Changes After 6,000 RPM Spin Test for Fabrication Evaluation . . . . . | 95 |
| 3 | Summary of Tensile Test Results for Annealed and Heat-Treated Inconel 718 Hub Bolts and Tensile Specimens . . . . . | 96 |
| 4 | Corrected Strain Data from Room-Temperature Spin Tests and Elevated-Temperature Tests . . . . . | 97 |
| 5 | Characteristics of Disk Temperature Profiles for Several Heater Power Inputs . . . . . | 98 |
| B1 | Effect of Balance Weight on Centrifugal Blade-Disk Attachment Stress of Second Stage Disk . . . . . | 123 |
| Ci | Summary of Tensile Tests on Hub Bolts . . . . . | 131 |

# I. SUMMARY

This report presents experimental data of the tangential and radial stresses in the turbine disks of the oxidizer turbopump designed for the M-1 engine. This two-stage Curtis turbine is a special light-weight design. It has thin conical disks to which the blades and shrouds are attached by electron-beam welding. The geometry of the rotor assembly made theoretical stress analysis uncertain. Therefore, it was considered necessary to experimentally determine the disk stress distributions under thermal and rotational loads. The measured distributions could then be used to evaluate and improve computer design programs.

The stresses were obtained by strain-gage measurements using a slip-ring assembly to transmit the electrical signals from the rotating assembly. Measurements were made at different rotative speeds and different thermal loads. Room temperature tests were made to a speed of 6,000 rpm or 150 per cent of the normal operating speed. Most hot tests were carried out at low rotational speeds and maximum hub to rim thermal gradients obtainable without exceeding 625$^{o}$F at the disk rim. Hot tests at the desired rim temperature of 1,000$^{o}$F could not be completed due to the non-availability of suitable strain gages. Hot tests at 625$^{o}$F and 3,000 rpm verified that the principle of superposition for the centrifugal and thermal stresses was valid for the subject rotor.

Detailed inspections and measurements of critical dimensions before and after the test series showed that the turbine rotor maintained its mechanical integrity at all operating conditions. However, a problem was experienced during the tests which involved elongation of the bolts used to secure the turbine disks to the rotor hub. The problem was traced to a misunderstanding between test personnel and the bolt manufacturer, which resulted in the installation of bolts in the low-strength annealed condition and did not indicate a design deficiency.

The report also describes the test facility, design of associated hardware, test procedures, instrumentation, and tests for selection and calibration of strain gages.

## II. INTRODUCTION

The turbine rotor assembly tested in this program was designed by the Aerojet-General Corporation under contract to the National Aeronautics and Space Administration. The light-weight design utilized a new and unfamiliar material (Inconel 718) and a relatively undeveloped electron-beam welding process. The fabrication of the rotor assembly as well as other engine components was completed by the Jet and Ordnance Division of Thompson-Ramo Wooldridge. Details of the design and fabrication are given in Refs. 1 through 3.

The turbine assembly, as shown in Fig. 1, was designed to operate at 4,000 rpm with an inlet total temperature of 1,190$^{o}$R, and produced 36,000 shaft horsepower to drive the oxidizer turbopump shown in Fig. 2. The turbine bearings are lubricated, and the shaft and rotor hub area are cooled by liquid oxygen. The M-1 engine shown in Fig. 3 has two separate turbopump assemblies; one for pumping liquid hydrogen, and the other for pumping liquid oxygen to the respective injector manifolds of the thrust chamber. Each turbopump has its own direct-drive turbine with drive gas supplied by a gas generator. The gas initially drives the liquid hydrogen pump turbine, then it is further expanded to feed the liquid oxygen turbopump turbine.

The weight-saving concepts employed in the design of the turbine rotor assembly resulted in a weight reduction of approximately 50 per cent. This was accomplished primarily by the use of hollow, thin-wall (.063 inch) turbine blades and thin-membrane (.300 inch) turbine disks. The blades were attached to the disks and shrouds by electron-beam welds instead of the more conventional dove-tail or fir-tree methods. Each disk was coned approximately 7.5 degrees and included an integral circular flange or spacer ring near the outer radius of the disk as seen in Fig. 4. Figure 5 shows the conical disks bolted to a common hub. Face contact at the circular flanges during rotation forms a box section structure for protection against shock loading and vibrations.

The geometry of the turbine rotor with its unique bolted-membrane disks did not readily lend itself to theoretical stress analysis. Hence, a program was established to perform spin tests of the turbine rotor, to obtain measurements for the evaluation of the design stress program, and to confirm the fabrication integrity. As originally established, the test program required two specific tests to obtain two sets of strain data for design evaluation; one set of data to be obtained at the mechanical design speed of 4,000 rpm with the disks at ambient temperature, the second test to be made at 4,000 rpm with a disk temperature profile where the maximum hub temperature is 300°F and the rim temperature is approximately 1,000°F. Also required was a spin test for fabrication evaluation to be made at ambient temperatures and at a maximum rotational speed not to exceed 170 ksi stress.

The specific goals of the original test program could not be met because of the nonavailability of a suitable strain gage for static strain measurements in thermal gradients and/or temperatures of 1,000°F. For the reason stated above and due to changes in the M-1 rocket engine program, the spin-test program philosophy was changed from verification of a specific design at its operating conditions to one of fundamental understanding of the stress distributions in a rotor of this configuration. The tests were made using strain gages that limited maximum rotor temperatures to 650°F. The large number of gages involved coupled with the problems and limitations of the slip-ring assembly required many test runs and several hundred hours of test time to establish and verify the stress distributions. The dimensionless stress parameters presented in this report are applicable to any geometrically similar rotor for a wide range of operating conditions.

## III. HARDWARE DESCRIPTION

### A. TEST ROTOR

The test rotor assembly as furnished consisted of the two turbine wheels and a rotor hub. Figure 1 shows the assembled rotor mounted in the measuring and balancing stand. The test rotor assembly was actually built for use in the M-1 engine and is an operational part in every detail. Figure 4 provides an inner view of the disassembled second-stage turbine wheel showing the parallel face lugs at the disk bore, which match with radial slots in the hub to transmit torque and to maintain concentricity as the rotor expands. The same arrangement is used to attach the first-stage turbine. The actual rotor shaft was replaced with a special arbor shaft and adapter described later under modifications. The mean diameter of each stage is 33 inches.

The box-section structure of the rotor assembly is shown in Fig. 5 with the two conical disks clamped to a common rotor hub. The nine hub attaching bolts were not furnished with the other components, but were manufactured locally in accordance with specifications of Drawing 2011 of Appendix D. The bolts were made from 3/4-inch Inconel 718 bar stock. A certified report of the bolt material heat showed that the material possessed a 0.2 per cent yield strength of 165 ksi. A total of 13 bolts was fabricated in accordance with machining procedures described in Ref. 4. When installed in the rotor assembly, the bolts were torqued to 80 inch-pounds with cotter pins to prevent the nuts from loosening during testing. Figure 6 shows a cross section view of the rotor assembly installed in the spin test facility. Total weight of the rotor assembly was approximately 340 pounds.

### B. EXISTING SPIN TEST FACILITY

The basic hot spin test facility (Figs. 6, 7, and 8) utilized in this program was designed and built for the Astro-Aeronautical Propulsion Laboratories of the Naval Postgraduate School by the Baldwin-Lima-Hamilton Corporation and was completed in November 1965. The unit was designed for testing various types of turbine and compressor

rotors at both ambient and elevated temperatures. Test rotors up to 50 inches in diameter and of maximum axial length of 24 inches can be accommodated. Both strain and temperature data can be taken from the rotating test model through slip-ring assemblies. Prior to this program, the facility was used for one other test program, which examined only centrifugal stresses (Ref. 5).

The test rotor is suspended from the lower end of the drive-turbine spindle shaft which extends through the spin-pit cover plate (Fig. 6). The maximum rotor weight and rotational speeds are determined by choice of drive-turbine size and rating. Two drive turbines were available; a four-inch (rotor diameter) Pelton turbine rated for speeds up to 30,000 rpm with a 250 pound maximum rotor weight, and a four-inch Barbour-Stockwell turbine rated to 60,000 rpm and 200 pounds. Each of the drive turbines contains provisions for applying a reversing air supply for braking. Both drive and brake air supplies are controlled from the control console, with rotor acceleration rates determined by rotor mass and spindle-shaft size.

A lube-oil system mounted adjacent to the spin pit circulates oil through the vibration-damper housing for lubricating and cooling the vibration dampers. This unit has both a delivery and suction scavenge pump to control oil level in the damper housing. The lower vibration damper contains a Garlock shaft seal to prevent oil leakage past the spindle shaft into the spin pit.

A catcher assembly (Fig. 6) is provided at the bottom of the pit to minimize damage in case of rupture in the test rotor or shaft separation. The lower end of the test-rotor arbor shaft is extended and coned to match the tapered inner race of a ball bearing mounted horizontally on top of the catcher base. The catcher assembly was positioned to provide 1/8 inch clearance between the rotor arbor taper and the bearing and would, therefore, limit lower arbor shaft eccentricities to 1/8 inch. A second ball bearing unit at the spindle housing limits travel of the upper shaft. In case of spindle-shaft failure, the rotating assembly

could drop slightly into the catcher assembly and run out between the bearing assemblies. A Bentley-Nevada Proximitor pickup is mounted on the catcher stand to detect shaft eccentricities. The Proximitor output can be displayed on an oscilloscope and monitored as a safety precaution.

A Kinney 30 CFM vacuum service unit is used to evacuate the pit, thus minimizing air-friction effects on the rotating assembly. This unit is capable of maintaining tank pressures in the 50-micron range when properly serviced and maintained.

Air for the drive turbine is supplied at approximately 140 psi from a compressor located in the Jet Engine Laboratory. Sufficient air is available at the spin test facility to permit use of a wide variety of rotor combinations. Drive and brake air supplies to the turbine are regulated through diaphragm-actuated valves located adjacent to the spin pit. Separate regulator valves were installed for adjusting turbine balance air and regulating cooling air flow to the slip-ring contacts.

A 30 kVA Ecco High Frequency motor-generator (M-G) set is utilized for induction heating of the test rotors. The system operates at 10,000 Hz and has a multiple capacitor bank to maintain a power factor close to unity. A cooling water supply is used to cool the M-G unit and is available for the rotor heater element and hub radiation cooling plates. A radiamatic pyrometer is normally mounted near the test rotor to sense the rotor temperature and provide a signal for automatic control of the heater to preselected temperatures. However, this feature was not used for the present tests since the lower control range for automatic control was above the maximum test temperatures.

All systems are operated from the two control consoles of Figs. 7 and 8 located adjacent to the spin pit. Rotational speed of the turbine is measured by means of a magnetic pickup mounted on top of the drive turbine at the slip-ring adapter. Output signal from the pickup is fed to a digital counter for direct readout in rpm. Speed is automatically maintained at preselected values by means of a counter limiter which

operates through relays to open or close the diaphragm valves of the turbine air supply.

Instrumentation leads from strain gages and thermocouples mounted on the test rotor pass through the hollow turbine spindle shaft to slip rings mounted on top of the drive turbine (see Figs. 6 and 7). Two slip-ring assemblies were supplied with the test facility. One, a Lebow 16-channel (conductor) unit which can be used at rotor speeds up to 50,000 rpm, has continuous brush contact and is cooled by flow of liquid Freon through the brush assembly. The other is a 36-channel Superior-Carbon unit designed for speeds to 20,000 rpm. It uses intermittent brush contact actuated by a solenoid on top of the unit, and is air cooled. Each of the 36-coin silver rings has four silver-graphite brushes connected in parallel to minimize the effects of contact resistance.

## C. SPECIAL EQUIPMENT AND MODIFICATIONS

Because of the rotor size and test requirements of this program, it was necessary to design and build several additional items of support equipment.

1. Drive Turbine. A new eight-inch Barbour-Stockwell Model 4146 drive turbine was procured, which could accommodate rotors up to 1,500 pounds and 20,000 rpm. The larger rotor weights are possible mainly by the use of balance air pressure applied to the lower face of the drive-turbine rotor, which reduces the axial force on the rotor bearings. The balance air pressure was also used for positive pressure scavenging of the damper housing. As a safety precaution at low balance air pressures, an additional oil return line with one-way check valve was installed to guarantee adequate scavenging under all conditions. The new drive turbine was purchased in its standard configuration, without a hollow spindle shaft necessary to accommodate instrumentation leads and without provisions to support and drive the slip-ring assembly.

A hollow spindle (Fig. 6) was designed and manufactured for the new turbine. Design calculations are given in Appendix A.1 with the

final design shown in Drawing 2015, Appendix D. The design provides a center bore of 0.407 inch for instrumentation leads and a cross sectional area of 0.125 square inch for load requirements. The spindle extends from the top surface of the drive turbine to approximately one inch below the inner surface of the tank cover. Vibration dampers submerged in oil keep the critical speed of the spindle shaft within safe limits.

In order to accommodate the 36-channel slip-ring assembly, the standard cover plate of the drive turbine was replaced by a mounting support and drive coupling (Fig. 6). The support includes provisions for mounting the magnetic pickup for rotational speed measurement and a thermocouple for the slip-ring reference-junction temperature. The drive coupling contains the electrical connector for instrumentation lead wires and space for stowing unused lead wires from the rotor wheel. Labyrinth seals are used to prevent oil leakage from around the slip-ring drive shaft.

2. Rotor Suspension System. The test rotor is suspended vertically from the lower end of the spindle with its center of gravity approximately 15 inches below the tank cover plate. The suspension system consists of an arbor shaft with hub adapters, arbor to spindle connector with a self-aligning ball bearing, and instrumentation wiring covers (see Figs. 9 and 10). The arbor to rotor attachment is accomplished at the four-inch hub bore using adapters designed to hold concentricity and squareness to close tolerances. The arbor also provides surfaces for self-aligning ball bearings to be used with the measuring and balancing rig described below. Torque is transmitted between arbor and rotor by shoes attached to the adapters that engage cutouts in the rotor hub. Appendix A.1 and Drawings 2007-1, -2A and 2018 of Appendix D provide pertinent suspension-system design details.

The arbor is suspended from a self-aligning ball bearing located at the arbor to spindle connector, which permits the turbine wheel to rotate about its center of gravity. Aluminum covers are provided to store and protect instrumentation lead wires during rotation. The entire rotor assembly can be prepared for installation in the spin pit and then set on the

spin-pit flange using the rotor handling rig described below. The spin-pit cover plate rests on safety supports while final mechanical and electrical connections are made. Figure 9 shows the rotor mounted above the spin pit ready for final hookup.

3. Measuring and Balancing Rig. The test specifications required that the turbine assembly be balanced prior to testing and that specified dimensions of the turbine disks be measured prior to and after the fabrication evaluation test. A single rig was designed and manufactured to serve both requirements. Figure 1 is a photograph of the measuring and balancing rig with the test rotor installed.

The rig was built using support flexures with adapters for self-aligning ball bearings mounted approximately eight inches apart on each end of the rotor arbor shaft. The rotor was mounted horizontally in the stand, as shown in Fig. 1, and supported on the ball bearings at the upper end of the vertical support flexures. The rotor was driven by a jet of air directed onto the turbine blading. Provisions are made for centering and clamping both bearings for rotor assembly measurements or securing one bearing at a time for dynamic balancing. Design details are given in Appendix A.2 and Drawing 2022, Appendix D.

Measuring stations were provided at various locations on the outer faces of each disk, along the blades and shroud, and at the circular flanges (Drawing 2022, Appendix D). Measurements were made using a special spring-loaded probe, inserted through a bushing provided in the support frame. An inside micrometer was used to measure the distance between the probe head and the bushing to establish the rotor measurements relative to the fixed support frame.

Provisions were made to clamp either of the two rotor bearings for dynamic balancing. The horizontal shaft deflections produced by unbalanced forces on the rotor were detected by a proximeter pickup with the output displayed on an oscilloscope. A flux cutter and magnetic pickup were used to detect angular position, which was also indicated on the oscilloscope. A jet of compressed air directed onto

the turbine blades was used to accelerate the turbine to slightly above its critical speed. Pictures were taken of the oscilloscope grid as the rotor decelerated through the critical speed and were analyzed to determine the magnitude and relative angular position of the imbalance.

An alternate method was developed during the balancing process which eliminated the need for the oscilloscope and camera. A common lead pencil was mounted on the measuring stand and adjusted to produce a trace on a paper disk attached to the end of the arbor shaft (Fig. 1). The rotor was accelerated to slightly above the critical speed and the drive air turned off. The pencil was then adjusted to produce a trace on the paper disk as the rotor decelerated through the critical speed. The horizontal oscillations of the arbor caused by rotor imbalance produced a trace which was offset from its center and could be used to locate the angular position of the unbalance.

4. Rotor Handling Rig. It was necessary to design and build a rotor handling rig (Fig. 9) to permit ease of handling and to eliminate the possibility of damage to the rotor. The rig consisted of a triangular aluminum frame with hardwood blocks that clamp and hold the rotor at the drum spacer between the blades. Design details are given in Appendix A.3 and Drawing 2021-2, Appendix D. The rotor assembly could be supported by the rig with its axis either horizontal or vertical and could be lifted by hoist. Adjustable legs were provided at each corner of the rig so that it could be set on the spin-pit flange and leveled to facilitate connecting of the rotor arbor to the spindle shaft.

5. Heating and Cooling Coils. The purpose of the heating and cooling coils was to produce thermal gradients in the rotor disks corresponding to those which would exist in the wheel during engine operation. Induction heating coils were constructed using 3/8-inch copper tubing to provide for a cooling water flow against resistive heating in the coils during operation. Location of the coils relative to the rotor is shown in Fig. 10. Design calculations proved to be of limited value, and the final design evolved from a cut and try procedure. Two flat coils of

five turns each, wound in "pancake" fashion, were attached to sheets of Johns-Manville Marinite insulation. The coils were wound in opposite directions and connected in parallel. The coils had a width of 2 1/4 inches and an outside diameter of approximately 28 inches to place the maximum induction field at the rotor disk rim. The insulation sheets, Figs. 10 and 11, provided support for the heating coils and enclosed the rotor to prevent radiation heating from the rotor to the spin pit cover plate and had provisions for adjusting the clearance between the coils and rotor.

Cooling coils were used for hub cooling to produce thermal gradients in the rotor disk. Copper plates, 1/8 inch thick, were fitted around both outer faces of the rotor hub to cool the inner parts of the rotor disks and around the arbor shaft to cool instrumentation lead wires, as shown in Fig. 10. Cooling water was circulated through copper tubing brazed along the back side of the cooling plates away from the rotor, and thermocouples were installed in the water inlet and discharge lines. The upper cooling coils and plate were split to permit removal of one-half of the assembly providing access to the hub terminal connector for wiring changes (Figs. 11 and 12).

6. Calibration Beam. A calibration beam device (Fig. 13) was constructed to evaluate strain-gage performance at room and elevated temperatures. The beams and holding jig were made from Inconel 718 with the load screw and mounting bolts of stainless steel. Two beams, a straight cantilever beam and a uniform-stress beam, were made 0.3 inch thick (same thickness as the rotor disks), and the entire assembly could be placed in a furnace. The uniform-stress beam was used exclusively since it provided a large constant-strain surface for simultaneous comparison of several gages. The device was calibrated using conventional strain gages and a Tuckerman optical gage.

## IV. PRELIMINARY AND FABRICATION-EVALUATION SPIN TESTS

Several delays were encountered in the selection of a suitable strain gage for static measurements at elevated temperatures. While several strain-gage configurations were available for high-temperature testing and dynamic strain measurements, many demonstrated excessive temperature effects and proved unsuitable for actual steady-state strain measurements on a rotating disk. Others required difficult mounting procedures and high temperature cures, which were nearly impossible to perform with the large size rotor. Further delays involved the existing strain-gage instrumentation and recording system of the spin test console which proved unsatisfactory, and a new data acquisition system ordered as a replacement was damaged in shipment. Due to these delays, it was decided to proceed with the ambient-temperature spin tests using available low-temperature gages and manual data scanning and recording procedures. The search for a suitable gage was continued during the preliminary spin tests.

### A. INSTRUMENTATION

The gages used in the preliminary test series were 350-ohm foil gages manufactured by the Budd Company with a gage factor (GF) of 2.07. The sensing element was 1/4 x 1/4-inch on a 1/2 x 3/4-inch phenolic backing. Gages were bonded to the wheel using Eastman 910 cement and standard bonding procedures. Installations were checked for minimum 50 megohms resistance to ground.

A total of 36 gages was installed on the two rotor disks with gages placed at four different radii on each of the four wheel faces as shown on Drawing 2007-2, Appendix D. Gages were mounted in pairs with one aligned radially and the other tangentially, as seen in Fig. 1. The gage lead wires were attached to solder terminals bonded to the rotor with Eastman 910 cement. Stress-relief terminal loops were used between the strain-gage and lead-wire terminals. The lead wires were held in place along the rotor disk contour by Nichrome ribbon straps spot welded

to the disk with a capacitance discharge welder. General Electric Silicon Rubber adhesive/sealant (RTV) was used in repairing lead-wire insulation damage and for additional securing of lead wires.

Seventy-two varnish-insulated copper lead wires from the installed gages were routed inward to the rotor hub connector pins, upward along the rotor shaft to the spindle flange, then through the hollow spindle shaft to the slip rings, as indicated by the arrangement on the left of the shaft in Fig. 6. Terminal connector pins at the rotor hub, arbor to spindle mating flange, and slip-ring attachment were provided to permit disconnecting or disassembly of the rotor without having to cut and splice the wires. Since only 36 lead wires could be connected to the slip rings at one time, the remaining wires were stored in the slip-ring connector housing. Wiring change-overs between runs were made at the slip-ring connector.

The electrical circuit consisted of a basic two lead-wire system, with the gage and leads forming one leg of a Wheatstone bridge. Eighteen gages at a time were connected to a B-L-H 20-channel manual switching and balancing unit using a common bridge completion network and excitation power supply. Bridge excitation was maintained at six volts DC and power was applied to individual gages as selected when the slip rings were closed. Individual ten-turn potentiometers were used to balance each gage to the bridge network for a zero bridge output. Bridge output was amplified and fed through a voltage to frequency converter and to a digital counter for manual recording. A calibration resistor shunted across the gage leads simulated a calculated strain value and was used to adjust the signal amplifier gain to give a direct readout in microinches/inch strain.

## B. PRELIMINARY SPIN TESTS

1. Preparations and Test Procedures. The instrumented assembly was placed in the Measuring and Balancing Rig where it was balanced, and specified dimensional data were recorded for future comparisons. The rotor critical speed was determined to be approximately 124 rpm. Balancing was accomplished by adding lead weights as needed along the inside of the shroud. A typical installation of such weights is noticeable in Fig. 1. The maximum

weight added at any location was of the order of eight grams per blade segment. The weights were strapped in place using Nichrome ribbon spot welded to the shroud.

The test rotor was then installed in the spin pit and prepared for spin testing. Due to the frequent opening, tank pressures of 1/10 inch mercury absolute or better were considered acceptable for testing. The drive-turbine balance air was maintained at 30 psi gage pressure which offset approximately 90 per cent of the rotor assembly weight.

Prior to the start of each test run, the slip rings were closed and each gage channel was selected and adjusted for zero bridge output. The calibration resistor was then shunted across a single gage and the signal amplifier gain was adjusted to the calculated strain value. The power supply for the proximeter pickup was turned on and the oscilloscope trace adjusted for static conditions.

The drive-turbine air was adjusted to maintain an acceleration rate of approximately 300 rpm per minute. The maximum rotor oscillations seen by the proximeter pickup occurred between 100 and 150 rpm, which corresponded to the previously observed critical speed of the assembly. The oscillations decreased rapidly and were not detectable above 1,000 rpm. The automatic speed control maintained rotor speed to within $\pm$ 10 rpm of the selected speed.

With rotor speed stabilized at the desired rpm, power was applied to the slip-ring solenoid bringing the brushes in contact with the rings. The manual selector switch on the switching and balancing unit was set to the first channel, which applied excitation power to that gage. Approximately eight to ten seconds were allowed for the strain reading to stabilize before the strain reading was recorded. The next channel was then selected and the same procedure repeated until all 18 channels were recorded. This procedure was repeated for rotor speeds of 1,000; 2,000; 2,800; 3,400; and 4,000 rpm. Braking air was applied to the air turbine to reduce the speed. Strain data were again recorded at the same speeds on the decreasing speed cycle. The rotor

was stopped by applying braking air to the drive turbine. A post-run inspection of overall conditions was made following each run, and desired gage wiring changeovers were made for the next run.

As an indicator of data accuracy, the strain data from each gage was plotted against $(rpm)^2$. The data generally gave a straight-line relationship, but frequently the line would not pass through zero. Sometimes the data from the same gage on different runs gave a straight line with equal slope, but shifted by as much as 200 microstrain from previous data. It is believed that this shift was due to a change in contact resistance, either in the terminal connections or slip rings, caused by movement of the lead wires after zeroing the bridge output at static conditions. Since it is known that the strain is zero at zero rpm and that it must vary directly with $(rpm)^2$, it is felt that by adjusting the plots to pass through zero one obtains the representative values of strains actually experienced by the gage.

Problems were encountered during this series of room-temperature spin tests, necessitating a total of 16 runs to establish the strains in the rotor disks. The problems mainly involved the lead wires, terminal connector pins, and slip rings. The radial loading on the connector pins due to centrifugal forces acting on the lead wires caused the pins to become loose, which resulted in data scatter or caused the gage to become inoperable. Most of the connector pins were eventually soldered in place. Breakdown of lead-wire insulation, usually at tie-down straps or at sharp corners, caused some of the gages to ground out. Repairs were made with RTV cement. Broken lead wires in the slip-ring assembly usually occurred between the brush-block units and caused excessive signal noise and data scatter. Although not specifically detected on these runs, later tests showed some evidence of brush contact heating at higher speeds.

Only minor problems were encountered in the mechanical systems. The vacuum pump had to be disassembled to remove deposits

built up as a result of excessive moisture trapped in the oil. Also, on the first run to 4,000 rpm, the large-diameter snap ring used to secure the arbor cover (RS 600, Drawing 2007-2A, Appendix D) became loose due to centrifugal forces. All snap rings used on the rotating system were then either replaced by machine screws secured by safety wires, or were fitted with safety covers to prevent their loosening under load.

2. Test Results. The strain data obtained during these tests were previously submitted to NASA and are listed in Table 1. A discussion of these data is not given here since its accuracy was not verified and the tests were, in effect, repeated in later runs using improved gaging and instrumentation, as reported in Section VI below.

3. Spin Test for Fabrication Evaluation

a. Test Preparation and Procedure. As stated earlier, one objective of the test program was the evaluation of the rotor at conditions near the elastic limit of the rotor material in order to determine rotor fabrication integrity. Data from the preliminary tests were reviewed jointly by representatives from NPS and NASA. The data from runs made to 4,000 rpm were projected to rotational speeds up to 6,000 rpm. It was jointly agreed that available data indicated a fabrication-evaluation run could be made up to 6,000 rpm without exceeding the 170 ksi stress limits stipulated in the contract.

Attempts to provide high-speed photographic coverage for this test were unsuccessful. Due to the very limited area of the viewing window in the pit cover, mounting of both lights and camera inside the pit would have been required, along with an external control system. For these reasons and the probable effect of radiation heating from high intensity lights, it was decided to conduct the test without photographic coverage.

The 18 most reliable gages were connected through the slip rings to the readout. After insuring that all systems were functioning properly, the speed was brought up slowly to 4,000 rpm. Strains were

recorded at intermediate points and compared with data from earlier tests. Speed was then increased gradually to 6,000 rpm in 500 rpm increments. The speed was actually as high as 6,100 rpm for a few seconds then adjusted and stabilized at 6,000 rpm for data recording. Strain data were recorded at each of the speed set points and compared with the projected data before making the next speed change. Three of the gages failed at 4,500 rpm, seven were inoperative at 5,000 rpm, and only 3 gages were still working at 6,000 rpm.

Except for the gages that failed, no difficulties were apparent during extensive operation at 6,000 rpm and throughout the run. There was no evidence of unusual vibrations or noise. The Proximitor display was normal; and there was no evidence of oil leakage from the spindle shaft seal, which would be expected in case of excessive spindle-shaft vibrations. Braking air was applied to the air turbine, and the rotor was brought to a complete stop. The tank vacuum pressure was bled off, and the tank cover with suspended rotor was raised for a detailed post-run inspection.

b. Test Results. Inspection revealed a gap of about 0.2 inch at the spacer drum between the rotor blades. Both disks were loose at the hub attachment bolts. The cotter pins used as a safety on the nuts and bolts were in place. Strain-gage lead wires were torn loose at both the terminal pins and on the disk surfaces. The gages themselves were intact except where torn loose by the lead wires. The rotor assembly was removed from the spin pit and disassembled for further examination. There was no indication of contact between the rotor and any other part.

The hub attaching bolts were removed and examined individually. Each of the nine bolts was elongated by approximately 0.185 inch, and the bolt central shaft diameter was reduced by approximately 0.016 inch. Details of the bolt failure are discussed in paragraph C below.

The wheels were reassembled using substitute bolts and mounted in the Measuring and Balancing Rig to check for possible deformations. Measurements were made at nine measuring stations on each disk

and repeated for four peripheral stations around the wheel. A comparison of these data with the measurements made prior to the spin tests is given in Table 2. The differences of Table 2 are considered to be within reasonable measuring tolerances and do not indicate actual deformations in the wheel.

The electron-beam weld joints which secure the rotor blades to the disk rim were not affected by the 6,000 rpm spin test. This fact is especially significant since the electron-beam welding technique represents advanced technology developed specifically for the test rotor as discussed in Ref. 3. Centrifugal stresses at the second-stage blade-disk attachment are estimated in Appendix B.1 to be 40.9 ksi at 6,100 rpm. This stress is shown to be about 3.5 per cent higher than that which would normally exist at the joint without the added centrifugal stresses caused by the balance weights attached to the shrouds. Thus the blade-disk attachment withstood, without failure, a slightly higher centrifugal load than that which would normally occur at 6,000 rpm.

## C. DISCUSSION OF HUB-BOLT BEHAVIOR

To explain the severe and unexpected 0.185 inch elongation of hub bolts at 6,000 rpm, a bolt tensile test program was initiated to establish the loads which caused bolt elongation and to evaluate the tensile strength of the Inconel 718 bolt material. Details of this test program are given in Appendix C. Significant results were as follows:

It was established that the maximum hub-bolt load during spin tests to 6,100 rpm was approximately 6,600 pounds. This load corresponds to an engineering stress of only 86.0 ksi, the maximum condition at which the 0.185 inch plastic deformation occurred. However, as stated in Section III.A above, tensile tests conducted by the bolt material supplier established a 0.2 per cent yield strength of 165.0 ksi. This apparent discrepancy indicated that the actual bolts were constructed of a material having a 0.2 per cent yield strength much less than that of the high-strength Inconel 718 as certified by the supplier.

However, this indication was not evident initially, and a new set of bolts of identical material but modified design was ordered to allow continuation of rotor testing. The primary modification for these new bolts was a nominal diameter increase from 0.313 inch to 0.323 inch. Moreover, the threads were ground instead of turned. Drawing 2011-A, Appendix D gives details of the modified bolt geometry. These bolts also stretched during rotor tests under combined thermal and centrifugal loads as will be discussed in Section VII.A below. Furthermore, a tensile test specimen (Drawing 2011-A, Appendix D) ordered from the same stock as the modified bolts exhibited a 0.2 per cent yield strength of only 68.6 ksi when tested, again indicating that the bolt tensile strength was much less than that commonly reported for Inconel 718.

Eventually, near the end of the program, this problem was cleared up. The bar stock, from which both sets of bolts were machined, was supplied in an annealed condition since machining is much easier when Inconel 718 is in this relatively ductile state. However, after machining the bolts required an age-hardening heat treatment in order to precipitate out the intermetallic and carbon strengthening phases (Ref. 7). The tensile specimen made from the bolt material had been given the proper heat treatment as indicated by tensile properties shown in the certified report, but for some reason the bolts were not treated. Test personnel erroneously assumed that the bolts had been given the same heat treatment as the certified tensile test specimen since all were made from the same piece of material. Therefore, all hub bolts tested in the rotor and in the tensile test program of Appendix C were actually in an annealed, low-strength condition. This accounts for the plastic elongation which occurred at relatively low bolt loads during spin tests and for the poor tensile properties obtained in tensile tests.

To verify the above explanation, a remaining tensile specimen was given an age-hardening heat treatment and tested at NPS. A 0.2 per cent yield strength of 142.8 ksi was obtained, verifying that heat treatment would have strengthened the hub bolts sufficiently to prevent elongation

during rotor tests. Tensile properties of all specimens tested are summarized in Table 3.

## V. HIGH-TEMPERATURE INSTRUMENTATION

One important objective of the program was to establish whether the disks could support the thermal stresses which are caused by radial temperature gradients. For these tests the ambient-temperature gages described above had to be replaced by high-temperature gages. This section describes the effort involved in selection, evaluation, and mounting of the high-temperature instrumentation system. The instrumentation described below was used for a second set of ambient-temperature spin tests to provide a check of the preliminary spin tests as well as for high-temperature runs.

### A. STRAIN-GAGE SELECTION

1. Gage availability. Finding an acceptable gage for strain measurement at elevated temperatures was more difficult than originally anticipated, although a number of suppliers fabricate gages for high-temperature work. Test personnel visited and discussed the specific gage requirements of this program with various strain-gage manufacturers, other agencies doing high-temperature testing, and recognized specialists in the field. General impressions gained from these contacts were as follows:

a. Only a few activities are performing static (steady-state) strain measurements on rotating components at elevated temperatures.

b. Few, if any, are measuring static strains in steep thermal gradients. The upper temperature limit for most gages used for static strain measurements is generally around 650$^{o}$F.

c. High-temperature gages are usually attached to the surface by spot welding, flame spray (Rokide), or ceramic cements. Welding and flame-spray processes require expensive equipment but are easier to apply than

cements on large components. Cements require high temperature cures while applying pressure on the gage.

d. Dual-element gages, using a thermocouple or similar device to adjust gage performance, require complex bridge circuitry and are expensive. Even then the gage may be compensated only at one fixed-temperature point, which must be known in advance.

e. The best approach to temperature compensation is probably the half-bridge configuration where the active (measuring) gage and dummy (zero-strain) gage are subjected to the same temperature. While satisfactory for simple tests, this approach is usually not practical on a spinning disk or in thermal stress fields where it is impossible to subject the dummy gage to identical temperatures without placing it on the stressed disk.

f. High-temperature gages are available in a broad price range of fifty to ninety dollars for most dual-element gages. Some single-element gages with self-temperature compensation (heat treatment to adjust the thermal coefficients of expansion and resistivity to specified values) are available at a cost of about seven dollars.

g. Some gages have a limited useful life at temperature (as low as five hours) due to permanent metallurgical changes in the sensing elements.

2. Tests for Gage Selection. Based on the above review, a test plan was initiated to select and test a number of gage types that appeared to offer the best possibilities. From this test, one gage type would be selected for a detailed evaluation prior to use on the test rotor. The following four types of gages were tested:

B-L-H HT 1235-4B. This is a 1/4-inch, single-element, free-filament, platinum wire grid with a chromel-alumel thermocouple junction. The gages are nonself-temperature compensated and are advertised for static strain measurement to 1,200°F.

B-L-H FNH-50-12E. This is a universally temperature-compensated, foil gage applied with ceramic cement. The 1/2-inch sensing element is made of Nichrome foil and includes a platinum-wire compensating element for temperature to 850°F. The cement precoat and overcoat require temperature cure cycles.

Microdot SG-420. This is a half-bridge, weldable gage, which has a one-mil, platinum-alloy strain filament and a strain-free, temperature-compensating filament combined in a single strain tube. By using the proper external temperature-compensating resistor in the bridge completion network, apparent strain errors with temperature should not exceed ± 150 microinches/inch. Highly compacted magnesium-oxide powder is used in the strain tube for electrical insulation and to transmit strains to the filament. The Inconel strain tube is line welded to an Inconel flange for mounting. The overall length is 1.094 inches, and the gage is advertised for static strain measurement to 950°F.

Microdot SG-180. This gage is similar to the SG-420 above, except that it has a single Nichrome filament usable to 650°F for static measurements. Strain tube and mounting flange are stainless steel with overall length of 1.16 inches.

Two gages of each type were mounted on the uniform-stress calibration beam of Fig. 12 for initial evaluation. Installation and wiring were in accordance with manufacturers' instructions. The gages were first tested at room temperature to verify the gage factor and to check gage stability. All gages were found to operate satisfactorily. The calibration-beam assembly with gages was then placed in a furnace and the temperature was increased slowly to 650°F. The temperature and gage strain readings due to temperature effects were recorded for several different temperatures during the heat-rise cycle. The tests were repeated several times to evaluate gage repeatability and stability at steady-state temperatures.

Based on the results of these tests the Microdot SG-180 gage was chosen, mainly for its repeatable apparent strain with temperature,

ease of application, simple bridge circuit, and lowest unit cost. A possible disadvantage of the Microdot SG-180 gage was the long overall length of about 1.16 inches. The HT 1235 gage showed excessive apparent strains at 600°F, and the FNH 50-12E gage was rejected because of its difficult application process and the requirement of a high temperature cure. The SG-420 gage requires the addition of a temperature-compensating resistor adjusted for each gage installation. This system would have resulted in severe complexities in wiring and difficulties for data acquisition, making the gage unsuitable for the present purpose in spite of improved temperature capability. Also, the cost factor of ten over the SG-180 gage was considered unreasonable for the present purpose in spite of improved temperature capability.

## B. DETAILED EVALUATION OF SELECTED STRAIN GAGE

Ambient and elevated temperature tests were conducted on the Microdot SG-180 gages to establish gage performance parameters for correction of rotor test data. Eight gages were randomly selected for evaluation out of a total of 51 gages procured from the same manufacturer's lot number. All gages were self-temperature compensated to nine parts per million per °F over the range of 75 to 650°F. This established the maximum rotor temperature to be used for the high temperature tests. The SG-180 is a nominal 120-ohm gage with a gage factor of 1.80. Figure 14 shows gage configuration and construction details.

The gages were spot welded to the uniform-stress calibration beam with 32 welds per inch. Four of the gages were mounted for tension loading and the other four in compression. Nichrome-alloy lead wires were silver brazed to the gage leads to form a three-lead-wire system. This was done to prevent signal shifts due to resistance changes in the leads caused by temperature variations. Iron-constantan thermocouple measuring junctions were spot welded to the beam alongside and at the equivalent center of each gage. The entire electrical hookup duplicated that which was to be used in

the turbine rotor tests. Figure 15 is a schematic wiring diagram of the three-wire arrangement and the data-system input conditioning.

1. Signal Conditioning. The strain-gage manufacturer recommends a correction for signal desensitization due to effects of long-lead-wire resistance on bridge sensitivity. The measured resistance of a single conductor from gage to data system was 1.42 ohms, and the measured gage resistances of the eight selected gages varied from 119.12 to 120.71 ohms. The bridge completion resistors on the signal-input conditioning cards were precision-quality resistors of 120 ohm. The "natural" gage factor of 1.8, as specified by the manufacturer, was modified by a simplified resistance ratio to obtain a "desensitized" gage factor $GF_d$, or

$$GF_d + \frac{R}{R_g + r} (GF_n)$$

where: $GF_n$ = specified "natural" gage factor - 1.80

$R = R_1 = R_2 = R_3$ = bridge-completion resistor, ohms

$R_g$ = measured gage resistance, ohms

r = measured lead resistance -- single conductor-gage readout, ohms

Hence, for $R_g = 119.12$ and $r = 1.42$,

$$GF_d = \frac{120}{119.12 + 1.42} \times 1.80 = 1.7919$$

The desensitized gage factor was then used in calculating a calibration set point for adjusting the data system to automatically correct for the lead-wire effect. A fixed calibration resistor mounted on the signal-input conditioning card could be internally shunted across two leads from the strain gage to simulate a strain at the gage. A resultant strain was calculated and then used as a calibration set point for adjusting the data system to read out directly in micro engineering units.

That is:

$$\epsilon_c = \frac{1}{GF_d} \times \frac{R}{R_g + 2r + R_c}$$

where,

$\epsilon_c$ = Calculated strain, microinches/inch

$GF_d$ = Desensitized gage factor

$R = R_1 = R_2 = R_3$ = Completion resistor, ohms

$R_g$ = Gage resistance, ohms

$r$ = Lead resistance -- single conductor, ohms

$R_c$ = Calibration resistor, ohms

For the above example, and $R_c$ = 50,000 ohms

$$\epsilon_c = \frac{1}{1.7919} \quad \frac{120}{119.12 + (2 \times 1.42) + 50{,}000}$$

$$= 0.001336 = 1336 \ \frac{\text{microinches}}{\text{inch}}$$

The above calculations were carried out for the measured resistances of each gage mounted on the beam, and the calibration set point was recorded for each gage circuit for future use.

2. Gage Performance Evaluation at Ambient Temperature. Tests were made with the gages at room temperature to verify gage performance, evaluate gage mounting procedures, and to study the effect of long lead wires. Each gage channel was balanced to zero, and the gage excitation or span was set for the calibration set point calculated above. The excitation voltage was approximately 2.2 volts which helped to minimize errors due to gage self-heating. The beam was loaded with the load screw to produce a measured deflection of 0.614 inch which corresponds to a strain of 2,000 microinches/inch. The load was removed and the gages checked for zero shift. The zero setting was readjusted, and the procedure was repeated several times to determine the effect of load cycling. The beam was then deflected by approximately 0.1-inch increments and the strains recorded to verify the linearity of the gage reading with deflection. To evaluate gage stability, the beam was loaded for 2,000 microinches/inch and held for one hour. Strain readings were recorded at the beginning and end of the period.

The results of the tests at room temperature were satisfactory. They showed that the gages were reliable and that the correct mounting procedures had been adopted. The zero shift after the first load cycle varied from ten to 17 microinches/inch. This shift was reduced to less than five microinches/inch on subsequent cycles. The strain readings with increasing loads were linear within approximately six to eight microinches/inch. Gage creep, the change of gage strain reading with time at constant load, was negligible. The following data were recorded for the different gages at a beam deflection corresponding to an actual strain of 2,000 microinches/inch:

Gage#1: +1,947 microinches/inch  Gage#5: -2,001 microinches/inch
Gage#2: +2,000 microinches/inch  Gage#6: -2,013 microinches/inch
Gage#3: +2,055 microinches/inch  Gage#7: -2,008 microinches/inch
Gage#4: +2,007 microinches/inch  Gage#8: -2,010 microinches/inch

The largest differences between actual and recorded strains occurred for gages #1 and #3. However, these gages had been removed from the load beam after initial installation and then reapplied. It is very likely that this procedure impaired the reliability of these gages. The results obtained with the other gages shows that the above-listed correction for the lead-wire effect establishes correct readings with an error of less than 0.7 per cent.

Errors could have been introduced also because the sensing element of the Microdot SG-180 gages is about 0.014 inch above the beam surface, or if the structure of the gage reinforces the beam surface. Thus, for a beam in bending, the sensing element experiences higher strains than those existing in the outer fiber of the beam. Conversely, any reinforcing by the gage would tend to reduce the strains. Test data indicate, however, that these influences are either insignificant for the 0.3 inch thick beam, or that they cancel each other.

3. Gage Performance Evaluation at Elevated Temperature. Elevated-temperature tests were made to 600$^{o}$F to establish the apparent

strain of the gages at different temperatures, to evaluate gage stability and gage-factor variation with temperature, and to determine the effect of temperature cycling on gage performance. The term "apparent strain" as used in this report includes those induced strains resulting from a differential thermal coefficient of expansion between elements of the strain gage and the test structure. It also includes the indicated strains resulting from changes in electrical resistance of the gage and lead wires due to variation of the thermal coefficient of resistivity with temperature. The apparent strain would be zero if the entire gage and test specimen had identical thermal coefficients of expansion, and if the gage and attached lead wires had a constant thermal coefficient of resistivity.

a. Evaluation of Apparent Strain. These tests were made by placing the calibration beam in an electric furnace and gradually increasing the temperature to 600°F, followed by cooling in the furnace to room temperature. The complete cycle of heat-up and cool-down to room-temperature conditions required approximately seven hours. Strain and temperature data were recorded at frequent intervals throughout the cycle. The temperature was measured at each gage location. Slight variations in temperature could be noted between the different gages. On the heat-up cycle, the mounted end of the tapered beam was 6-8°F cooler than the free end, indicating that the beam had not reached full temperatue equilibrium. Possible effects of this slight variation in temperature were ignored, and the apparent strains of the individual gages were plotted against the measured temperatures at the same location. The test was repeated several times to evaluate the effect of temperature cycling on gage performance.

After the first temperature cycle to 600°F there were zero shifts of as much as 100 microinches/inch. This shift decreased to less than 30 microinches/inch after subsequent cycles. This experience shows the definite requirement for temperature cycling to stabilize and to insure accurate strain measurement. After the gages had been temperature cycled and stabilized, the apparent strains were repeatable to within

two to three per cent. The following average apparent strains were obtained for the different gages at 600°F:

| | |
|---|---|
| Gage #1: + 802 microinches/inch | Gage #5: + 759 microinches/inch |
| Gage #2: + 766 microinches/inch | Gage #6: + 784 microinches/inch |
| Gage #3: + 834 microinches/inch | Gage #7: + 778 microinches/inch |
| Gage #4: + 757 microinches/inch | Gage #8: + 766 microinches/inch |

Based on these data, the single curve of the apparent strain vs. temperature of Fig. 16 was established for the correction of the test data obtained with the turbine rotor.

b. Evaluation of Gage Stability. Attempts to evaluate gage creep at a constant temperature were unsuccessful due to difficulties with the furnace controller, which made it impossible to maintain an exactly constant temperature. As shown by Fig. 16, slight temperature variations can produce large changes in the apparent strains; hence, gage creep due to temperature effects could not be identified independently of these temperature and apparent strain variations. Therefore, the zero readings of the gages at ambient temperature were recorded before and at the end of a temperature cycle with a one-hour hold at near 600°F. The changes in zero readings represent the combined effects of gage zero shift and creep. The combined creep and zero shift for one temperature cycle and a one-hour hold at 600°F was generally less than 14 microinches/inch. The gages showed good stability over the entire temperature range.

During a particular temperature cycle, one of the gages showed an apparent strain of about twice the normal value found during previous runs, and the zero setting after cool-down was several hundred counts higher than that recorded earlier. Investigations revealed that the gage was partially grounded through a break in the lead-wire insulation. The insulation was repaired and subsequent tests were normal. This experience showed that it is extremely important to maintain adequate gage-to-ground resistance.

c. Variation of Gage Factor with Temperature. Two tests were made to evaluate the effect of temperature on gage factor. For the first

test, the beam was deflected to produce 2,000 microinches/inch strain; then it was placed in the furnace and temperature cycled as during the tests for the apparent strains. Strain data from this run were corrected for temperature by using the apparent strain values established earlier. The resulting data varied only slightly from the 2,000 microinches/inch preload setting, with five gages approximately two per cent lower, two gages less than one per cent higher, and one gage showing no change.

For the second test the procedure was changed to allow for loading of the beam while at temperature, thereby eliminating the need for the apparent strain correction. A spacer block was obtained which could be inserted between the calibration beam and the load-screw bracket of the holding jig, producing a repeatable strain reading of 1,775 microinches/inch at room temperature. The beam, without the spacer block, was placed in the oven; and the temperature was increased to a particular value. The strain readings were recorded after the temperature was stabilized. The spacer block was then inserted, and a second set of strain data was recorded. The difference in the two readings was due only to the strain induced by the beam deflection produced by the spacer block and was independent of apparent strains. Such tests were carried out at 150, 200, 300, 350, 450, and 600$^{o}$F. The data showed that no change in gage factor occurred for temperatures up to about 350$^{o}$F, and that at 600$^{o}$F the gage factor was decreased by about four per cent.

4. Summary. The various tests for gage performance evaluation indicate that reasonably accurate test results can be obtained with gages from the same manufacturing lot number with the following procedure:

a. Mount gages according to manufacturer's instruction.

b. Use standard three-wire hookup for single active gage. Lead wires connected to gage must be of same material as gage element. This is necessary for all connections in the thermal environment to avoid thermocouple effects.

c. Calculate desensitized gage factor for each gage to take account of resistance of lead wires.

d. Calculate strain for each gage calibration set point to obtain readout in microinches/inch.

e. Temperature cycle gages after installation to stabilize for maximum temperature expected.

f. Establish apparent strain curve for each installed gage by testing representative gages from the same lot.

g. Correct data for gage-factor decay with temperature.

C. DATA LOGGING SYSTEM

A new B & F Model SY 133 solid-state data acquisition system was obtained during this period of the program which was used for the strain-gage evaluations and all subsequent rotor tests. The system is capable of acquiring, displaying, and recording data from pressure-scanning valves, force transducers, strain-gage bridges, thermocouples, and frequency sources. Adjustments can be made for calibration and direct readout in engineering units. Data is automatically recorded by a Model 33 Teletype Unit which has print-out and/or punch-tape capability.

Ten thermocouple channels were available with direct readout in millivolts to three decimal places. The system was calibrated by inputs from a Leeds and Northrop Calibration Standard. This readout was further checked during the tests by comparing the signal from the system output monitor with those read on a precision potentiometer.

Ten channels were used for strain data, each having a completely isolated, full-floating power supply and separate signal-input conditioning. The input conditioning cards contained provisions for bridge-completion, calibration, and balance-limit resistors (Fig. 15). A balance potentiometer was provided to initially balance the bridge output to zero. The value of the limit resistor ($R_{Limit}$ in Fig. 15) was chosen to provide sufficient balance adjustment range, yet minimize the shunting effect of the balance network on the bridge. Span adjustments were made by adjusting the bridge excitation, which was maintained by the constant voltage mode of the power supplies. A calibration resistor mounted on the strain-gage conditioning card could be shunted across the active gage leg of the

bridge by a toggle switch mounted on the front control panel, which operates through a switching relay. The resultant change in resistance produced by the high-resistance shunt simulated a strain in the active leg of the bridge. Using this procedure prior to a run, each bridge output channel was balanced to zero; then, with the calibrate switch on, it was possible to adjust the span control for calculated bridge output, so that each channel was read out directly in microinches/inch strain.

The data system was located in the main control room of the Turbo-Propulsion Laboratory requiring about 60 feet of instrumentation leads between the slip rings of the turbine rotor and the signal-input conditioning cards. A shielded 38-conductor cable with matched 20-gage lead wires was used for these connections. A switching arrangement was provided at the data system so that the cable could be used for any combination of strain-gage and/or thermocouple inputs.

## D. INSTRUMENTATION OF TEST ROTOR

The turbine rotor was disassembled and cleaned prior to installing high-temperature strain gages and thermocouples. All gages, wiring, and residue from the preliminary tests were removed. The new gage lead wires were attached to the gage by silver brazing prior to installation on the test rotor. Heat sinks were used to reduce heating of the gage sensing element during lead attachment. Forty-two high-temperature gages were mounted on the rotor disks by following the same procedure as used with the test gages on the calibration beam. The gages were mounted in pairs, with one aligned radially and the other tangentially, having their equivalent centers at the same radius. Figure 17 shows a typical gage alignment and thermocouple installation. For purposes of wiring changeovers and data recording, the gages were identified corresponding to rotor-disk face, gage radius, and alignment. For instance, the designations 1-6.350R and 1-6.350T refer to the radial and tangential gages at the 6.350 inch radius on Face 1. The rotor faces were identified as:

Face 1 = Outer surface of stage 1
Face 2 = Inner surface of stage 1
Face 3 = Inner surface of stage 2
Face 4 = Outer surface of stage 2

Radial positions of the pairs of strain gages and thermocouples on the rotor are shown in Fig. 5.

The gage bridge circuitry is shown in Fig. 15. The gage and lead-wire resistances were measured, and a calibration set point was calculated for each installed gage using a 50-Kohm shunt resistor as described earlier. The calculated values varied from 1,309 to 1,386 microinches/inch, depending on gage resistance and length of Nichrome lead wire between the gage and the hub terminal connector. The lead wires through the slip rings and the matched conductors to the data system were assumed to have equal resistances.

The iron-constantan thermocouple junctions were made by spot welding the thermocouple wires directly to the rotor disk (Fig. 17). A thermocouple was placed at each strain-gage location to provide temperatures for apparent strain corrections. Figure 5 also shows the locations of additional thermocouples to establish the disk temperature profiles. The thermocouple lead wires were also connected to the hub terminal connectors of Figs. 6 and 12. Since copper lead wires were used from the hub terminal connector to the slip ring, the connections at this location constituted the reference junctions for all thermocouples on the rotor. A separate thermocouple was placed at the hub terminal connector with its iron and constantan wires extending through the hollow spindle. These wires were connected to the lowest slip-ring connector forming the reference junction of this thermocouple. The temperature at this junction was determined by another thermocouple located as closely as possible to this slip-ring connector. It measured the slip-ring temperature with respect to a $32^{o}F$ electronic reference junction manufactured by Pace Engineering Company. The general wiring system for the temperature measurements is shown in Fig. 18. The temperature at a location on the rotor is obtained by adding the measured temperature differences $\Delta T_1$, $\Delta T_2$, and $\Delta T_3$ of Fig. 18. The validity of this procedure was verified by taking direct

thermocouple readings from the stationary rotor with respect to the 32°F reference junction. This approach used the minimum number of thermocouple lead wires , which was of importance because of limited slip-ring capacity, and allowed the maximum choice in combination of strain and/or temperature measurements for any run.

## VI. ROOM-TEMPERATURE SPIN TESTS

The room-temperature tests of Section IV.B were repeated using the high-temperature instrumentation and data acquisition system described above, to verify and possibly improve the accuracy of the earlier-acquired test data. Changes were made before the test to correct several problems and deficiencies that were encountered during the previous runs.

### A. EQUIPMENT CHANGES

New attaching bolts were obtained for these tests, as mentioned in Section IV C. They were manufactured from the same material as the original ones but with the nominal central shaft diameter increased from 0.313 inch to 0.323 inch. Two special test specimens, also made from the same material, were subjected to tensile tests; and the results are discussed in Appendix C.

The lead weights previously added at the blade shrouds for wheel balancing were removed, and similar weights of stainless steel were prepared for the high-temperature runs. The heaviest of the weights was 40 grams and would have spanned about four blade segments on the shroud. Because of the difficulty in attaching and contouring the weight precisely to the shroud ring and the possibility that the centrifugal forces on the weight could be concentrated at as few as two points on the shroud, it was decided to carry out the tests without these balancing weights. Table B 1 of Appendix B indicates that a stainless-steel balance weight would increase blade-disk attachment stress by nearly ten per cent. This decision was also influenced by test experience and confidence gained during the previous runs, which indicated that balance weights would not be necessary.

## B. TEST PROCEDURE

Test procedures were basically the same as those used for the preliminary tests. Ten gages at a time were connected through the slip rings to the data system. Each gage channel was balanced for zero bridge output, and the calibration step was adjusted for the exact value calculated for the individual gage being measured. After the rotor was brought up to a predetermined speed, the slip rings were closed to apply excitation power simultaneously to all connected gages. After about 30 seconds for the stabilization of the gages, the scan cycle was initiated on the data acquisition system. Scan rate was two seconds per channel; and since each channel was recorded twice, a complete cycle required only about 40 seconds. The slip rings were then opened, and the speed was increased for the next data point. This procedure was carried out at speeds of 1,000, 1,500, 2,000, 2,400, 2,800, 3,000, 3,200, 3,400, 3,600, 3,800, and 4,000 rpm. From 4,000 rpm the speed was reduced by applying braking air to the drive turbine. During the slowdown, data were usually recorded at three or four of the above-listed speeds to check the repeatability of the test data. After the rotor was stopped, the zero and calibration data were again recorded and compared with those at the start of the test. Plots of strain vs. $(\text{rpm})^2$ were then established for each gage to evaluate the gage performance over a number of runs.

Changeover for the next run required disconnecting various air, lube-oil, and instrumentation leads, bleeding off tank vacuum pressure, and raising the tank cover with the suspended rotor. Lead wires from the slip rings were unsoldered at the hub terminal block and resoldered to other strain-gage or thermocouple connectors. This lead wire changeover was very time-consuming but resulted in better test data and fewer runs. Usually only one run per day could be completed. A physical inspection was made of the rotor, attaching bolts, and instrumentation leads at each wiring changeover.

Some of the gages became inoperative during the tests, and unfortunately most of these were located on Face 2. It is believed that their gage lead wires were pinched at the point where they passed between the rotor disk and the hub assembly (Fig. 6) and were grounding out. To correct this condition would have required complete disassembly of the rotor at the hub and extensive rewiring at the hub connector. A single gage had been mounted axially on the spacer drum of the second-stage rotor to find out at what operating conditions the rotor disks came into positive contact at the spacer. This was one of the gages which became defective

C. RESULTS AND DISCUSSION

In Ref. 5 it is shown that the stresses induced at a point in a rotating disk by centrifugal forces and bending moments are proportional to the square of the angular velocity. Since for assumed elastic behavior the stress-strain relationship is linear, plots of measured strain vs. $(\text{rpm})^2$ should result in straight-line relationships. This consideration was used in the data reduction.

The strain data for each individual gage and spin test run were plotted vs. $(\text{rpm})^2$ and approximated by a straight line giving minimum deviation. At least two sets of data were available for each gage, and as many as four were available for most gages. Since data scatter was greatest at low speeds, the only data obtained above 2,000 rpm were used in establishing the plots. The data scatter about the straight lines obtained was very small and generally less than three per cent of the average value.

An average straight line was drawn for each gage to represent a best average of the combined data from all runs. The heavy lines in Fig. 19 show the average strain values for four typical gages on Face 1, together with bands within which the actual test data scattered about the average line. At 4,000 rpm the maximum deviation from the average line was about $\pm$ 4.5 per cent. This is an indication of the repeatability of the strain readings taken during different runs. The slight variations from run to run can be attributed to wear in the slip-ring contacts over a period of time, which affected the contact resistance.

The straight-line plots of Fig. 19 indicate a small value of strain at zero rpm. This condition cannot occur in reality and must be due to a step change in slip-ring contact resistance, which occurs with rotation after the gage bridge has been balanced at zero rpm. To correct for this condition, these residual strains were uniformly added to or subtracted from the values given by the average lines of Fig. 19 to obtain the corrected curves of Fig. 20. Strain data recorded from each gage were corrected in this manner. The corrected centrifugal strain values for all gages at 4,000 rpm are shown in Table 4.

An additional spin test was made to further verify the data reduction procedures described above. Radial gages at the same radius on opposite faces of a single disk were connected into adjacent legs of the strain bridge. In this two-active gage, half-bridge configuration, differences in strain between the opposite gages were measured directly. These test data were also plotted vs. $(\text{rpm})^2$ and checked for linearity. The corrected values were then compared with the algebraic differences of data previously obtained by using single gages. The maximum vibration was less than three per cent, indicating good reliability of the test data.

No evaluation was made in the test program to determine the averaging effects of the long gage length when used in steep strain gradients. The averaging effect could cause a gage to indicate a lower than actual strain value, especially in the region of peak radial strains.

It should be noted that the gages near the hub (radius less than five inches) are on the straight and reinforced portion of the disk near the bolt circle. The influence of this geometry is especially evident in the tangential strains obtained from the outer faces at radii of 4.0, 4.29, and 4.90 inches.

The measured and corrected 4,000-rpm centrifugal strains of Table 4 were plotted vs. a dimensionless radius ratio $r/r_m$, where $r_m$ was chosen as the mean turbine-blading radius which equals 16.5 inches in accordance with Ref. 1. The resulting radial and tangential strain distributions on each face of the rotor are shown in Figs. 21 and 22. It was not possible to accurately establish strain distributions at small radii near the hub.

The available data indicate that strain changes rapidly with radius in the hub region, particularly by changes in the thickness of the disks and the presence of the bolt holes. The strain distributions shown by broken lines in Figs. 21 and 22 are included only to indicate how the strains might behave in the hub region. The limited data available and the variable geometry prevented accurate estimation of strain distributions in this region. The shape of the broken curves was based on the following considerations:

a. The centrifugal strain data of Table 4 was assumed to be valid, even that which indicated unusual strain distributions, since it had been verified by several runs as explained above.

b. It was assumed that the strain distributions on both outer faces must be of similar shape, as must those on the inner faces, since the two disks are geometrically similar. With this assumption the strain distribution on a particular face was drawn considering both the data taken on that face and the data taken on the geometrically similar face. For example, Fig. 21 shows a large dip in Face 1 of $\epsilon_t$ at $r/r_m = 0.265$ although there is no data at this radius. However, a tangential gage at $r/r_m = 0.26$ on Face 4 indicates that such a dip occurs (Fig. 22); and since the two faces are similar, it is assumed to also occur on Face 1.

c. When the data indicated a sharp change in strain, it was attempted to locate these changes relative to points of changing geometry, such as at the tangent points and at the outer radius of the parallel face lugs.

The radial strain at the disk inner radius ($r/r_m = 0.2$) was not measured but was determined from the compatibility equations (given below) and the condition of zero radial stress at this radius.

Once the strain curves were established, stresses were determined with the compatibility relations for two-dimensional stress conditions in an elastic body

$$\sigma_r = \frac{E}{1 - \nu^2} (\epsilon_r + \nu \epsilon_t) \quad (1)$$

$$\sigma_t = \frac{E}{1 - \nu^2} (\epsilon_t + \nu \epsilon_r) \quad (2)$$

where

$\sigma_r$ = radial stress, psi

$\sigma_t$ = tangential stress, psi

$\epsilon_r$ = radial strain, micro in/in, from Figs. 21 and 22

$\epsilon_t$ = tangential strain, micro in/in, from Figs. 21 and 22

$E$ = Young's modulus = 29.6 ($10^6$) psi at room temperature

$\nu$ = Poisson's ratio = 0.29 at room temperature

Using these relationships, radial and tangential stresses were calculated at each radius where strains were measured, as well as at several intermediate radii.

The centrifugal stresses in a disk with constant mass density $\rho$ rotating with the angular velocity $\omega$ are proportional to the quantity $\rho\omega^2$. A thin rotating ring of the disk material with radius $r_m$ has the hoop stress

$$\sigma_R = \rho\omega^2 r_m^2 \quad (3)$$

Hence, the measured disk stresses can be presented in dimensionless form as ratios with respect to $\sigma_R$. For convenience the radius $r_m$ is taken as the mean radius of the turbine blading. Then

$r_m$ = 16.5 inches

$\rho$ = 7.693 ($10^{-4}$) lb-sec$^2$ - in$^{-4}$ for Inconel 718

$\omega$ = angular velocity, radians/sec

The stresses calculated by Eqs. 1 and 2, divided by $\sigma_R$, are plotted in Figs. 23 and 24 as functions of the radius ratio $r/r_m$. These curves can be used to determine the centrifugal stresses in all geomentrically similar rotors with different material densities that operate at arbitrary rotational speeds. As discussed above, the strains from which these curves were

calculated were duplicated to within $\pm$ 4.5 per cent on different runs, verifying the repeatability of the stress distributions. The stress distributions in the hub region are shown by broken lines to indicate that they were calculated from the estimated curves of Figs. 21 and 22. Figures 23 and 24 show the tangential stress at the inner bore of the disks where a tangential strain gage was mounted on each disk. With the assumption that the radial stress is zero at this radius, the tangential stress is $\sigma_t = \epsilon_t E$ (Hooke's law). The figures also indicate that the outer faces of both disks have similar stress distributions, as do the inner faces. This condition must be due to the geometric similarity of the disks. The maximum stress in the conical portion of the disks occurs at a radius ratio of about 0.33 on Face 4. At 4,000 rpm this stress is about 48.0 ksi in tension.

To obtain a qualitative comparison of the experimental stress distributions of Figs. 23 and 24 with those of a more conventional non-conical disk, a theoretical calculation is given in Appendix B.2 for a straight-disk replacement model of the second stage. As shown in Fig. B2, the conical disk is replaced by a straight disk of constant thickness which is attached to another ring of constant thickness that substitutes for the rim. The centrifugal forces of the blades and the shroud are distributed equally over the outer periphery of the rim, producing a uniform radial stress $\sigma_{r3}$. In the following discussion, the disk of the replacement model will be referred to as the straight disk.

The centrifugal stresses in the straight disk are shown by the solid lines of Fig. B4. These theoretical curves point out that if the radial stress is assumed to be zero at the inner radius of the disk, the tangential stress has a maximum at this station. A sharp drop of this stress is followed by a gradual decrease at larger radii, whereas the radial stress has a maximum at an intermediate radius and then decreases slightly toward the outer periphery. The entire disk is in tension.

The general nature of the experimental stresses in the conical disks of Figs. 23 and 24 and their deviations from the theoretical stresses in the straight disk can be summarized as follows:

Outer Faces 1 and 4. The experimental radial stresses have much more pronounced and higher maxima than the theoretical stresses in the straight disk, occuring at radius ratios between 0.325 and 0.425 instead of about 0.55. They are about twice as high as the maximum radial stress in the straight disk. However, at the outer radius of the disk where the theoretical stress ratio $\sigma_r/\sigma_R$ is about 0.5, the experimental stresses are zero on Face 1 and negative on Face 4. Contrary to the theoretical stress distributions, the experimentally determined tangential stresses decrease from a maximum at $r/r_m$ of about 0.5 toward the hub and toward the outer periphery. Except for the disk portions near the hub, the experimental tangential stresses have the same order of magnitude as the theoretical ones. At the inner bore the ratios $\sigma_t/\sigma_R$ for the first and second stages of the rotor are about 1.6.

Inner Faces 2 and 3. The stress distributions on the inner faces of the test rotor differ considerably from those on the outer faces and have little resemblance to the theoretical ones. The radial stresses are zero or negative in the mid-portions of the disks and increase sharply toward the rims. The tangential stresses exhibit a minimum near $r/r_m$ equal to about 0.5, reach values similar to those on the outer Faces 1 and 4 at larger radius ratios, and increase gradually to their maxima at the inner bore.

The differences in stress distribution relative to those in the straight disk are due to the special geometry of the test rotor. Bending moments are produced in the conical disks by centrifugal forces which pull the disks toward each other. These moments are redistributed in complex manner if the disks contact at the spacer drum. Both the sharp increase of the inner-face stresses and the change of the outer-face radial stress into compression at large radii result from these bending moments. In addition to this effect, the hub geometry influences the stress distributions. It is probably responsible for the condition that the tangential stresses at the outer faces tend to decrease near the hub and then to

increase sharply at the inner bore of the disk.

The centrifugal stresses for a rotor speed of 6,100 rpm were calculated from Figs. 23 and 24 to establish the stresses which occurred during the fabrication-evaluation tests discussed in Section IV.B.3. As indicated in Section IV.B.3, it was not possible to measure strains at 6,000 rpm due to strain-gage and lead-wire failures. The reference stress $\sigma_R$ at the maximum speed of 6,100 rpm is 85.464 ksi by Eq. 3. Actual stresses are found by multiplying the dimensionless ratios of Figs. 23 and 24 at chosen radii by $\sigma_R$. The results are shown in Figs. 25 and 26, which represent the maximum centrifugal stress levels at which the wheel was operated at room temperature.

## VII. ELEVATED-TEMPERATURE STATIC TESTS

### A. PREPARATION FOR TEST AND PRELIMINARY RUNS

The objective of the elevated-temperature tests was to subject the rotor to radial temperature gradients in order to induce thermal stresses which could be determined from measured thermal strains. The induction heater assembly and hub cooling plates (Section III.C.5) were installed and adjusted around the rotor as shown in Figs. 10 and 11. These assemblies were readjusted after the preliminary runs to reduce the axial temperature gradients across the rotor.

Preliminary runs were made at several induction-heater power inputs to evaluate the influence of the induction field on thermocouple readings. Readings were taken both with the electric power turned on and switched off. It was found that heater power inputs of more than five kW caused some of the thermocouples to indicate values as much as 50 per cent lower than those corresponding to the actual temperature. Strain-gage readings were only slightly affected by the heater induction field. These tests established the requirement that the heater power must be turned off during data taking in order to obtain valid thermocouple data.

Prior to this discovery and based on observed heat rates of less than $3^{\circ}F$/min for five kW input, a preliminary run was made at 4,000 rpm and an initial heater input of 15 kW. This load was reduced to 12.5 kW after 15 minutes, then five minutes later to ten kW. After about 55 minutes, loud noises were heard from the spin pit; and braking air was applied to stop rotation. The indicated disk rim temperature just prior to shut-down was $353^{\circ}F$. However, this reading was later found to be incorrect since it was taken with heater power on. Actual rim temperature was probably near $570^{\circ}F$, with a disk hub-to-rim temperature difference of about $430^{\circ}F$.

Subsequent inspection of the rotor revealed that the hub bolts were elongated by an average of 0.057 inch. In addition, lead wires were torn loose from Face 1, the spindle-shaft oil seal was damaged, and a number of bolts in the catcher assembly were loose. Except for the hub-bolt elongation, the rotor was not damaged. This was verified by detailed examinations and measurements of critical dimensions. Apparently the problem was initiated by bolt stretching, which allowed the disks to move axially, resulting in hooking of lead wires on the lower nuts of the hub cooling plates (Figs. 10 and 12). Eventually this occurred with sufficient force to displace the rotor and to set up oscillations, which damaged the spindle-shaft oil seal and caused the arbor shaft to engage the lower catcher assembly.

The damaged lead wires and gages were replaced. Since there were indications that high temperatures were causing lead-wire insulation to become brittle, teflon sleeves were slipped over all gage lead wires to prevent electrical shorting. The rotor was reassembled with the same bolts, which were carefully torqued to 80 inch-pounds. The gap at the rotor-drum spacer remained at 0.003 to 0.004 inch. A new spindle shaft and oil seal were installed, and the catcher-assembly anchor bolts were safety wired to prevent loosening. The rotor was reinstalled in the spin pit, and checks were made to insure proper operation.

After reinstallation of the heater and cooling plate assembly, a number of high-temperature runs were made at various heater power settings to establish the optimum heating schedule, namely, one which would provide the largest stable temperature gradient from disk hub to rim while maintaining all temperatures below the maximum allowable strain-gage temperature of 650°F. Significant characteristics of the temperature profiles, produced by some of the power inputs which were considered, are shown in Table 5. The two-hours-at-six-kW heating schedule was chosen as the most suitable one since it produced a relatively large temperature difference and a fairly stable profile. This latter consideration was important to insure that significant temperature changes did not occur while the heater was turned off during data taking. As Table 5 shows, a combined heat schedule, such as 2.5 hours at six kW followed by holding at 3.8 kW, was closest to a steady-state situation. However, to obtain a higher temperature difference with this type of heat schedule would have required a more effective hub cooling technique than the one which was available.

These tests established the so-called standard heat schedule, henceforth referred to as a standard run. This schedule consisted of heating for 2.0 hours at six kW input followed by cooling to room temperature, while maintaining rotor speed at 200 rpm throughout the run to insure uniform heating and cooling. A typical run from room temperature to maximum temperature and cooling to room temperature required a full day. This standard heating and cooling cycle was used in all subsequent testing.

## B. TEST PROCEDURES

As in previous tests, the number of available slip-ring channels limited the amount of data that could be recorded during a particular run. The combination of gages and thermocouples selected for a run was either six gages and eight thermocouples or eight gages and five thermocouples. A typical run consisted of four gage pairs (radial and tangential) at different radii on one rotor face and a thermocouple at each radial location.

The thermocouple at r = 13.0 inches on Face 1 was monitored on every run and served as a reference point in comparing data from different runs.

Maximum hub-cooling water flow was used on all runs, and the rotor was cooled to minimum temperature prior to start of a run. The strain bridge was balanced for zero output, and the calibration adjustments were made after the rotor speed was stabilized at 200 rpm and just prior to turning the heater on. The thermocouple channels were calibrated using a L-N calibration standard, and readings were periodically cross-checked using a precision potentiometer.

Heater power input was set and maintained at six kW with the power factor at unity. Temperature and strain data were recorded at 15-minute intervals during rotor heat-up. Slip rings were closed one minute before data recording to permit strain readings to stabilize. The heater load coil was disconnected during all data recording, which required about one minute for scanning all inputs twice. The heater was turned off after two hours, and the rotor was permitted to cool down. Data were recorded at 30-minute intervals up to three hours after the power was shut off. Approximately 12 hours were required for complete cool down to room temperature.

The test data were corrected for reference-junction temperatures and apparent strains. Rotor-disk temperatures were obtained by adding the terminal connector and slip-ring reference-junction millivolt readings to the measuring-junction reading and using standard conversion tables to convert to $^{o}F$. The measured strain values were corrected for apparent strain using the corrected temperature for the gage location and the apparent strain vs. temperature curve of Fig. 16.

## C. RESULTS AND DISCUSSION

In Fig. 27 is shown the temperature profile on Face 4 recorded at several times during a standard run. Similar profiles were obtained for Faces 1, 2, and 3 during other standard runs. The temperature profiles

on the four faces could not be compared directly since slip-ring limitations necessitated a separate run to obtain each profile, and slight variations in heat input caused by inaccuracies of the heater control were inevitable from run to run. However, an accurate comparison was obtained by monitoring the thermocouple at the 13-inch radius on Face 1 during the runs for Faces 2, 3, and 4, and then referencing this reading and all other thermocouple readings recorded during the runs to the Face 1 test data. Figure 28 shows the results and establishes the axial temperature variation between rotor surfaces at the 2.0 hour point of a standard run. The first-stage disk was generally cooler than the second-stage disk, probably because of its larger diameter. Temperature profiles obtained at other time intervals showed relationships similar to those of Fig. 27.

As shown below, the thermal stresses induced by a given temperature profile were nondimensionalized to be independent of the overall temperature difference. Therefore, temperature profiles were also nondimensionalized to indicate the manner in which temperature is distributed across the disk, independent of the overall temperature difference. For a given temperature profile, there is

$$\text{Dimensionless temperature ratio} = \Delta T/\Delta T_{max} \qquad (4)$$

where $\Delta T$ = Temperature difference between radius of interest r and radius = 4.0 in.

$\Delta T_{max}$ = Temperature difference between radius = 12.3 in. and radius = 4.0 in.

Thus, the dimensionless temperature is that fraction of the total temperature difference which occurs from the inner radius, r = 4.0 inches, to the radius of interest. Values of $\Delta T_{max}$ are tabulated as follows:

| | 2.0 hr at 6 kW | 2.0 hr at 6 kW<br>1.0 hr at 0 kW |
|---|---|---|
| Face 1 | $\Delta T_{max} = 322.7^{o}F$ | $\Delta T_{max} = 128.3^{o}F$ |
| Face 2 | $= 321.6^{o}F$ | $= 143.6^{o}F$ |
| Face 3 | $= 395.8^{o}F$ | $= 124.7^{o}F$ |
| Face 4 | $= 398.0^{o}F$ | $= 124.1^{o}F$ |

Dimensionless temperature profiles for the 2.0-hour and 3.0-hour test points of a standard run are shown in Figs. 29 and 30 respectively.

The close similarity of the dimensionless profiles at the 2.0-hour point in Fig. 29 indicates that the temperature gradients are almost identical at all rotor faces. Figure 28 shows the actual temperatures on the four faces. However, Fig. 30 demonstrates that after one hour of cooling, this face-to-face similarity of the temperature distributions no longer exists, especially not between those on Faces 1 and 2 of the first-stage disk compared with those on Faces 3 and 4 of the second-stage disk. The variation in temperature profiles during the cooling is probably due to differences in geometry and position of the disks relative to the cooling plates. Such differences, commonly referred to as "configuration-factor effect", are unavoidable during installation and alignment of the rotor. Also the fact that the second-stage disk is hotter at the beginning of cooling (Fig. 28) undoubtedly contributes to the existence of a different type of temperature profile on this disk after one hour of cooling.

Although strain data were available for each profile shown in Fig. 27, as well as at several intermediate times, thermal stresses were calculated for only two times; at 2.0 hours representing the maximum temperatures reached by the rotor, and at 3.0 hours representing a typical cool-down gradient. A complete list of the strains measured at these conditons is given in Table 4. The strain data were plotted vs. radius ratio as shown in Figs. 32 through 35. The broken lines in the hub region of these figures provide qualitative indication of strain patterns, as was discussed in Section VI.C for centrifugal strains. The same considerations and

assumptions as described in Section VI were applied to obtain Figs. 32 through 35. The Face 2 data (Fig. 32) were taken early in the test program and were not verified due to failure of Face 2 instrumentation as described in Section VI. This failure also prevented obtaining Face 2 data at the 3.0-hour test condition. The Face-3 tangential strain gage at radius 11.02 inches was not operational during elevated-temperature tests. The strain curve was estimated by the broken line shown, based on the shape of the Face-2 tangential strain curve in this region.

Thermal stresses corresponding to the 2.0-hour and 3.0-hour test conditions were calculated by substituting the strains of Figs. 32 through 35 into Eqs. 1 and 2. Values of Young's modulus and Poisson's ratio were obtained from Fig. 31 at the appropriate temperatures. No account was taken of the centrifugal stresses at 200 rpm since they are negligible compared with the thermal stresses, and the gage bridges were balanced for zero output with the rotor stabilized at 200 rpm. The value of $\sigma_t$ at the inner bore was again obtained by assuming that the radial stress vanishes at the inner bore.

Since thermal stresses depend on the shape of the temperature profile, as well as on the value of the temperature difference $\Delta T/\Delta T_{max}$ between hub and rim, and the material properties, they cannot be nondimensionalized for completely general test conditions as can centrifugal stresses. However, for a temperature profile with equal temperature ratios $\Delta T/\Delta T_{max}$ they can be expressed as fractions of the thermal stress $\sigma_T$ that would exist in a bar of the rotor material that is completely restrained while its temperature is increased by $\Delta T_{max}$. This maximum possible thermal stress is

$$\sigma_T = E \alpha \Delta T_{max} \qquad (5)$$

where

$E$ = Young's modulus of rotor material

$\alpha$ = Coefficient of thermal expansion of rotor material

$\Delta T_{max}$ = Temperature difference between radii 4.0 and 12.3 inches.

Values of E are taken from Fig. 31 for the temperatures at the mean radius of 8.15 inches; and for the temperatures of the tests, an average value $\alpha = 7.7\ (10^{-6})$ in/in/$^{o}$F can be used.

The radial and tangential stresses calculated by Eqs. 1 and 2, divided by $\sigma_T$ of Eq. 5, are plotted in Figs. 36 through 39 vs. the radius ratio $r/r_m$ for the different dimensionless temperature distributions of Figs. 29 and 30. These curves can be used to calculate thermal stress distributions in geometrically similar rotors irrespective of the rotor material or the overall maximum temperature difference, provided that the dimensionless temperature profile corresponds to that shown in the appropriate figures. The statement that thermal stresses are independent of overall temperature difference $\Delta T_{max}$ is correct only if temperature independence of material properties is assumed. Although this assumption was not made for the thermal stress calculations, the errors that would occur with this simplification in the present temperature range would be within the measuring accuracy of the test data.

The tangential and radial strains used to calculate the stress of Figs. 36 through 39 were not averages of several runs but represent data from individual test runs. In order to estimate the repeatability of this data, thermal stresses were calculated from a limited amount of data available from other runs. These independent data were available at one radius on Face 1, three radii on Face 3, and one radius on Face 4. The stresses calculated from these data were found to be within $\pm$ 7 per cent of the points of Figs. 36 through 39.

Figure 36 shows that the highest thermal stress is a tensile stress on Face 1 in radial direction, at a radius ratio of about 0.34. For the test conditions, the value of this stress was about 50 ksi. It is of interest to note from Figs. 23 to 26 that the highest centrifugal stresses in the conical portions of the disks occur at about the same radius. These are also tensile stresses acting in radial direction. The figures indicate that the temperature distributions for two hours at six kW with one hour

cooling at zero kW produce stress distributions similar to those without cooling, but give somewhat smaller values. From the similarity of the stress distributions on Faces 2 and 3 of Figs. 36 and 37 it can be anticipated that the thermal stress distributions on Face 2 at the 3.0-hour test point must be similar to those on Face 3 of Fig. 39.

To investigate the effect of the conical arrangement of the disks on the thermal stress distribution, the thermal stresses in the straight replacement disk of Fig. B2 were calculated for a linear temperature profile, which closely approximates the temperature distribution at the 2.0-hour-at-six-kW heating schedule. These theoretical calculations are presented in Appendix B2, and the results are shown by the dashed curves in Fig. B4. The following conclusion can be drawn from a comparison of these curves with the experimental stress distributions of Figs. 36 and 37.

Outer Faces 1 and 4. Although similar in character, the measured radial stresses differ materially from the theoretical ones of the straight replacement disk. At a radius ratio of about 0.35, they are three times higher than those calculated; and whereas the straight disk has tensile stresses at $r/r_m = 0.75$, the measured stresses are compressive stresses of about the same magnitude as the maximum tensile stresses in the straight disk. At the inner bore, the ratio $\sigma_t/\sigma_T$ is about 0.925 and 0.71 for the first and second stage respectively compared to 0.68 for the straight disk. Outside of the hub region, the experimental tangential stress curves are similar in shape to that of the straight disk. At the outer-disk radii where the theoretical value of $\sigma_t/\sigma_T$ is about - 0.12, the experimental ratios are about - 0.3 on Face 1 and - 0.4 on Face 4, indicating that considerably higher compressive stresses will occur at these locations than those predicted with the simplified model of the straight disk.

Inner Faces 2 and 3. Although only limited data were available from Faces 2 and 3, it is evident that inner-face stress distributions are

quite different from those in the straight disk. This is particularly true of radial stresses, which become slightly compressive at $r/r_m$ near 0.4 and increase into tension at large radius ratio. Tangential stresses are more like those of the replacement disk since they decrease continuously into compression with increasing radius ratio. However, the slope of the experimental tangential stress curves changes rapidly over the disk, whereas that for the replacement disk is nearly constant.

It appears that the thermal loads applied, although much less than those which would exist in actual operation of the test rotor, were sufficient to cause bending moments in the disks similar to those discussed in earlier sections. These moments cause the outer-face radial stresses to become compressive, and inner-face stresses to increase in direction of tension at large radii. The disk geometry in the hub region probably causes the decrease in outer-face tangential stresses at small radii.

## VIII. ELEVATED-TEMPERATURE SPIN TESTS

### A. TEST PROCEDURES

Combined-loading tests, relatively few in number, were run near the end of the program. The rotor was loaded by spinning at 3,000 rpm. Simultaneously the temperature gradients of a standard elevated-temperature run were applied. A major objective of these tests was to compare the experimentally measured stresses to those obtained by adding the results of separate centrifugal (Section VI) and thermal (Section VII) stress tests, to verify that test results approximately correlate with the principle of superposition.

Rotor speed was limited to 3,000 rpm for the following reason. The strains from separate room-temperature spin tests and elevated-temperature static tests, when combined, indicated that for speeds greater than 3,000 rpm, rotor strain would exceed that at which bolt elongation occurred during the 6,100-rpm fabrication-evaluation run. Three thousand rpm was thus chosen as the maximum safe speed to prevent bolt elongation,

when applied in combination with the temperature gradients of the standard elevated-temperature run.

The procedures were basically the same as used for the elevated-temperature static tests described above, except that the rotor speed was stabilized at 3,000 rpm prior to application of heater power. Gage bridge circuits were balanced to zero, and calibration adjustments were made with the rotor at zero rpm. The rotor speed was then brought up and stabilized at 3,000 rpm. A set of strain data was recorded at ambient temperature and compared with previous 3,000 rpm data. After verifying the centrifugal strain values, the heater unit was started; and power was adjusted to maintain a constant six kW input to the load coil. Heating was continued for two hours; then power was turned off, and the rotor was cooled to ambient temperature. Rotor speed was reduced to 200 rpm after one hour of cool down (three hours total) and maintained until room temperature was reached. Both strain and temperature data were recorded, with heater power off, at 15-minute intervals during the run. Test data were corrected for thermocouple reference junction and apparent strains as described earlier. Slip-ring contact deterioration became so severe near completion of these tests that only data from Faces 3 and 4, taken early in the series, were considered reliable.

Following combined-loading tests the rotor was removed from the spin pit. Visual inspection indicated that no permanent geometry changes occurred during these tests.

## B. RESULTS AND DISCUSSION

The corrected values of strain were converted to stress using Eqs. 1 and 2 in Fig. 31. These results are shown by the points plotted in Fig. 40. These points represent the experimentally determined stresses due to combined loads at radii where radial and tangential strains were measured.

An important assumption often made in the analysis of members under combined loading is that material properties do not vary with temperature.

With this assumption the equilibrium, stress-strain, and strain-displacement relations are linear; and the superposition principle can be applied. In other words, thermal stress and rotational stress can be calculated separately and added to obtain the total stresses. For this program the assumption of constant material properties was not made. Instead, properties were considered to vary with temperature according to Fig. 31. However, for the temperature range considered, the effect of this variation on stress is very small; and the superposition principle should give results similar to those obtained by direct measurement of stresses due to combined loading. To verify this statement, the stress distributions for the combined 3,000 rpm and high-temperature test runs were calculated by adding the separate results of spin tests at 3,000 rpm to those of high-temperature tests after 2.0 hours at six kW, reported above in Figs. 24 and 37 respectively. The resulting stresses are shown by the broken lines of Fig. 40.

As expected, the results of superposition agree closely with the stresses measured directly during the combined-loading tests. This fact is significant for two reasons. First, it implies that the results of the separate spin and high-temperature tests can be combined to enable estimation of stress distribution for a variety of centrifugal and thermal load combinations. Secondly, the agreement furnishes a final verification as to the reliability and repeatability of the test data. The fact that three separate tests are involved in obtaining the data of Fig. 40, with the excellent correlation shown, emphasizes this latter point.

## IX. CONCLUSIONS

The centrifugal and thermal stress distributions in the M-1 engine oxidizer turbine test rotor were experimentally determined for several test conditions. Calculations made using data from duplicate runs indicated that the stress distributions were repeatable to within $\pm 4.5$ per cent for ambient-temperature centrifugal stresses, and to within $\pm 7.0$ per cent for thermal stresses.

The dimensionless stress distribution curves can be used to estimate stresses in any geometrically similar rotor, independent of rotor material, over a wide range of rotor speeds and thermal gradients. Within the temperature range considered, the superposition principle can be applied to estimate stresses due to various combined centrifugal and thermal loads.

The measured stress distributions differ significantly from those of a more conventional straight disk under similar loads. The conical shape of the disks, the contact which is established between disks under both centrifugal and thermal loads, and the bolted hub-disk attachment geometry are the primary features which cause these differences.

The mechanical integrity of the entire rotor assembly, tested under centrifugal and thermal loads for several hundred hours, was satisfactory at all test conditions. The only weakness discovered was hub-bolt elongation at certain high-load conditions. This weakness was traced to an improperly heat-treated bolt material and was not caused by faulty design.

Due to instrumentation and hub cooling coil limitations, it was not possible to test the rotor under the maximum thermal gradients expected in service. Hence, the mechanical integrity of the rotor at this condition remains uncertain. This situation is not likely to change until simple and reliable strain gages are developed for use at higher temperatures. However, it is believed that information obtained during this program at less severe thermal conditions will prove useful in refinement of analytical methods to accurately predict thermal stresses in the rotor caused by larger thermal gradients.

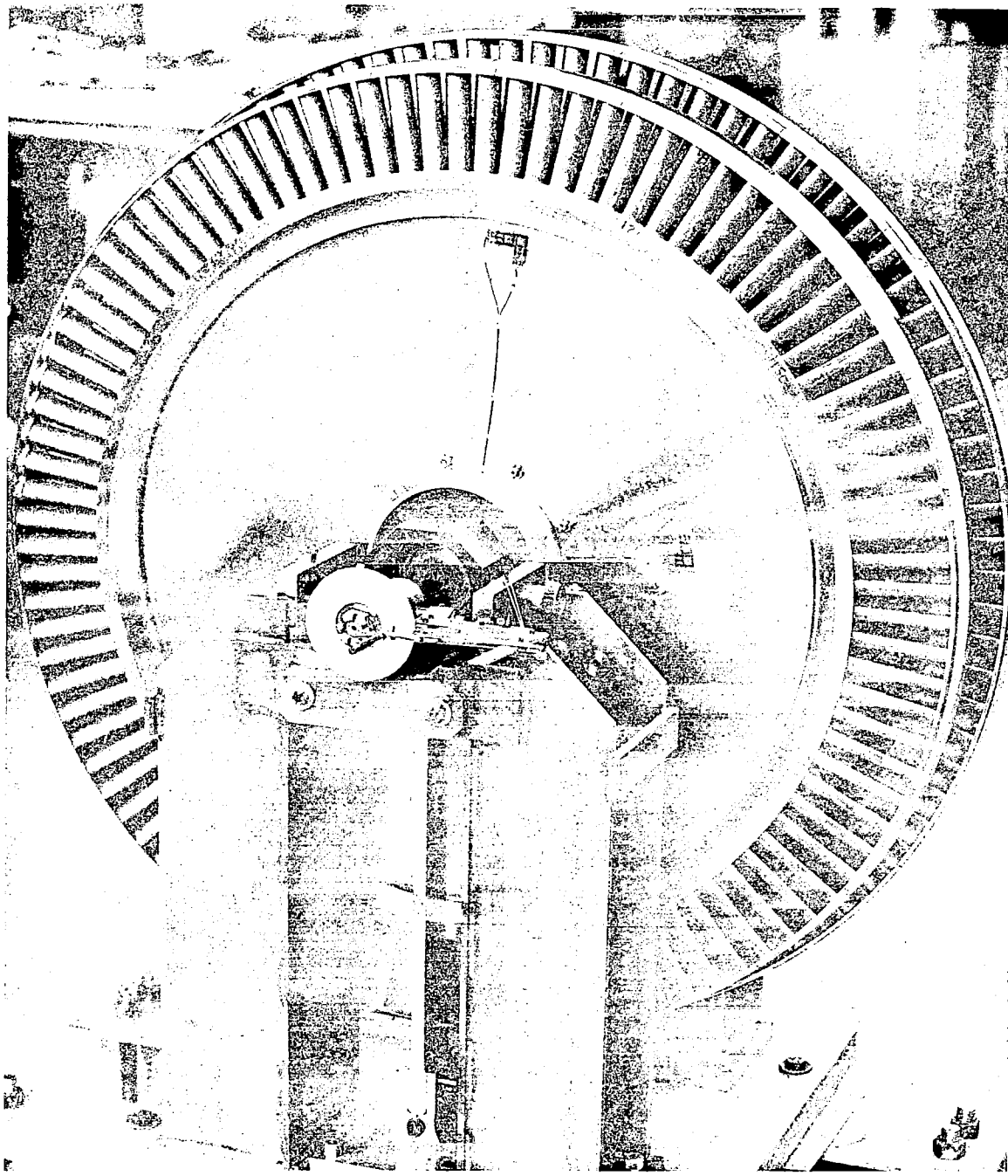

FIG. 1 TEST ROTOR MOUNTED IN MEASURING AND BALANCING RIG

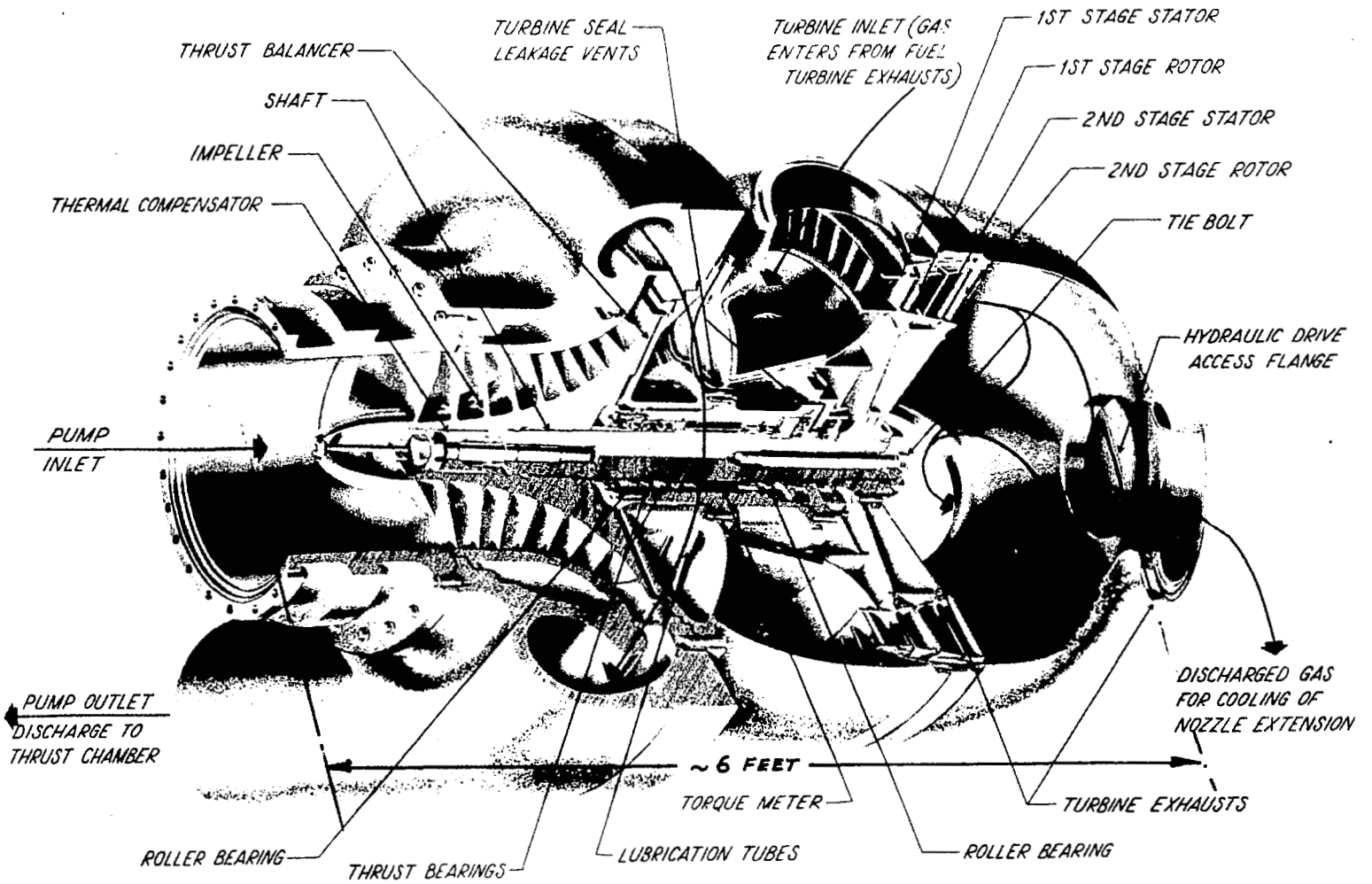


FIG. 2 OXIDIZER TURBOPUMP ASSEMBLY

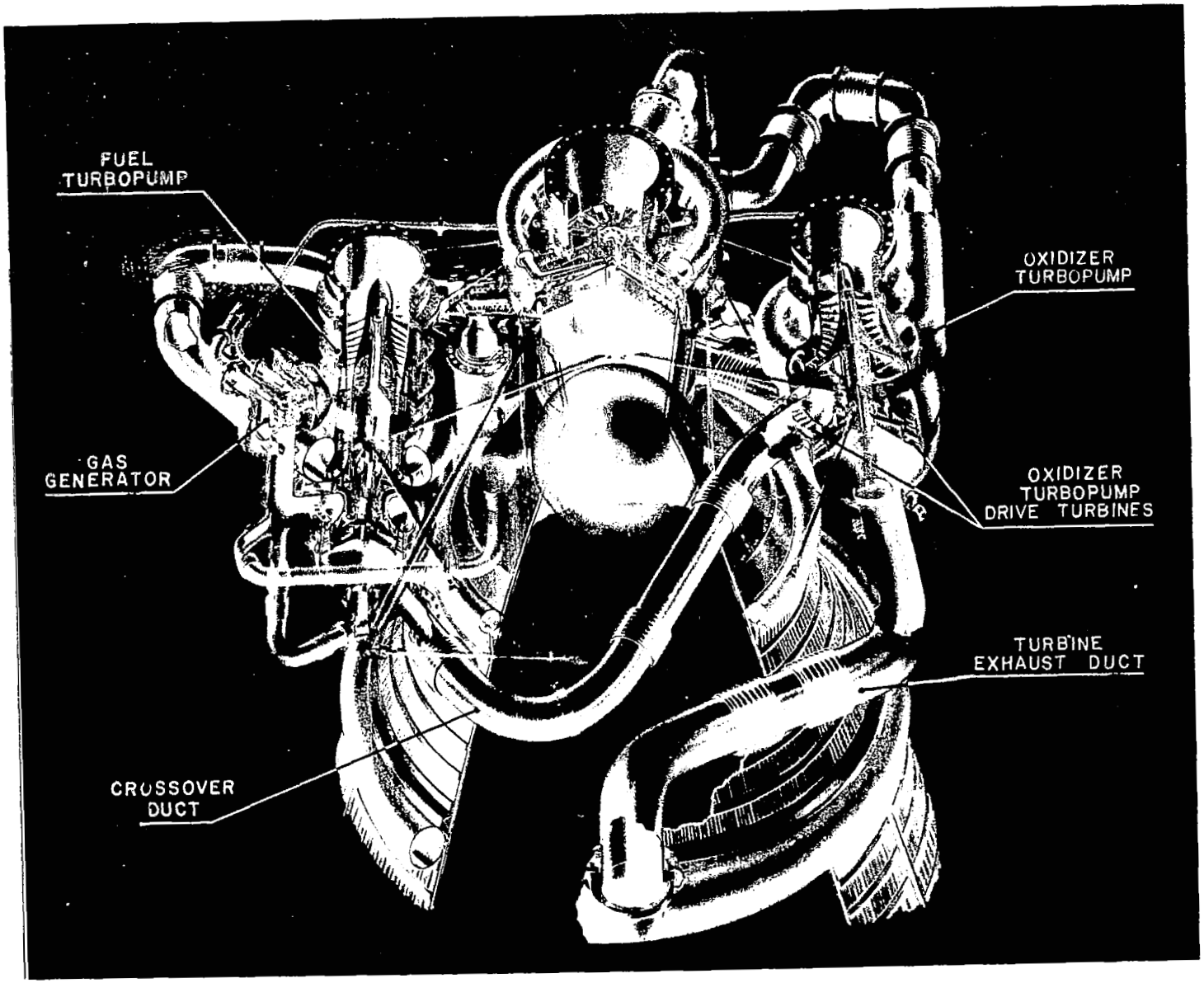


FIG. 3 M-1 ENGINE MOCKUP

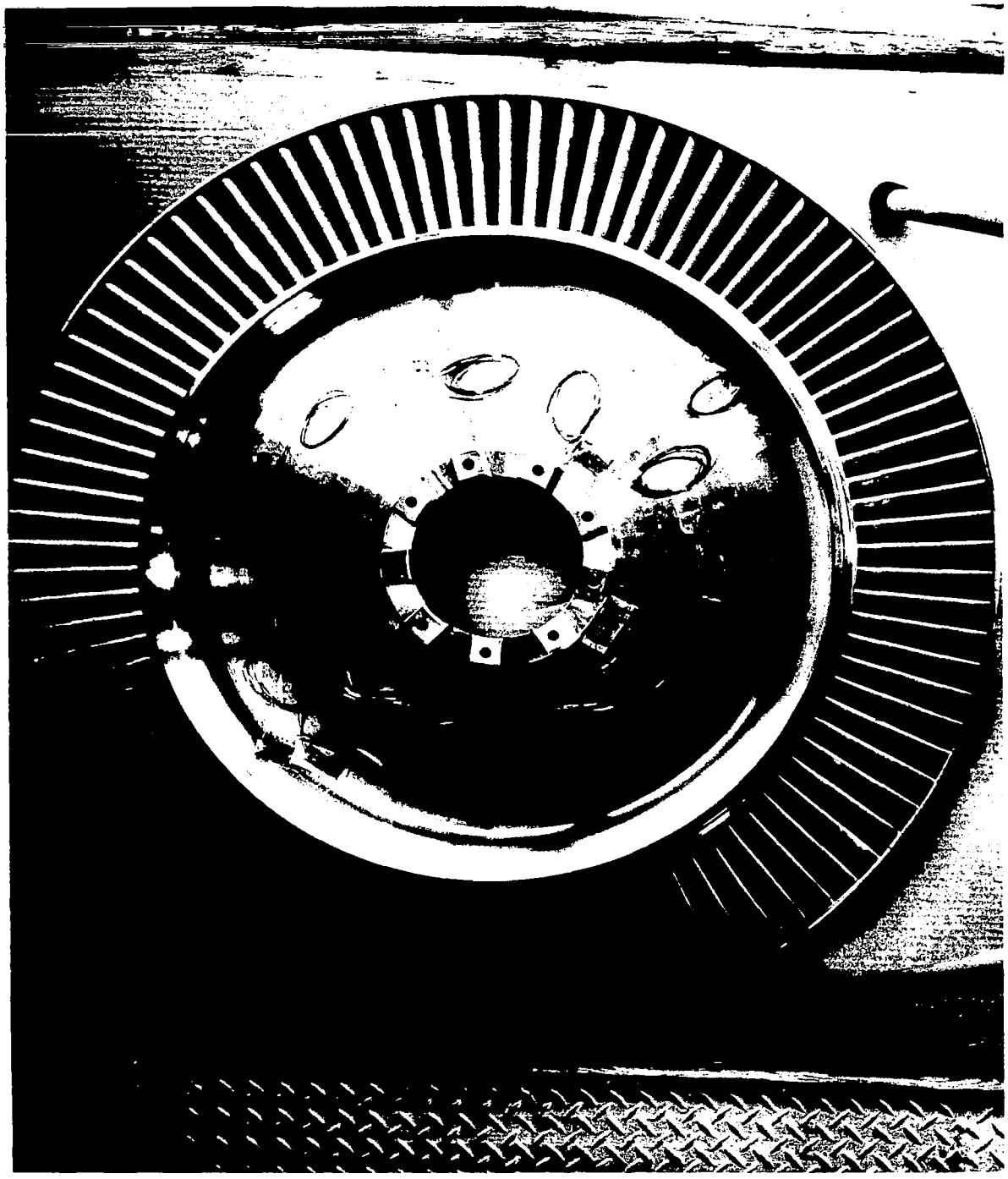

FIG. 4 INNER FACE OF SECOND-STAGE TURBINE

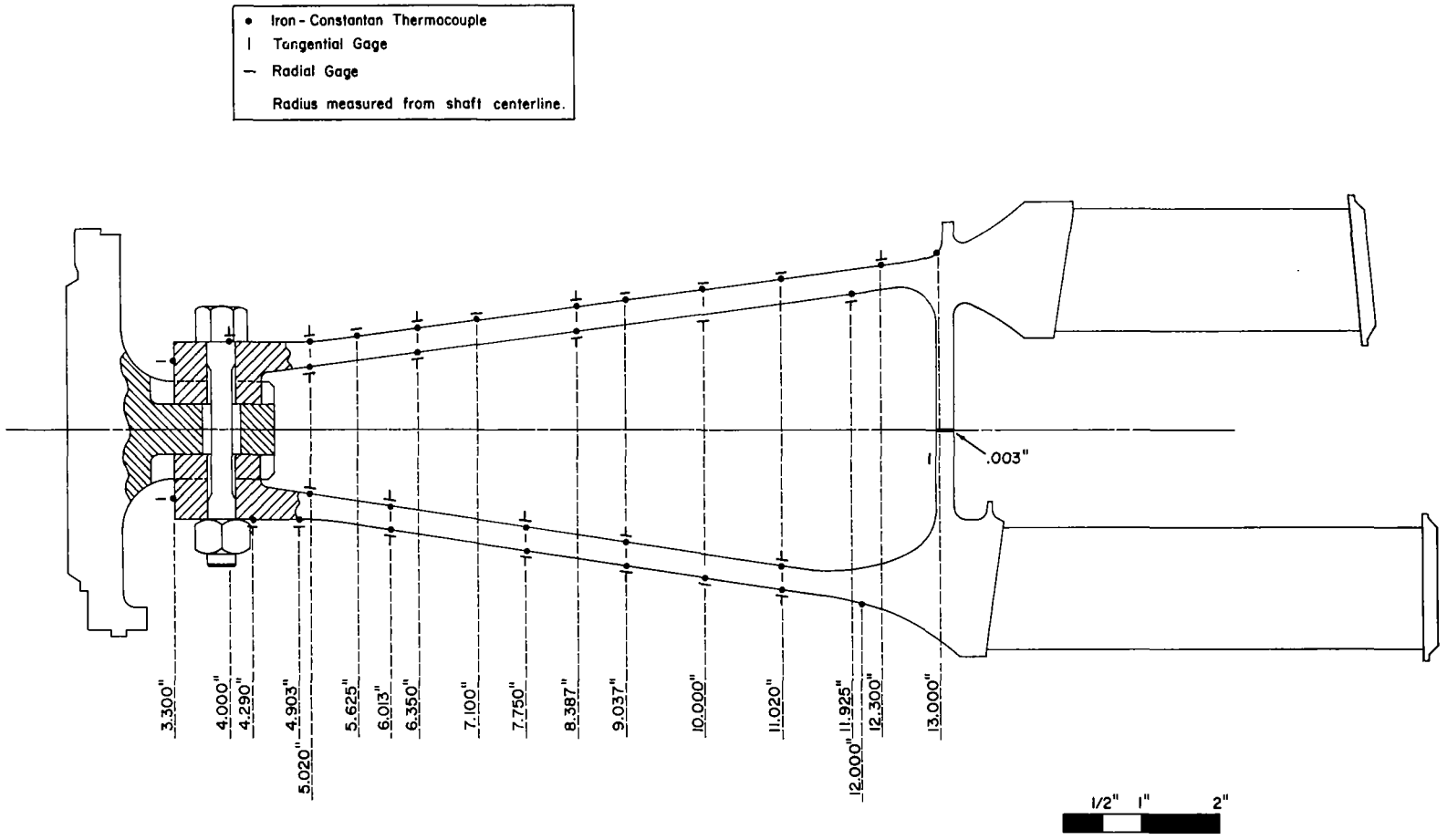


FIG. 5 STRAIN GAGE AND THERMOCOUPLE LOCATIONS - HIGH-TEMPERATURE INSTRUMENTATION

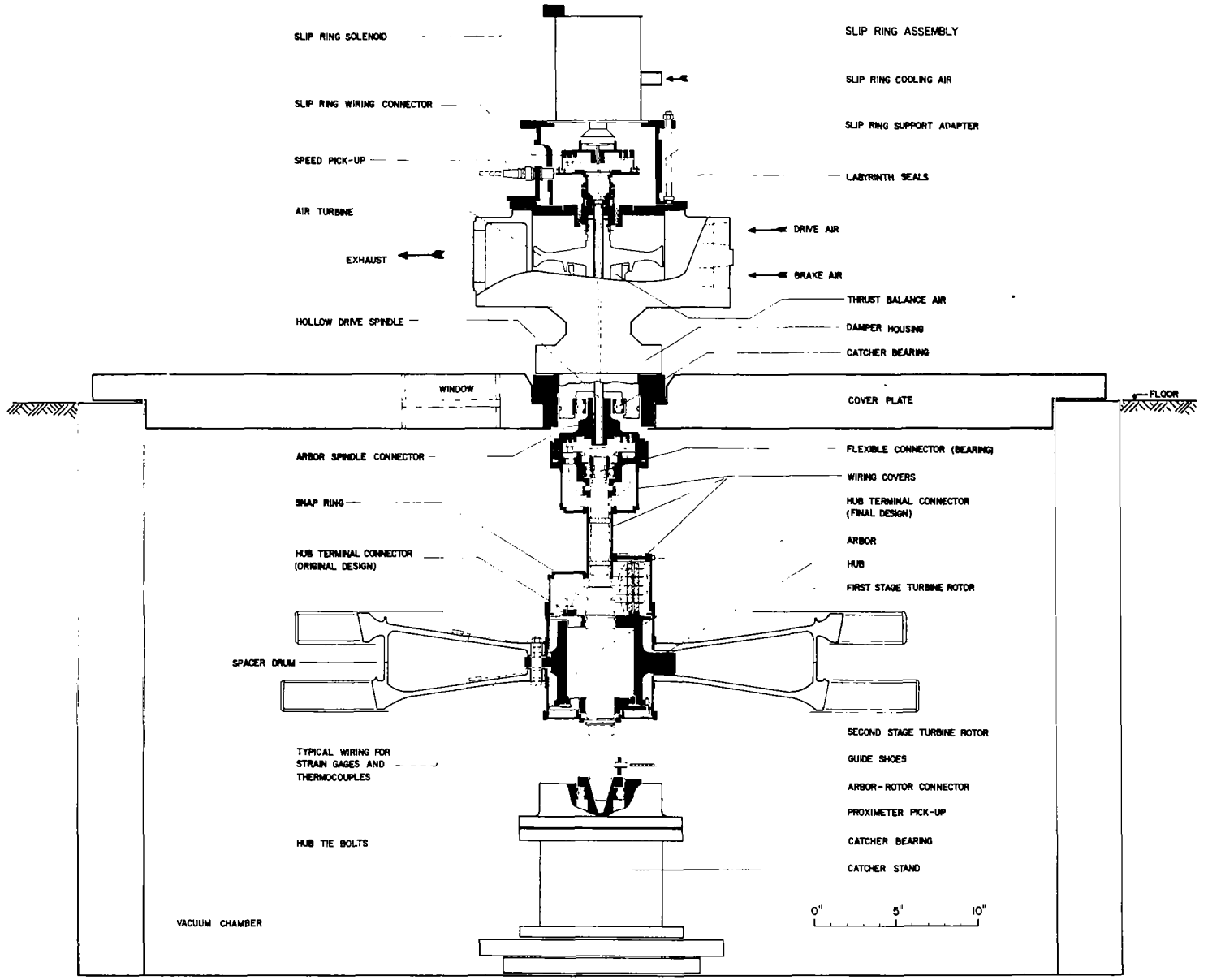


FIG. 6 CROSS SECTION OF TEST ROTOR IN SPIN PIT

FIG. 7 OVERALL VIEW OF HOT SPIN TEST FACILITY

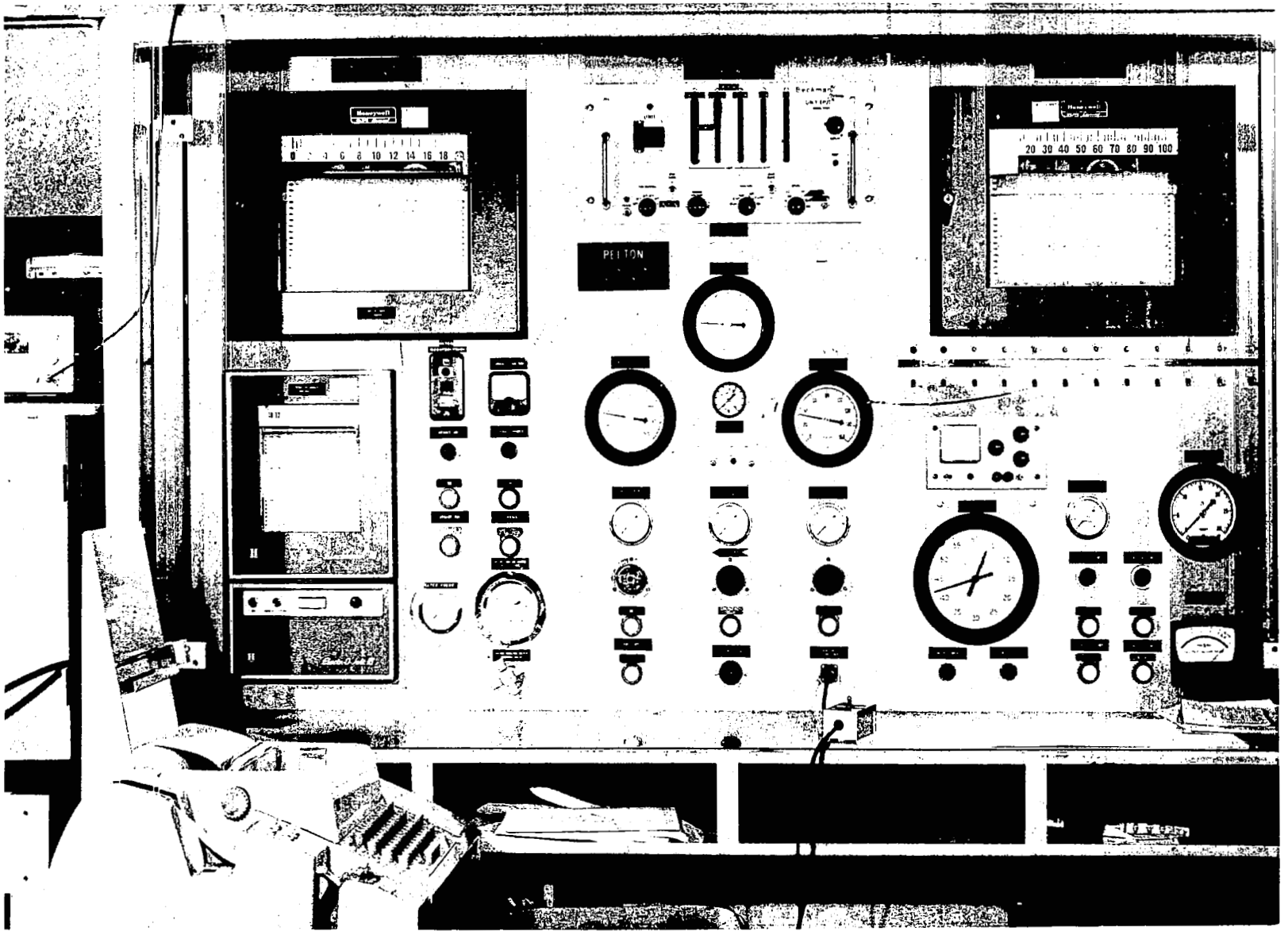


FIG. 8 HOT SPIN TEST UNIT CONTROL CONSOLE

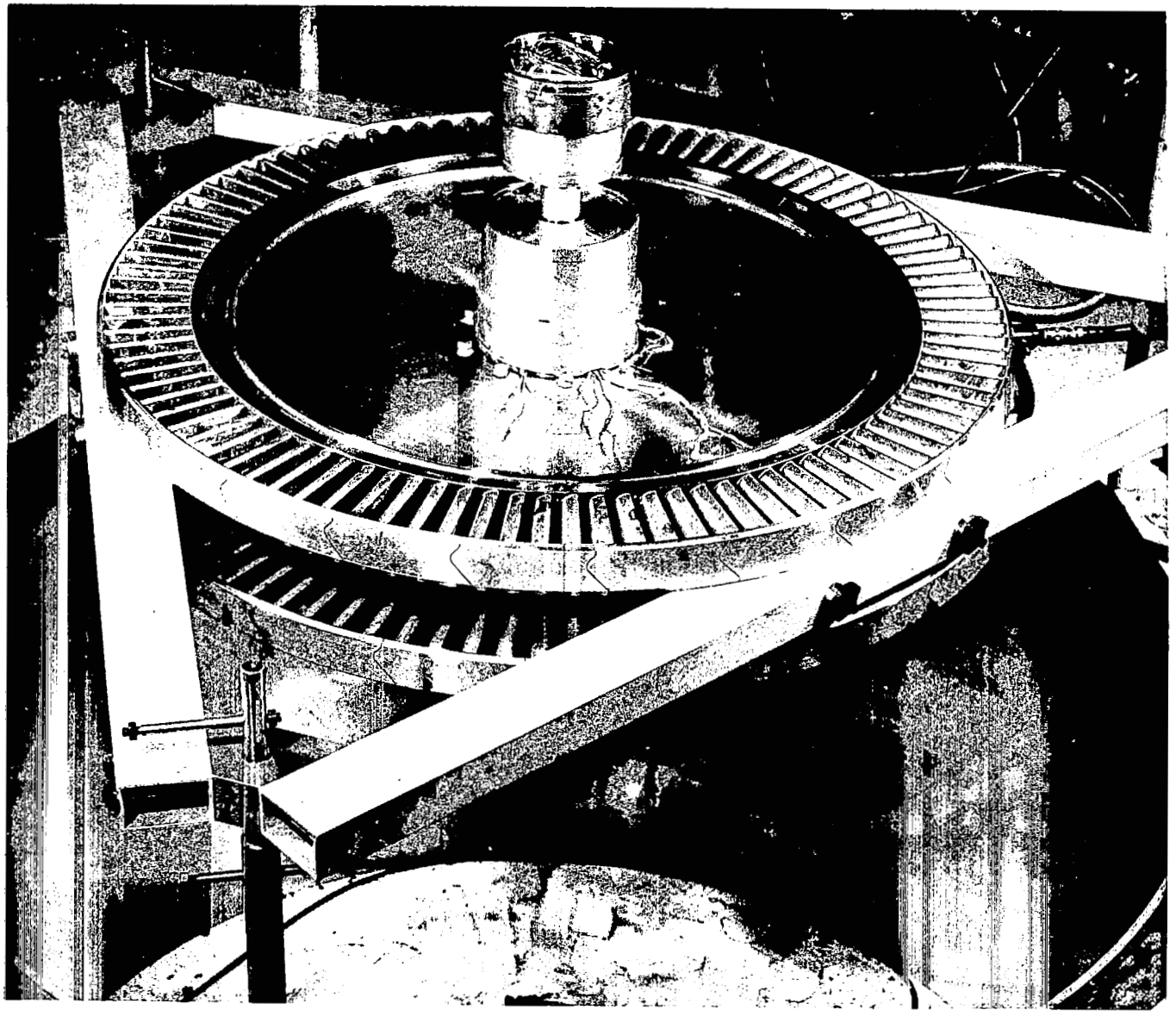

FIG. 9 TEST ROTOR SUPPORTED IN HANDLING RIG

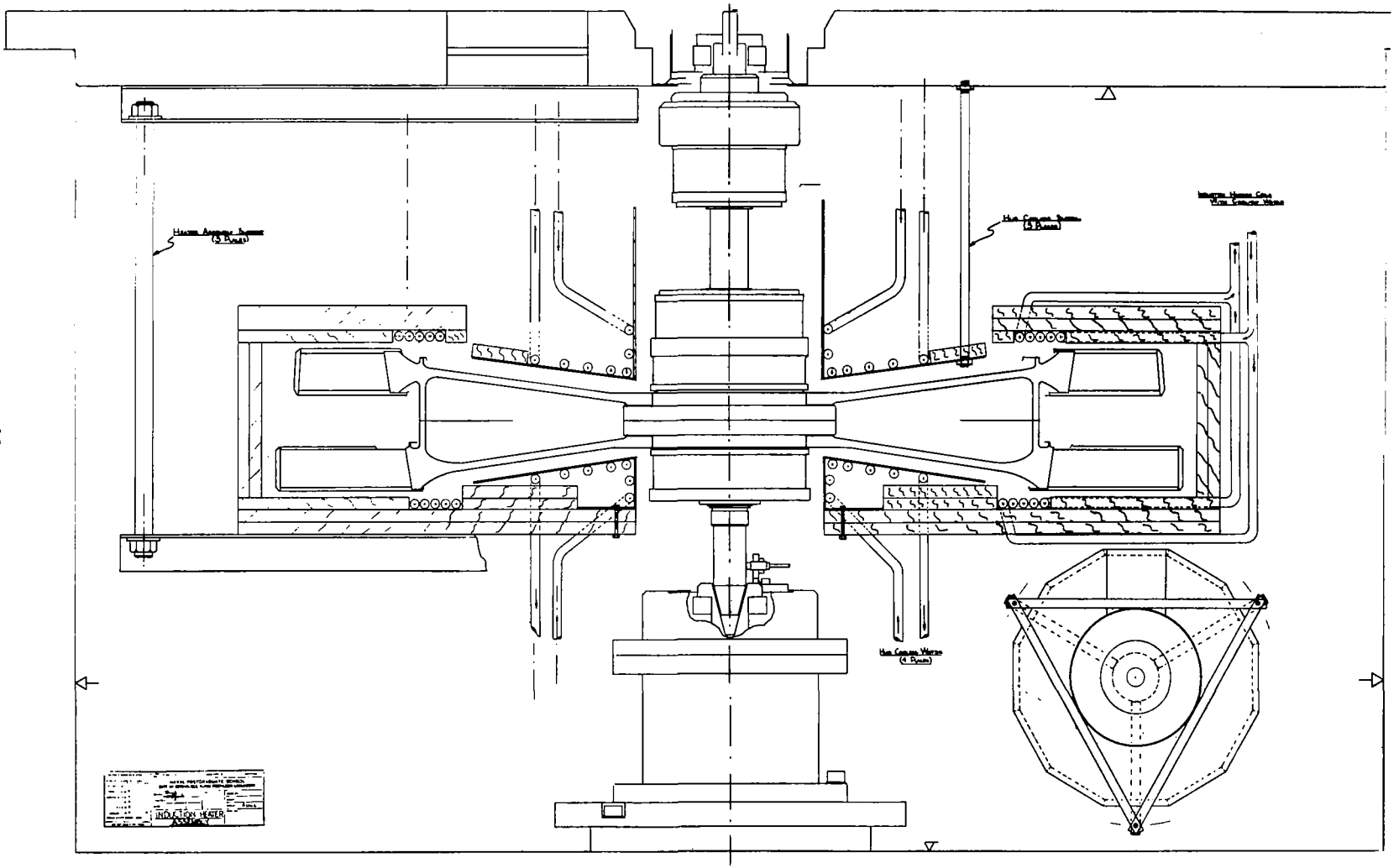

FIG. 10 CROSS SECTION OF HEATING COILS AND HUB COOLING PLATES

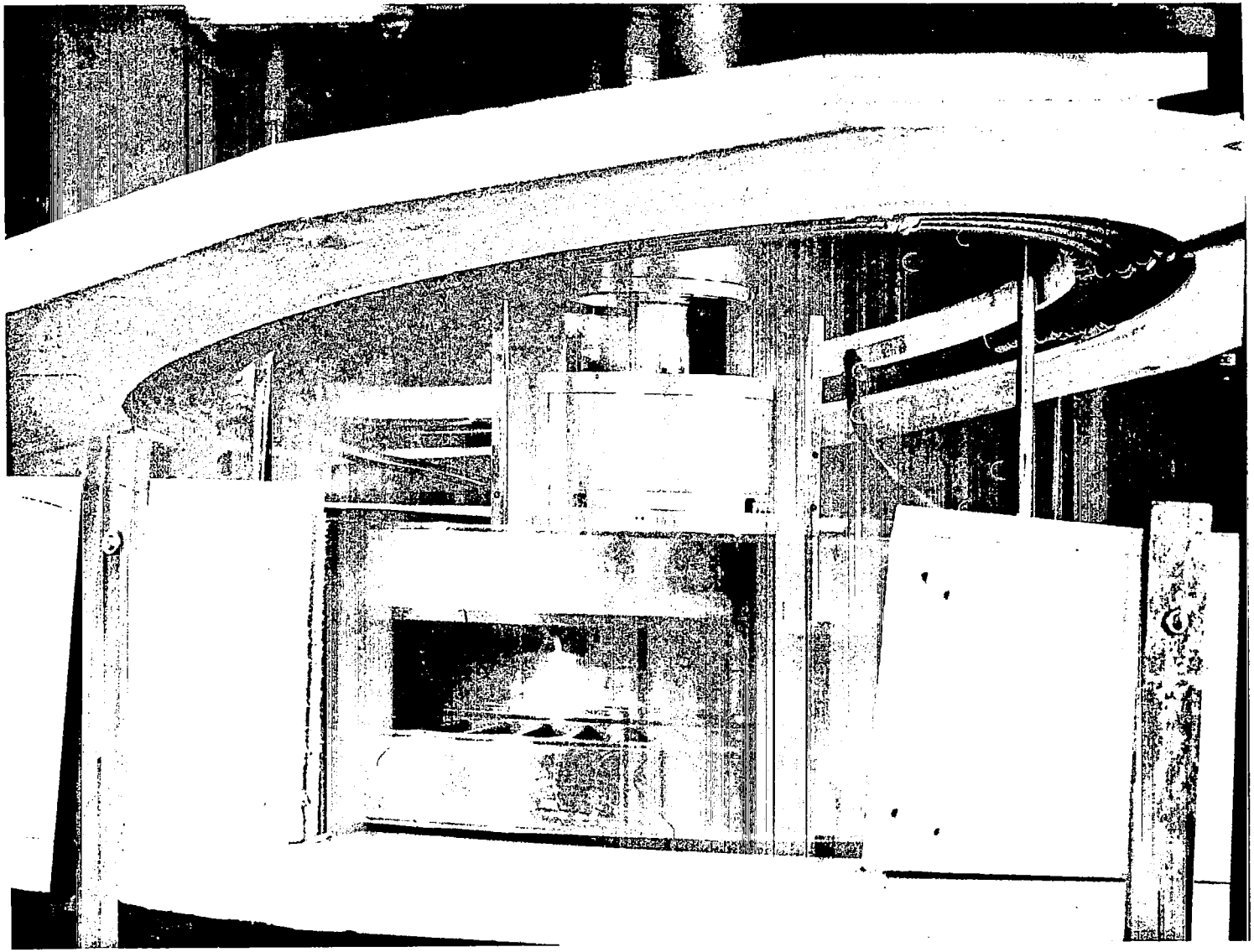

FIG. 11 UPPER HEATING COIL AND INSULATION SURROUNDING TEST ROTOR

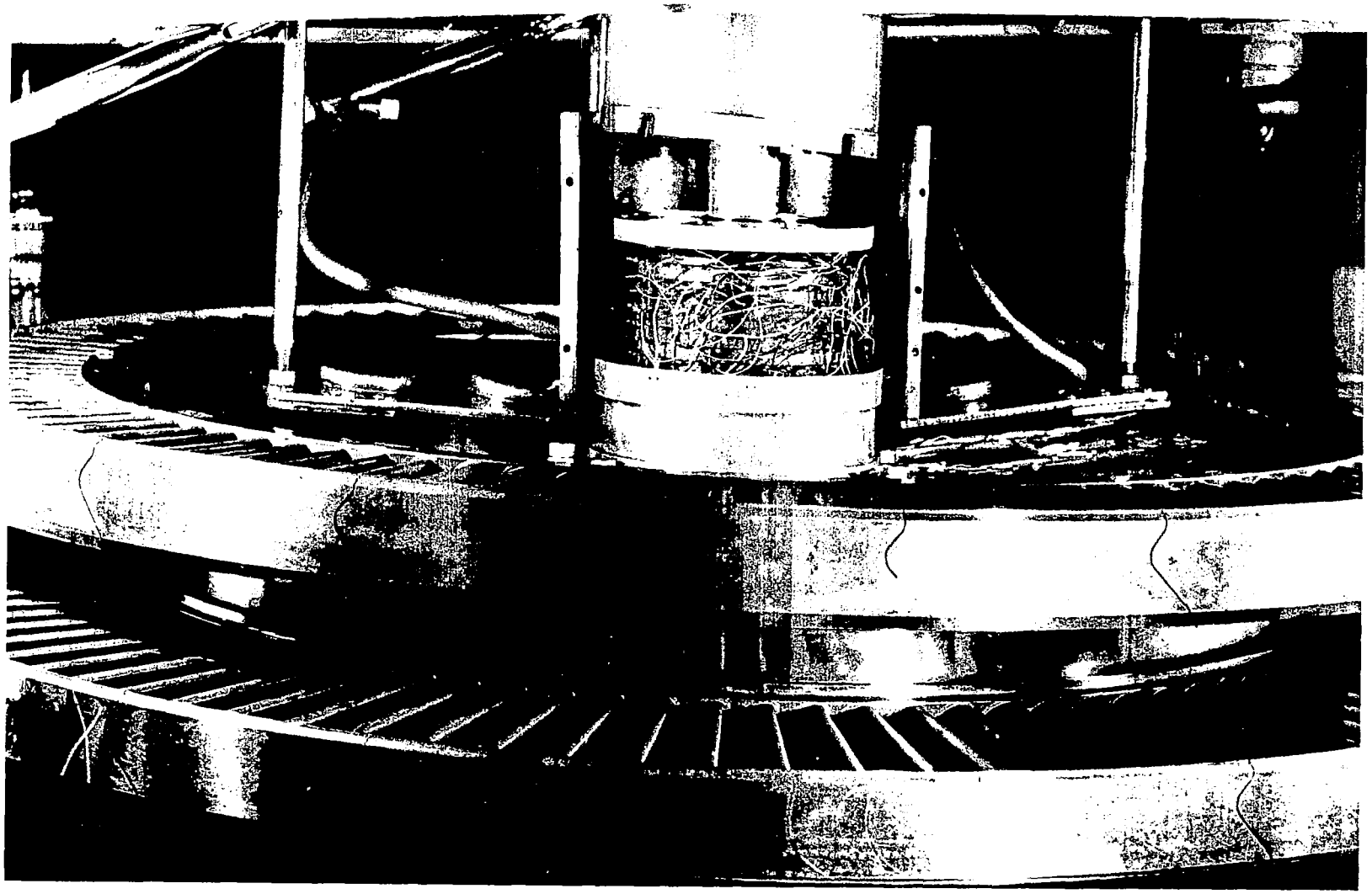

FIG. 12 UPPER HUB COOLING PLATE. (One-half of the cooling plate and the instrumentation cover are removed to show the hub terminal connector.)

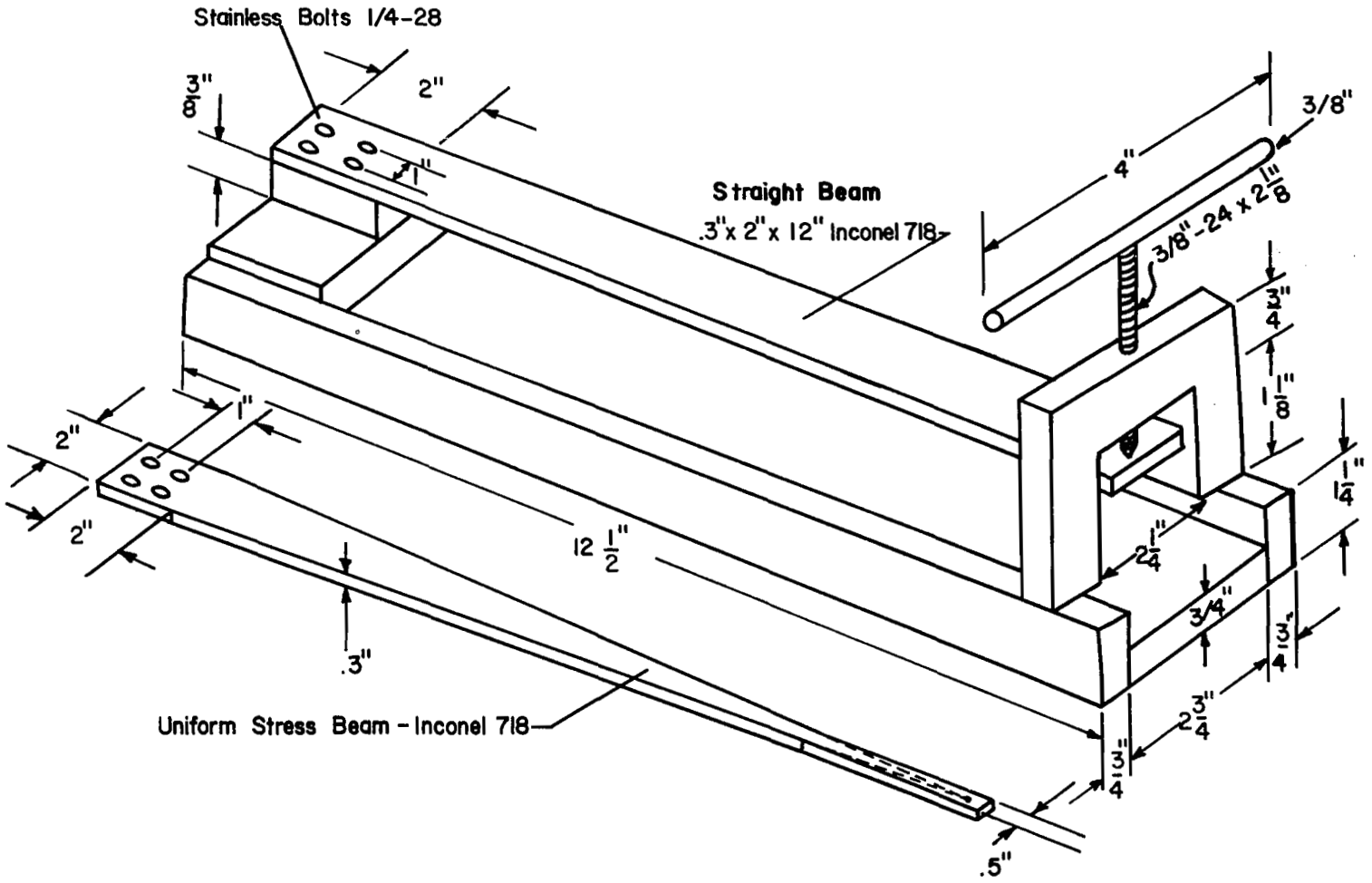


FIG. 13 CANTILEVER BEAM TEST JIG AND UNIFORM STRESS-BEAM

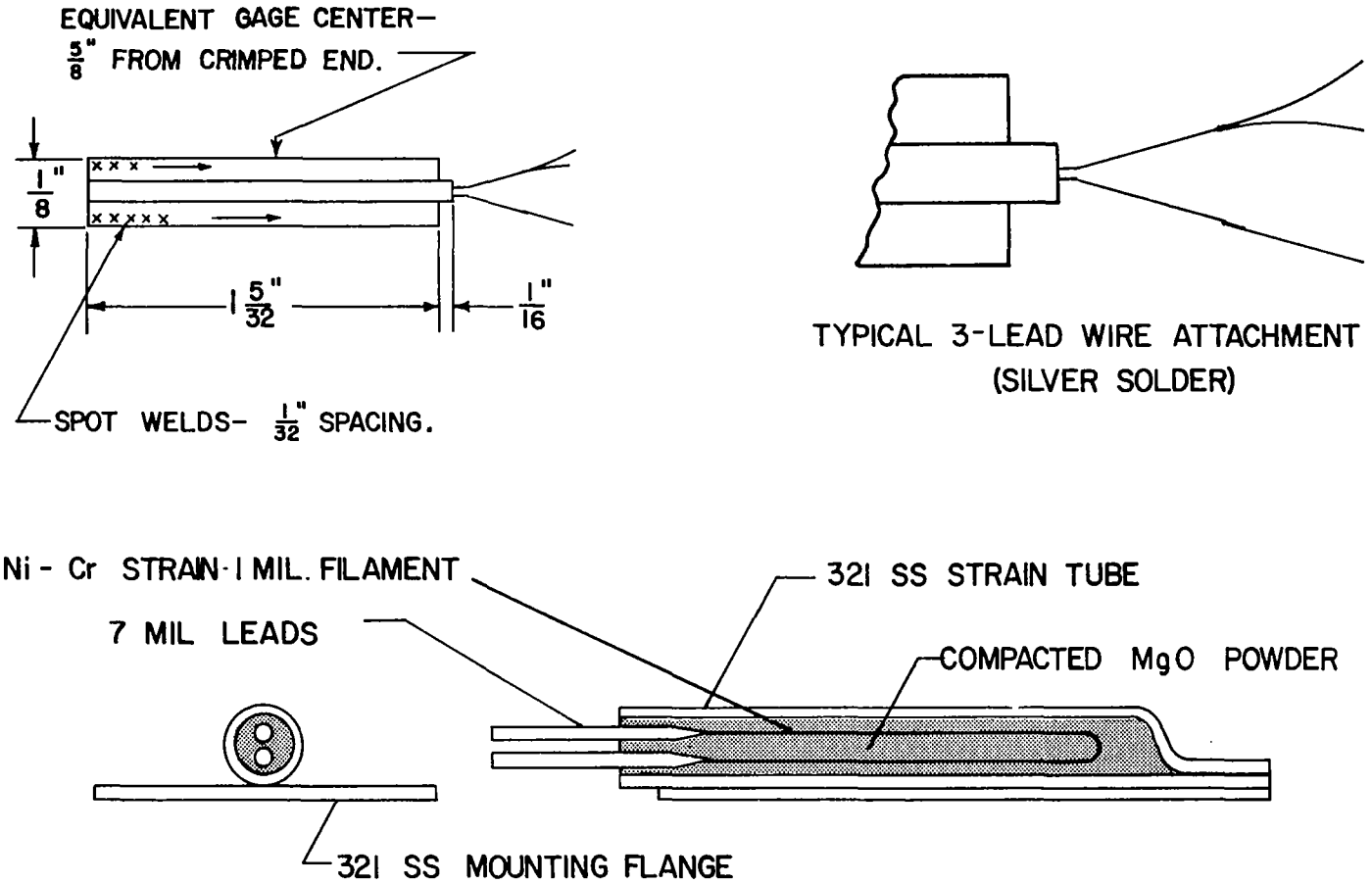


FIG. 14 MICRODOT SG-180 GAGE CONFIGURATION

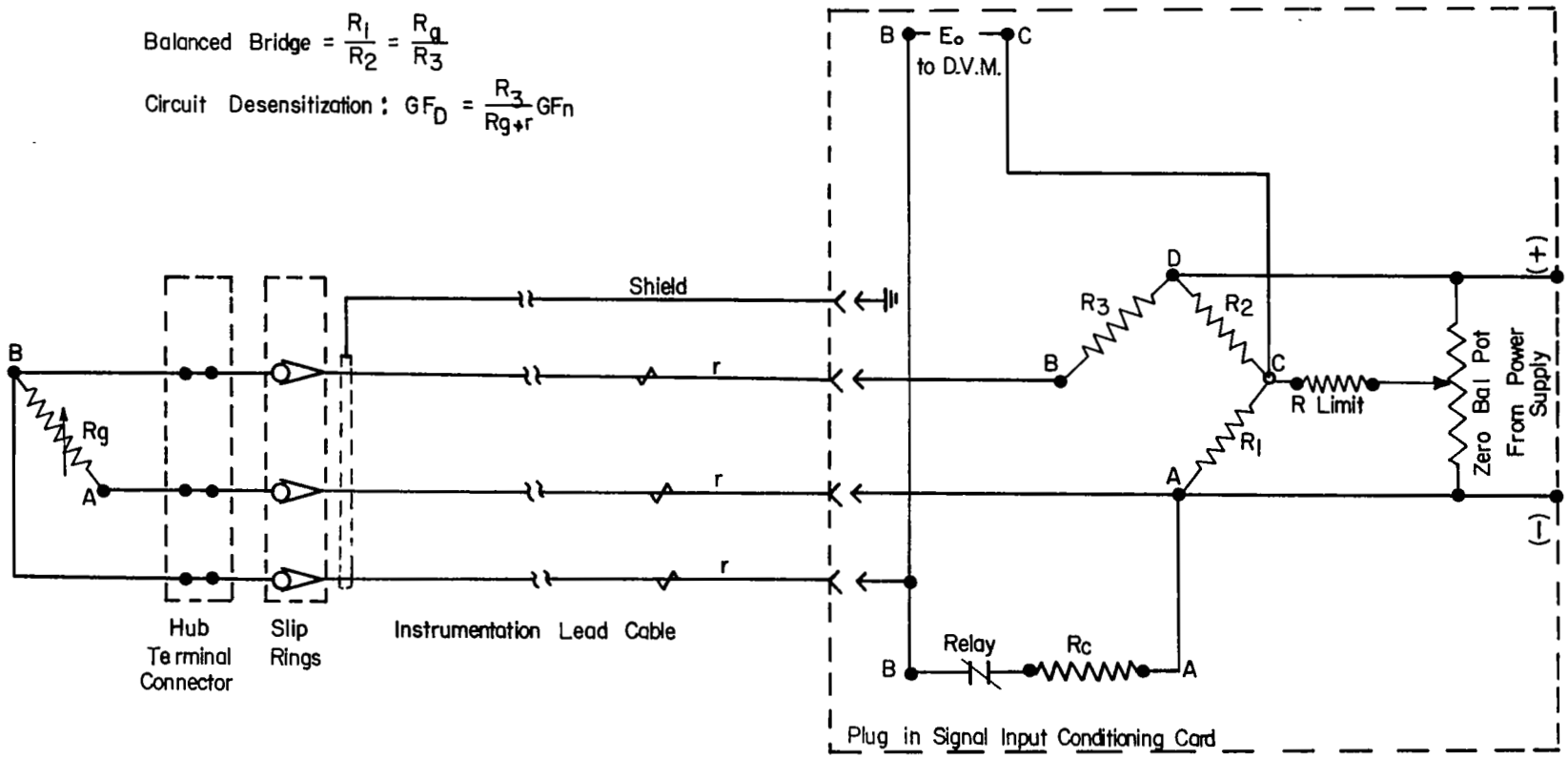


FIG. 15 STANDARD THREE-WIRE CIRCUIT ILLUSTRATING LEAD-WIRE RESISTANCE AND INPUT CONDITIONING

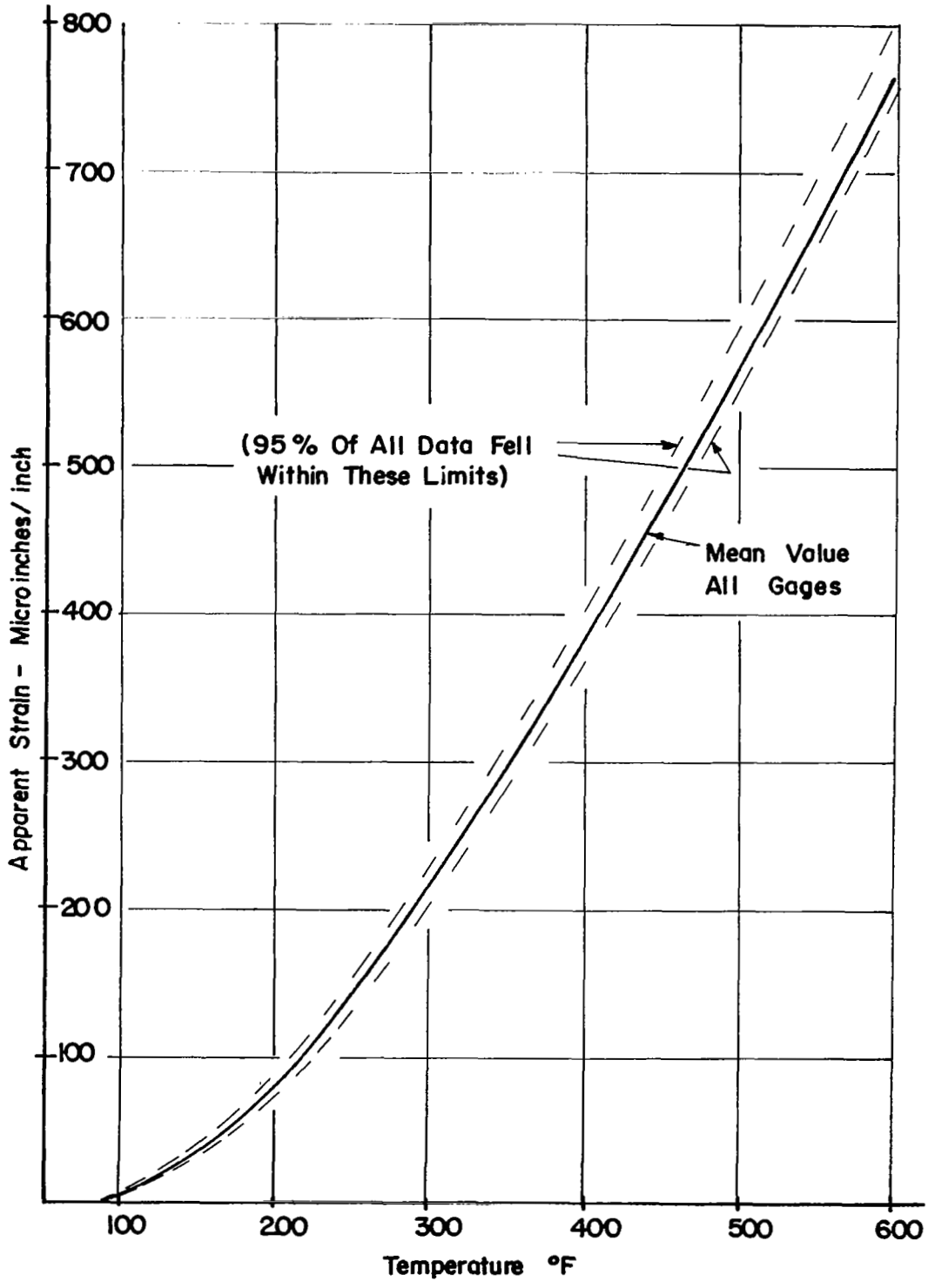


FIG. 16 MEAN APPARENT STRAIN WITH TEMPERATURE CURVE BASED ON TESTS OF EIGHT GAGES MOUNTED ON CALIBRATION BEAM

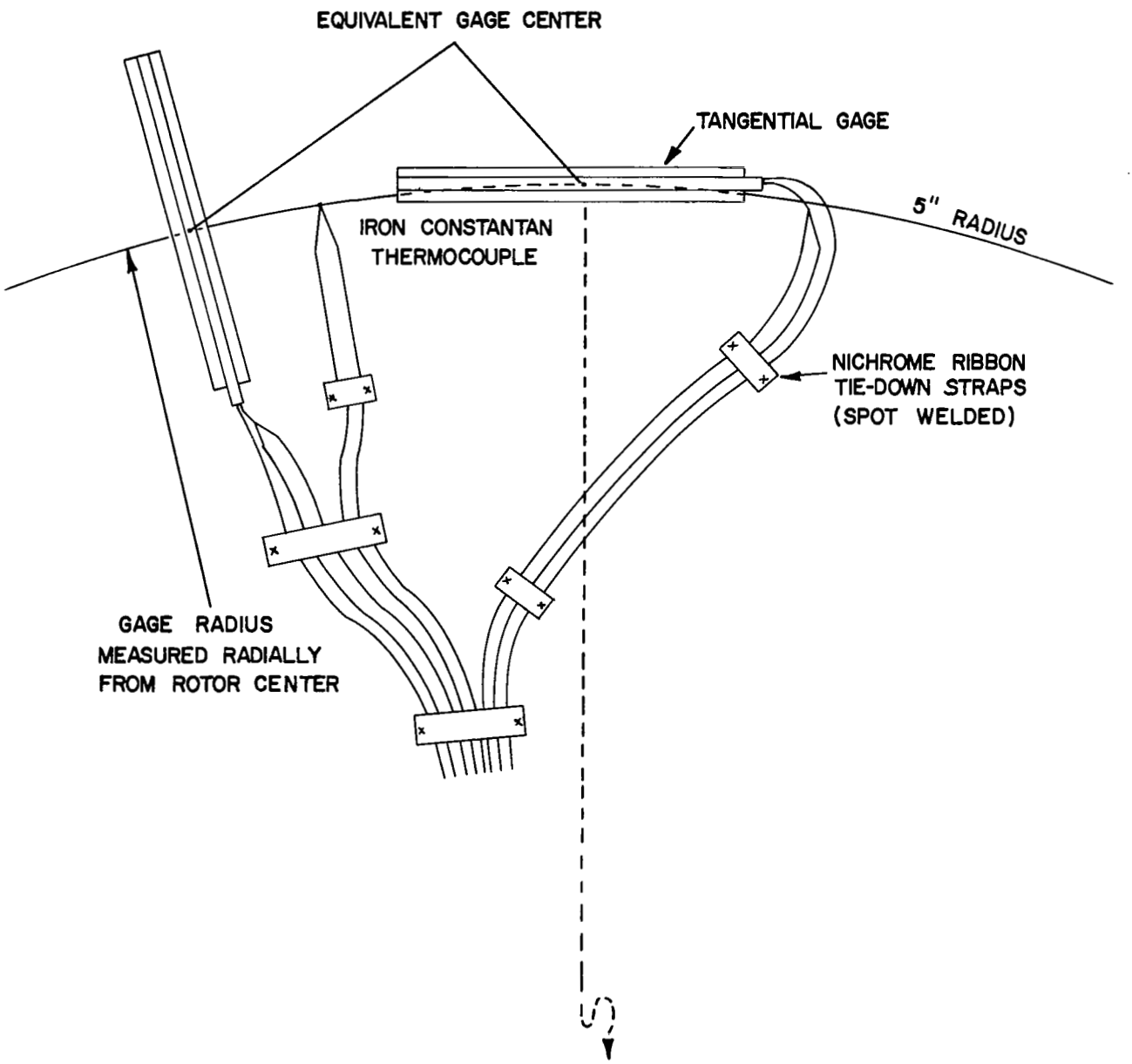


FIG. 17 TYPICAL GAGE INSTALLATION (MICRODOT SG-180) ON ROTOR DISK

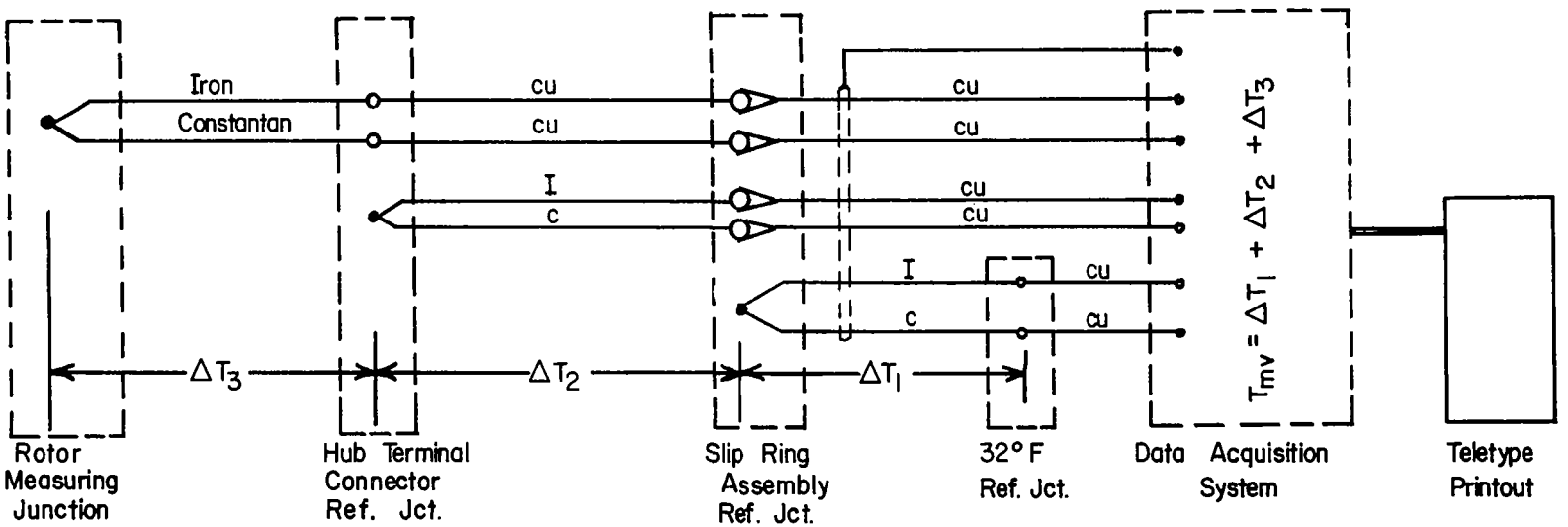


FIG. 18 THERMOCOUPLE CIRCUIT SHOWING REFERENCE JUNCTION ARRANGEMENT

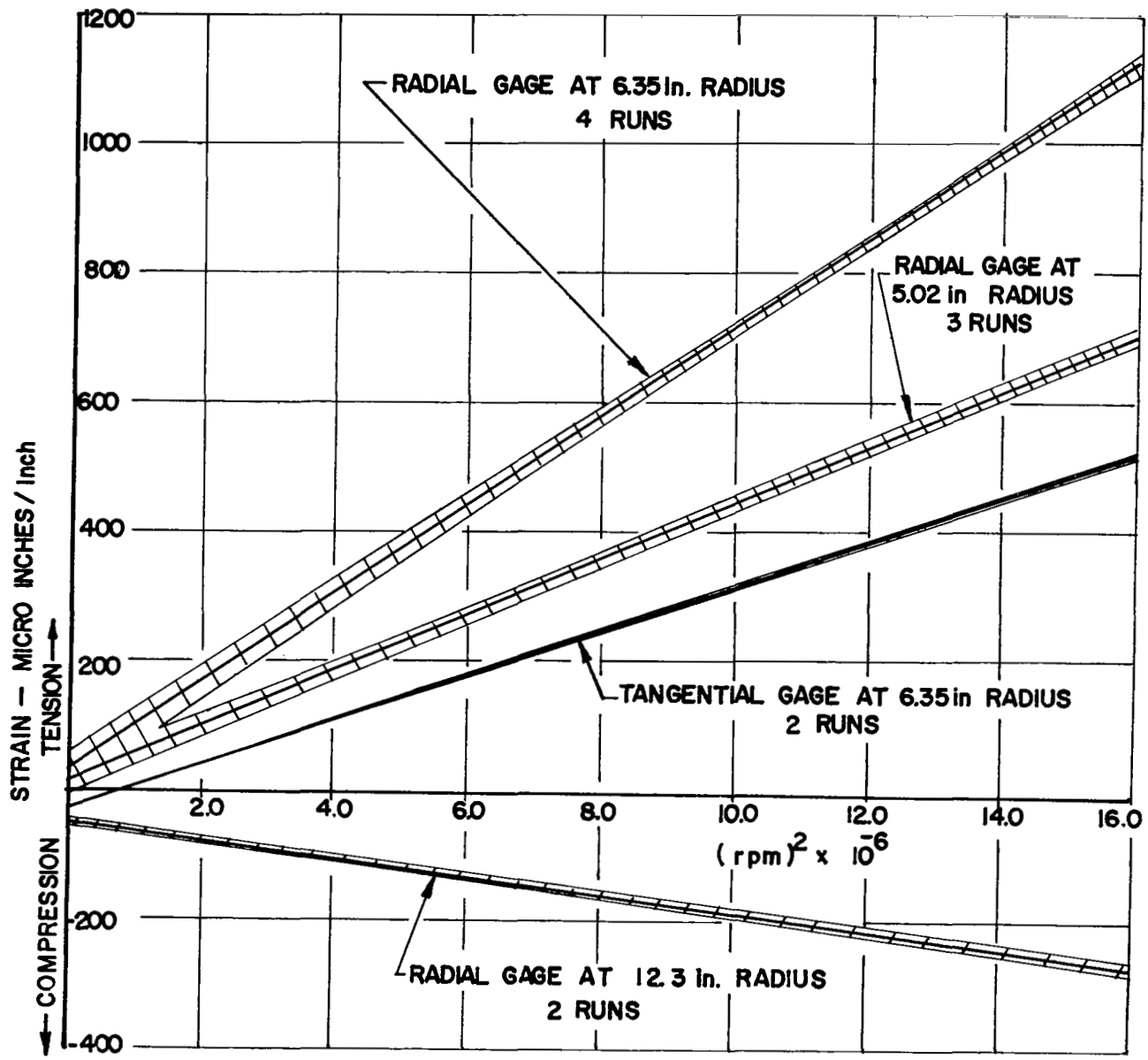


FIG. 19 STRAIN DATA SCATTER BANDS FOR TYPICAL FACE - 1 GAGES - (Heavy lines denote average of all runs)

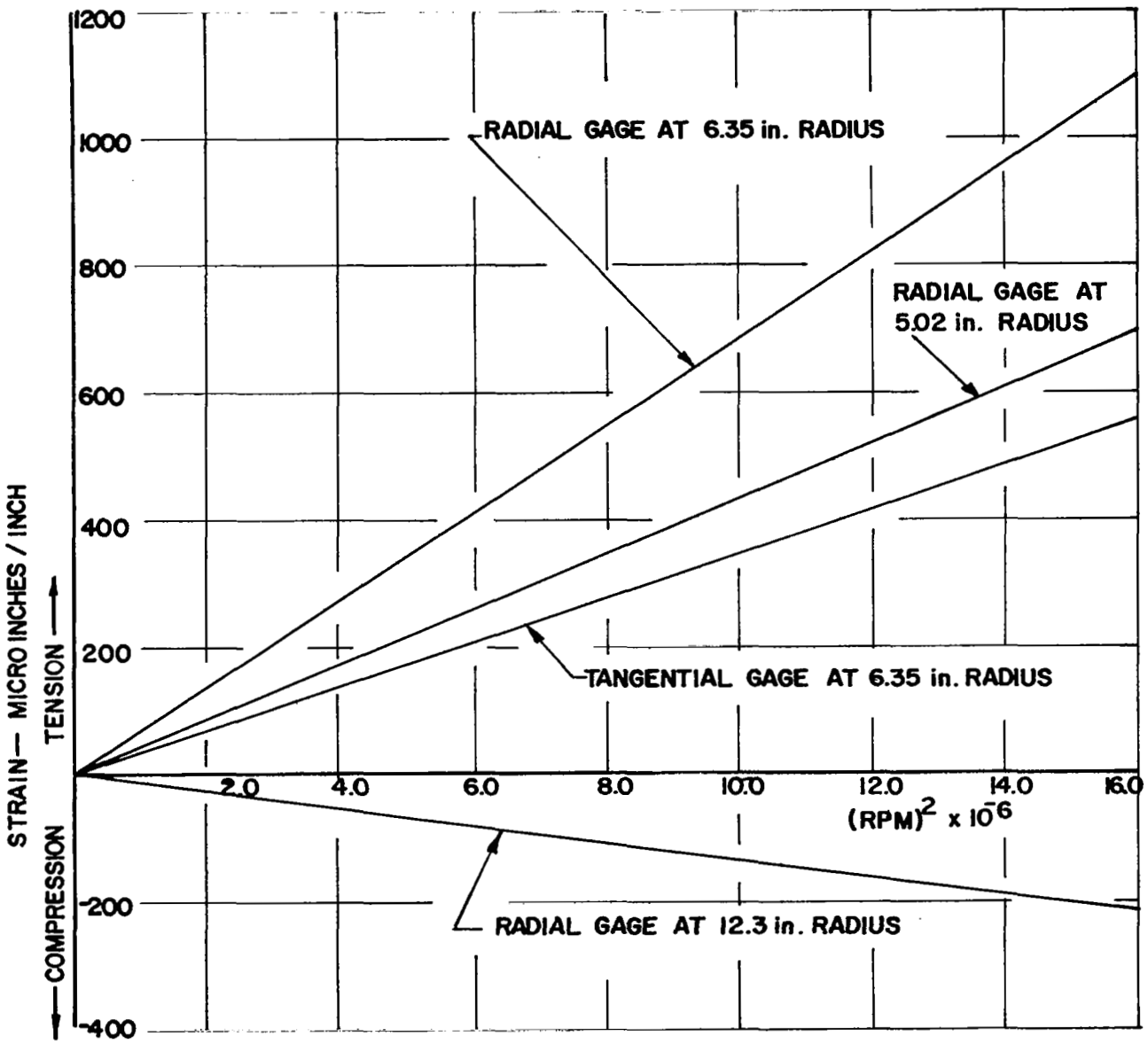


FIG. 20 AVERAGED AND ZEROED STRAIN DATA FOR TYPICAL FACE 1-GAGES

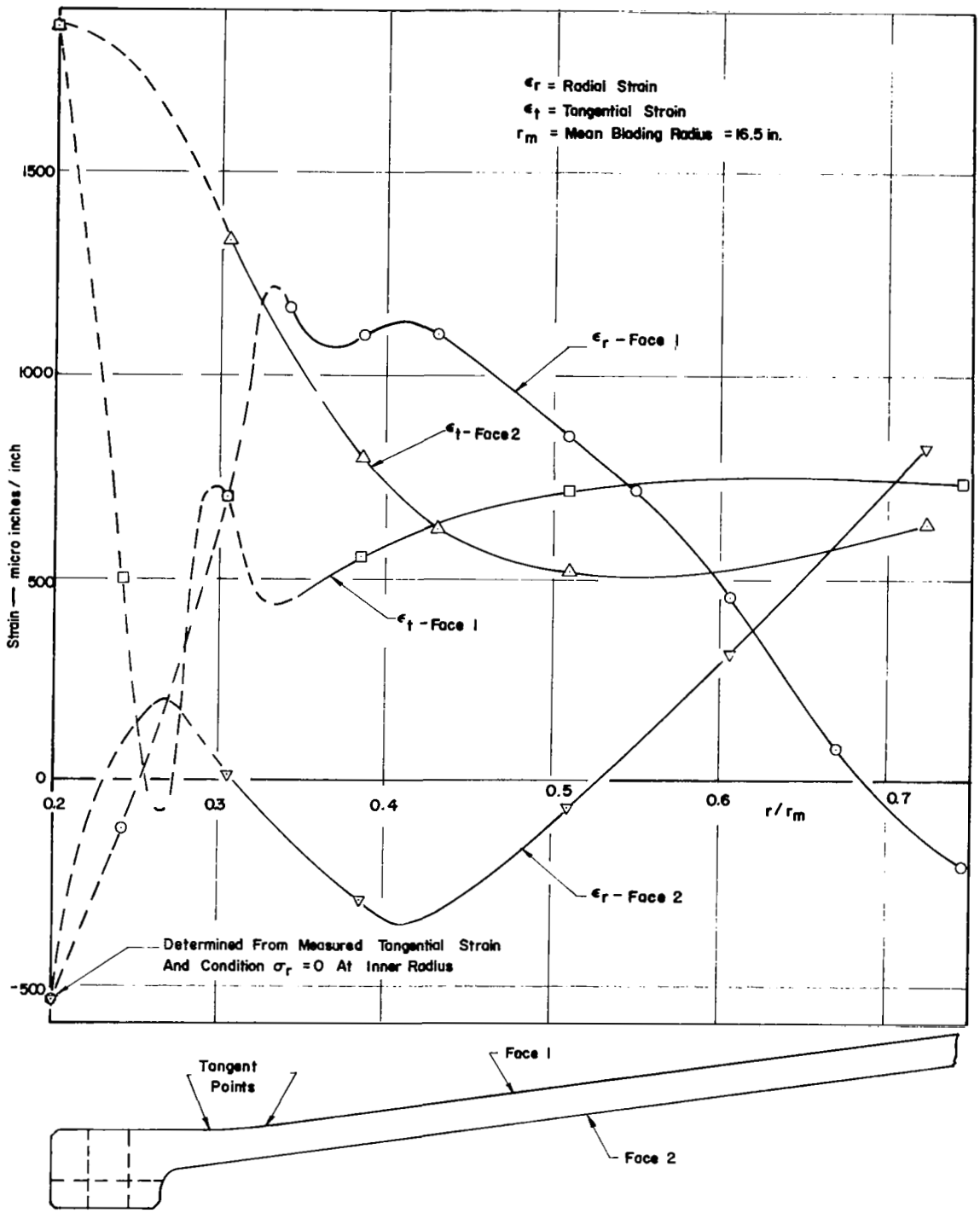


FIG. 21 CENTRIFUGAL STRAINS ON FIRST-STAGE DISK AT 4,000 RPM (Broken lines in hub region represent approximate strain distributions estimated from a limited number of data points.)

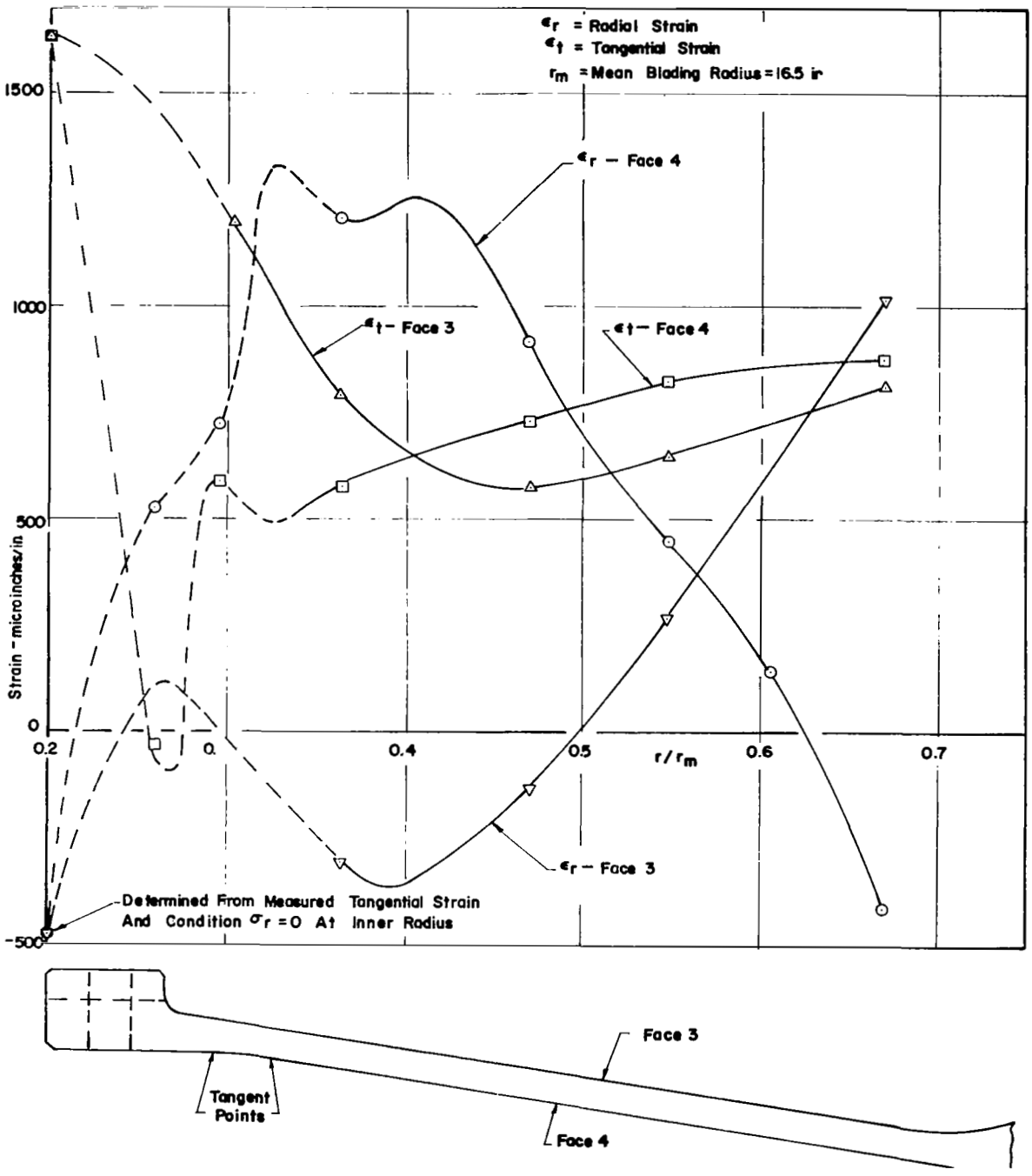


FIG. 22 CENTRIFUGAL STRAINS ON SECOND-STAGE DISK AT 4,000 RPM
(Broken lines in hub region represent approximate strain distributions estimated from a limited number of data points.)

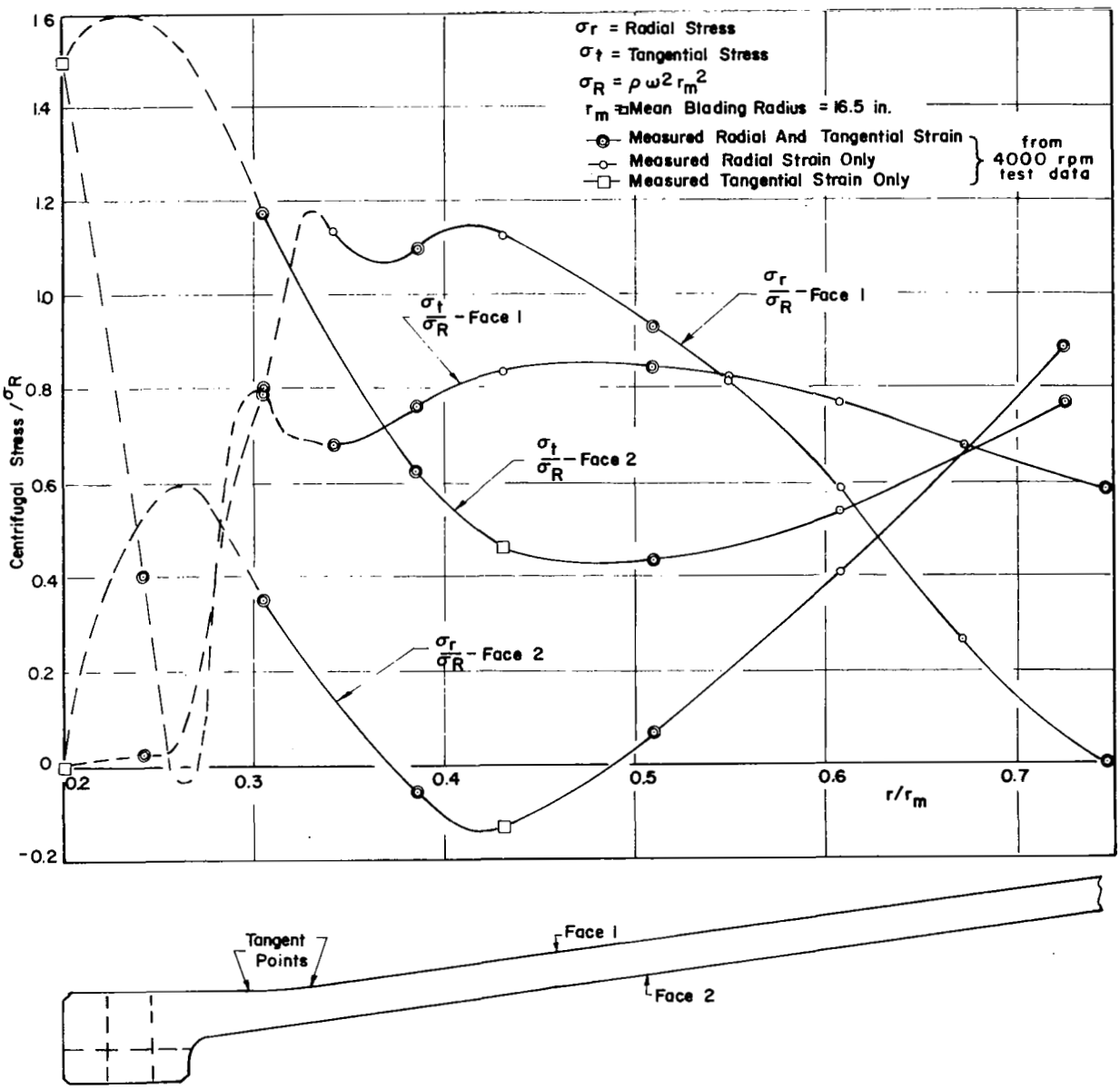


FIG. 23 DIMENSIONLESS CENTRIFUGAL STRESSES ON FIRST-STAGE DISK (Stress distributions based on estimated strains are shown by broken lines.)

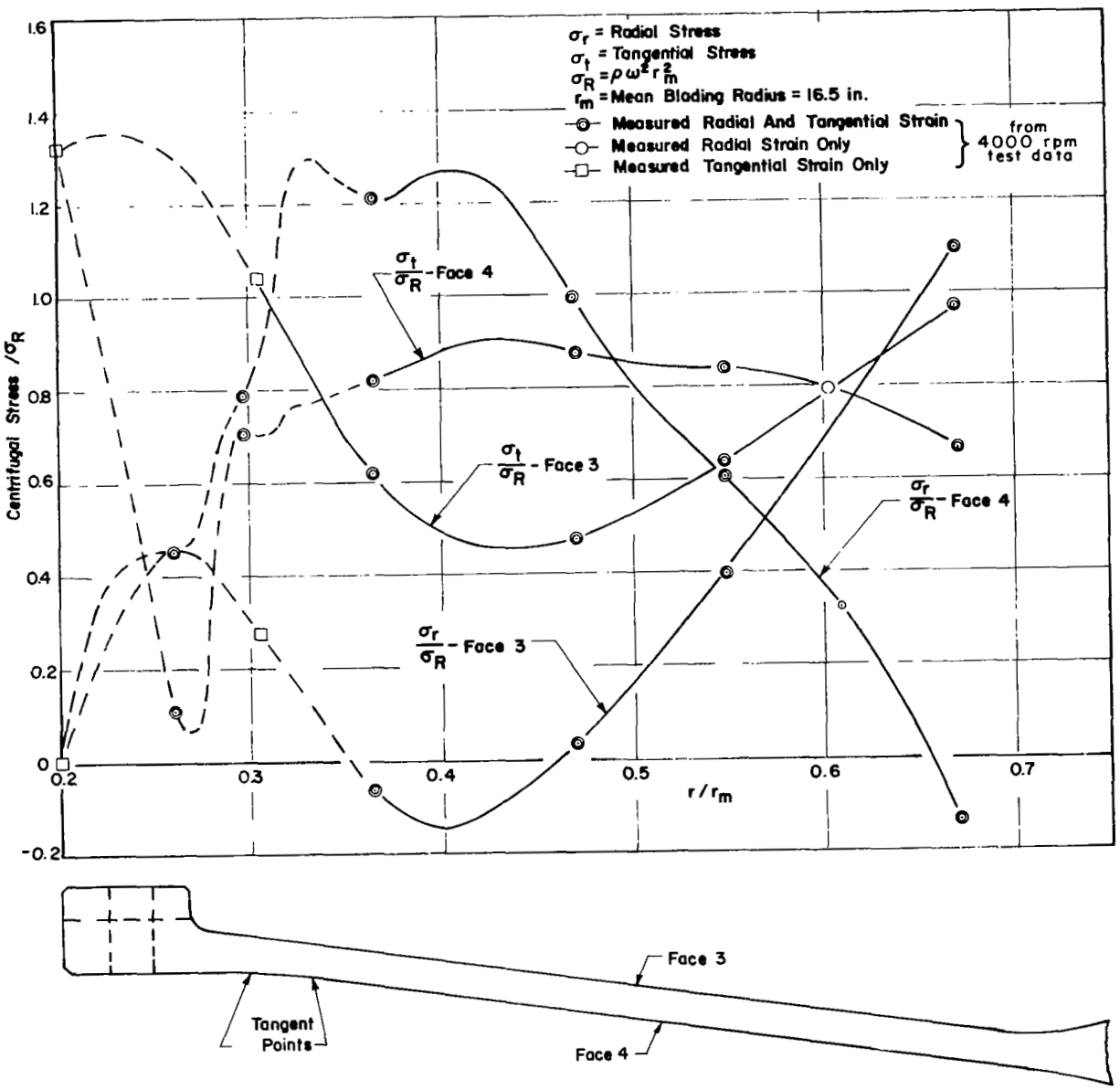


FIG. 24 DIMENSIONLESS CENTRIFUGAL STRESSES ON SECOND-STAGE DISK (Stress distributions based on estimated strains are shown by broken lines.)

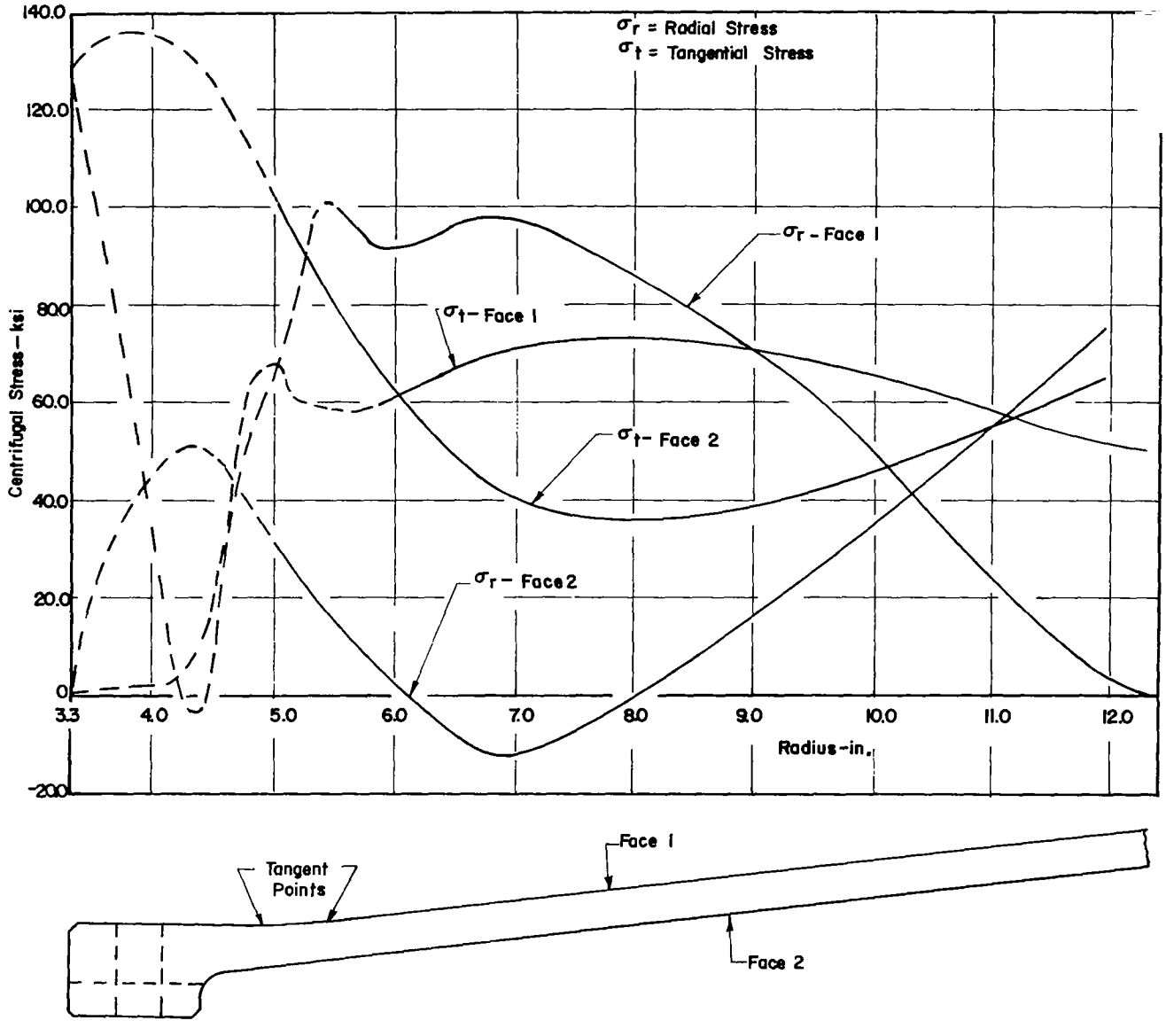


FIG. 25 CENTRIFUGAL STRESSES ON FIRST-STAGE DISK AT 6,100 RPM (Stress distributions based on estimated strains are shown by broken lines.)

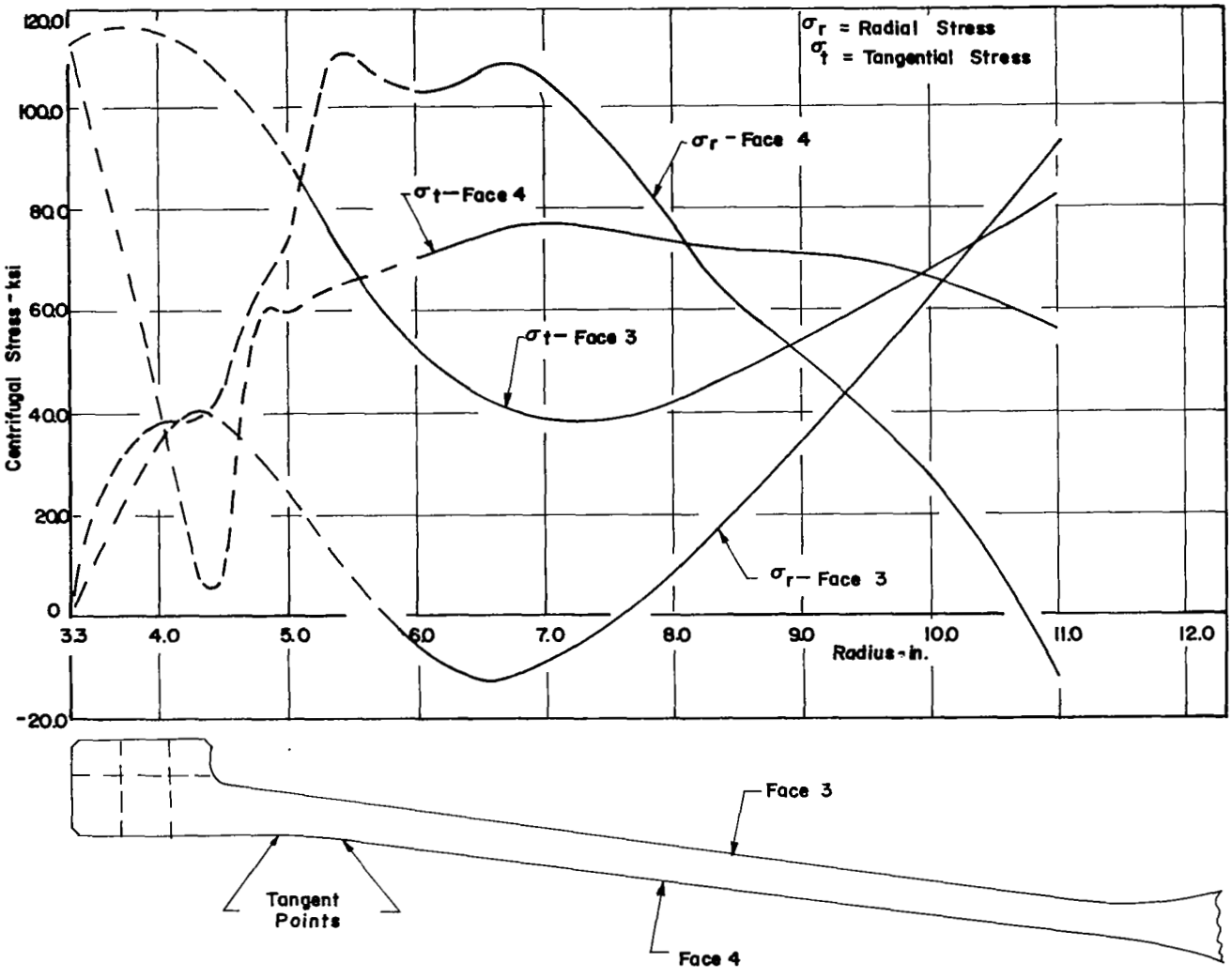





FIG. 26 CENTRIFUGAL STRESSES ON SECOND-STAGE DISK AT 6,100 RPM (Stress distributions based on estimated strains are shown by broken lines.)

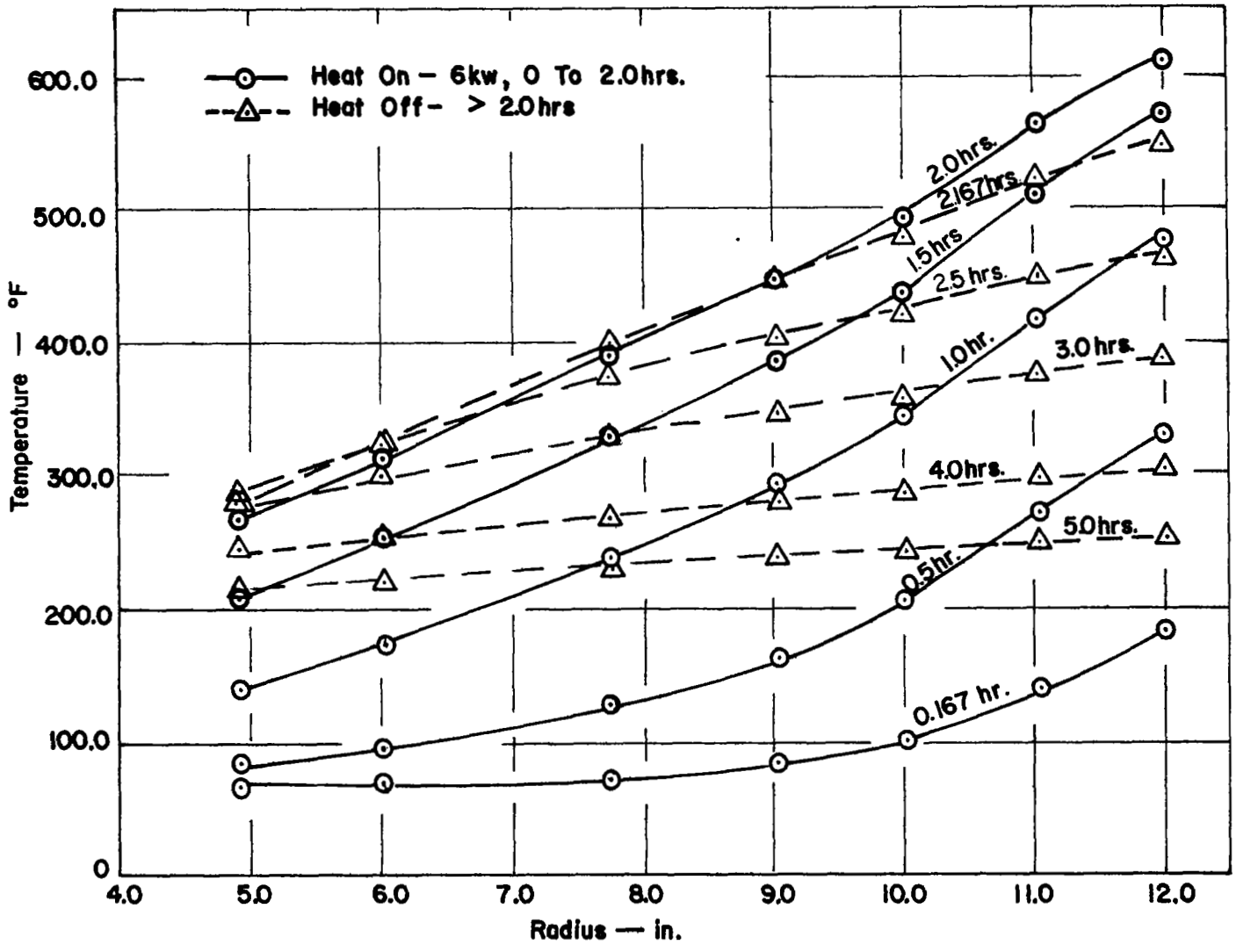


FIG. 27 TEMPERATURE DISTRIBUTIONS ON OUTER FACE OF SECOND STAGE DISK AT VARIOUS TIMES DURING A STANDARD RUN

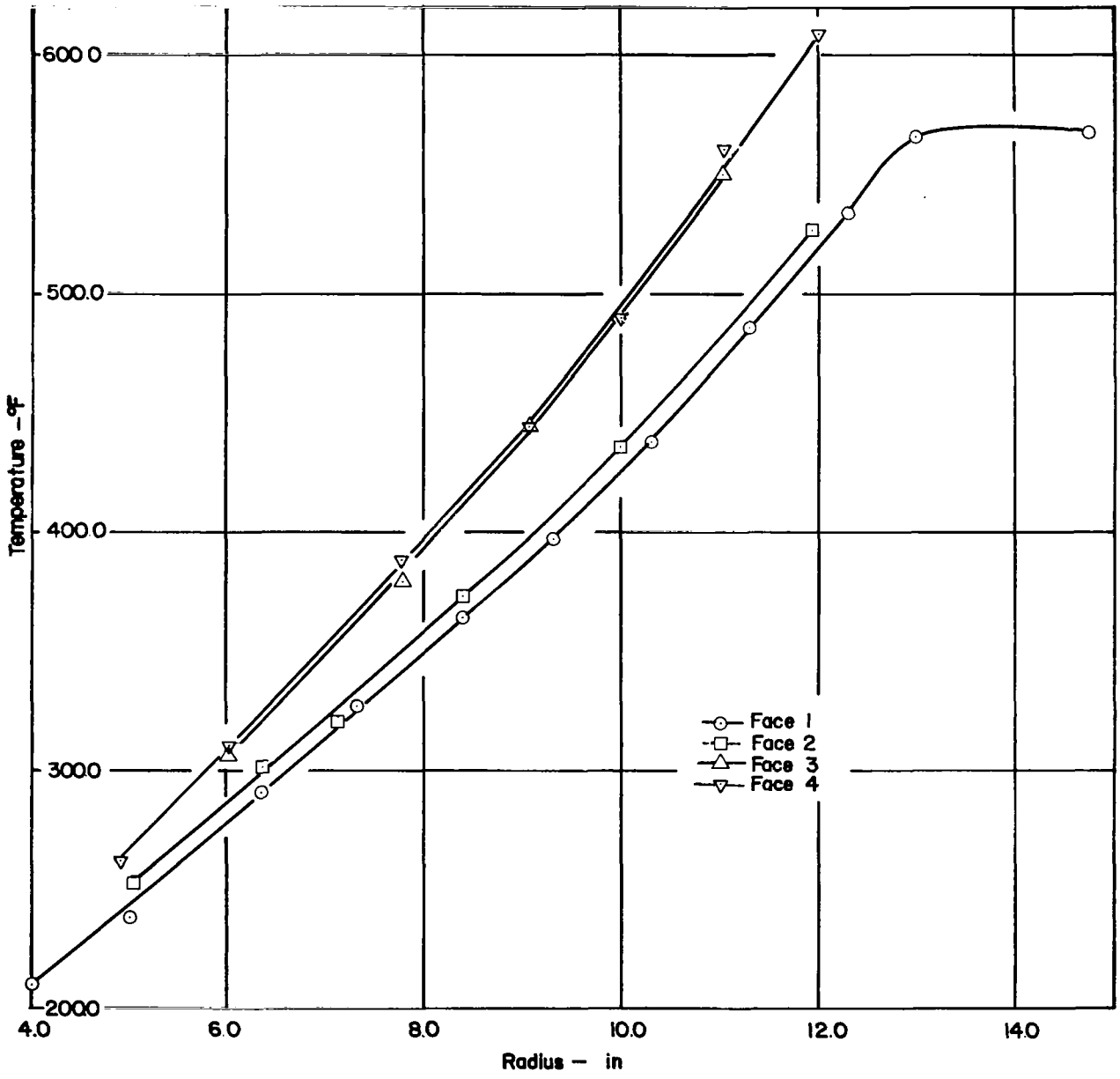


FIG. 28 TEMPERATURE GRADIENTS AFTER 2.0 HOURS AT 6 KW

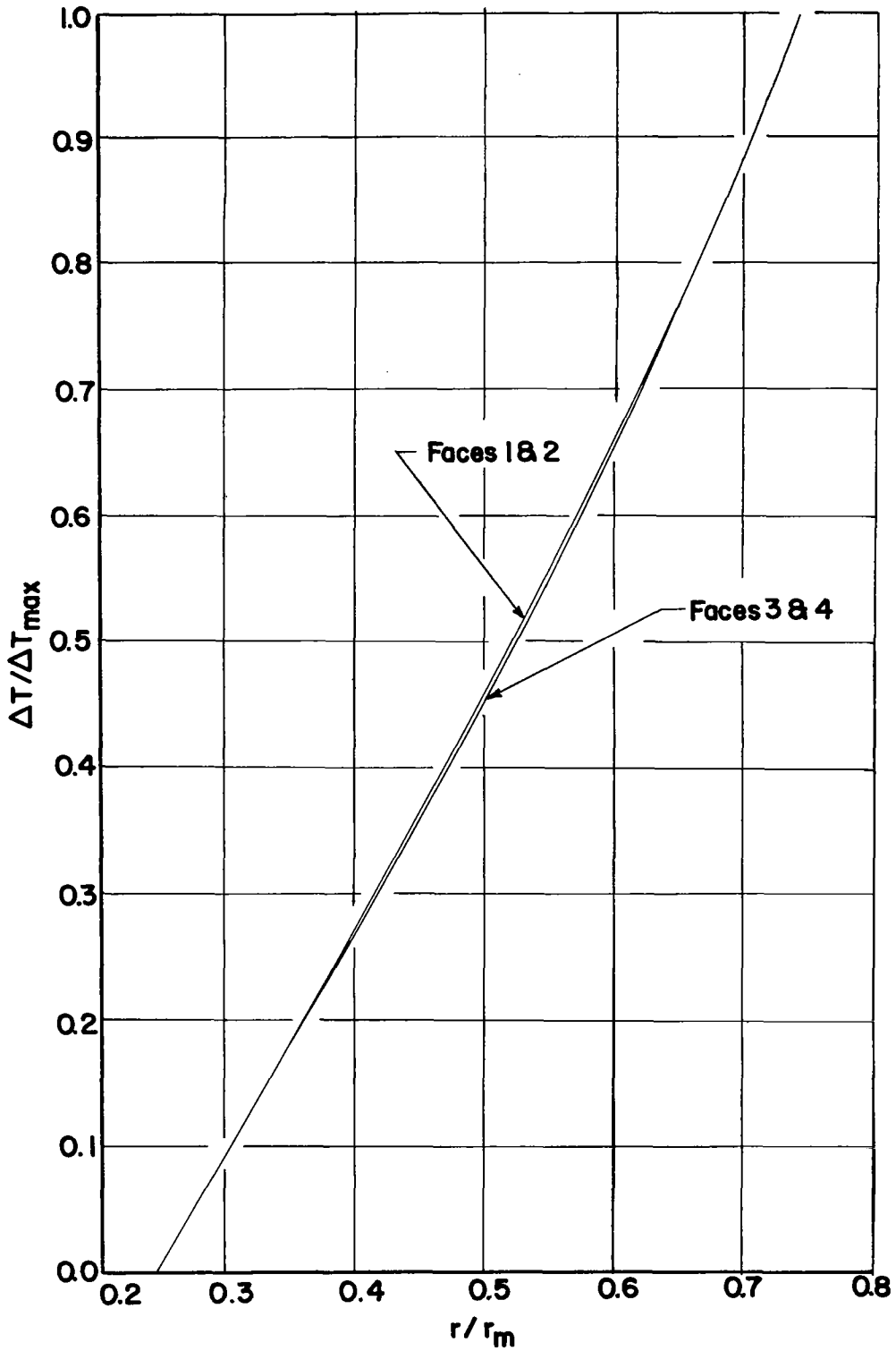


FIG. 29 DIMENSIONLESS TEMPERATURE DISTRIBUTIONS FOR 2.0 HOURS AT 6 KW

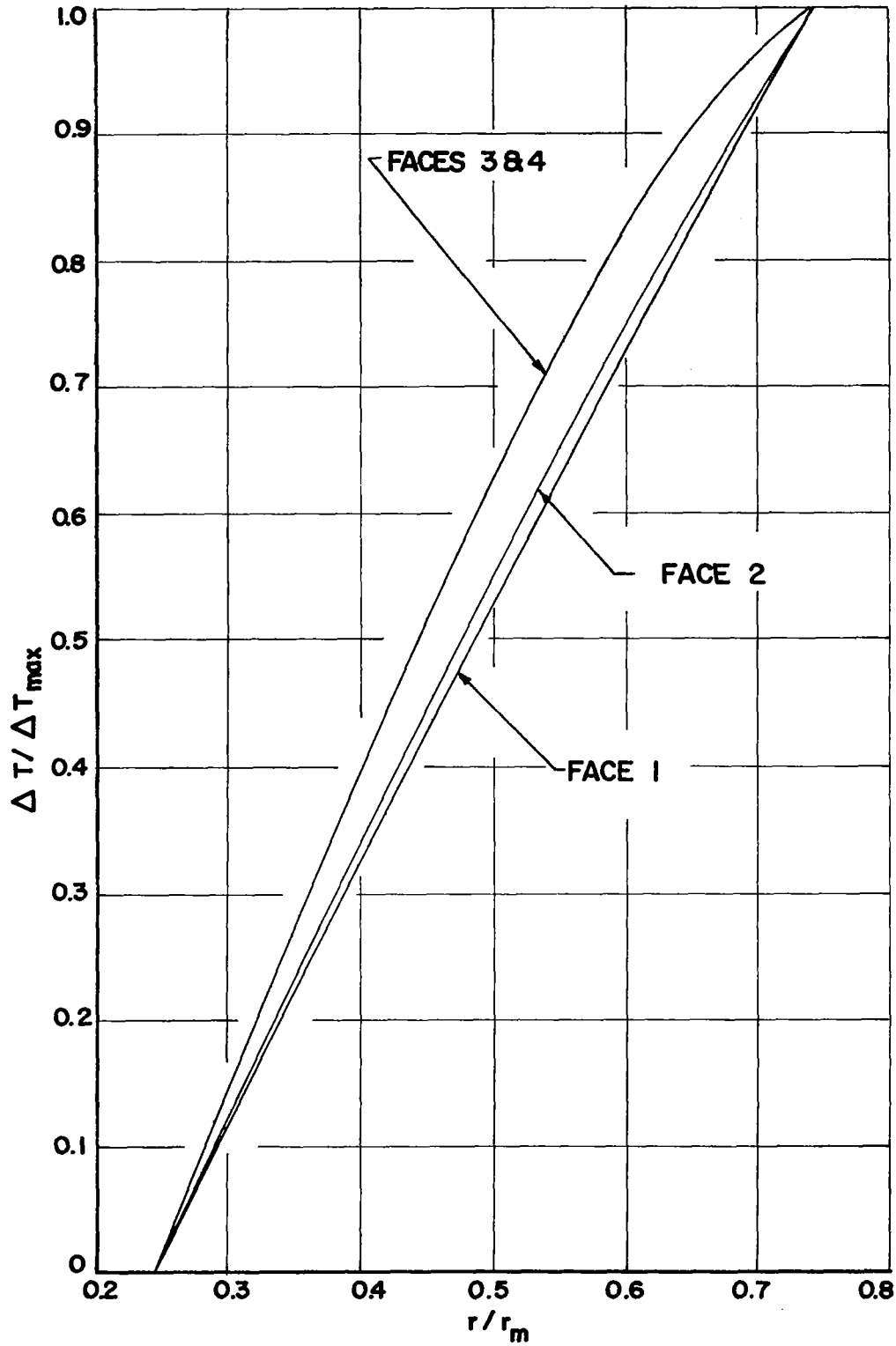


FIG. 30 DIMENSIONLESS TEMPERATURE DISTRIBUTIONS FOR 2.0 HOURS AT 6 KW PLUS 1.0 HOUR AT 0 KW

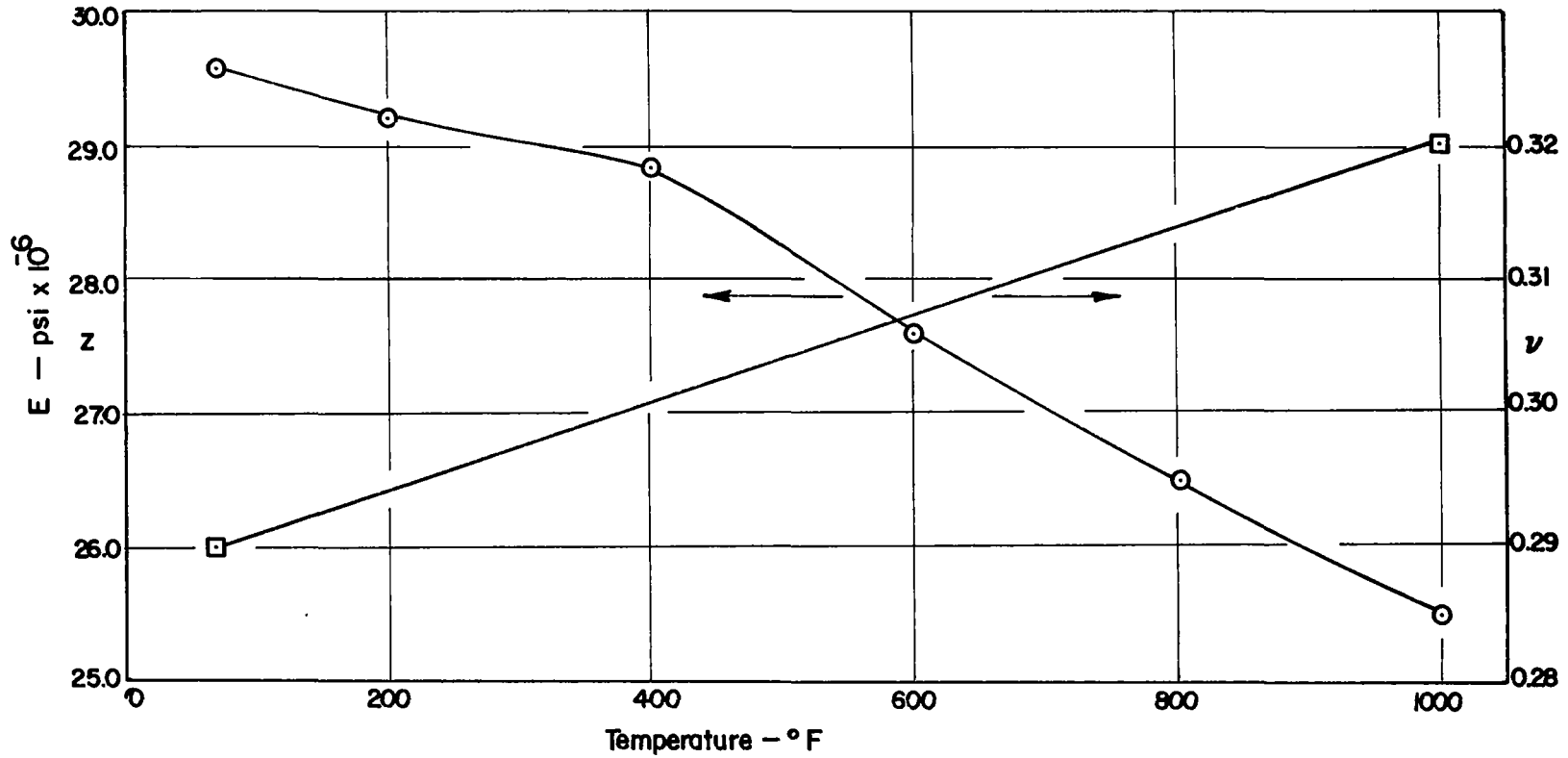


FIG. 31 VARIATION OF YOUNG'S MODULUS AND POISSON'S RATIO WITH TEMPERATURE
(From table 1 of purchase request.)

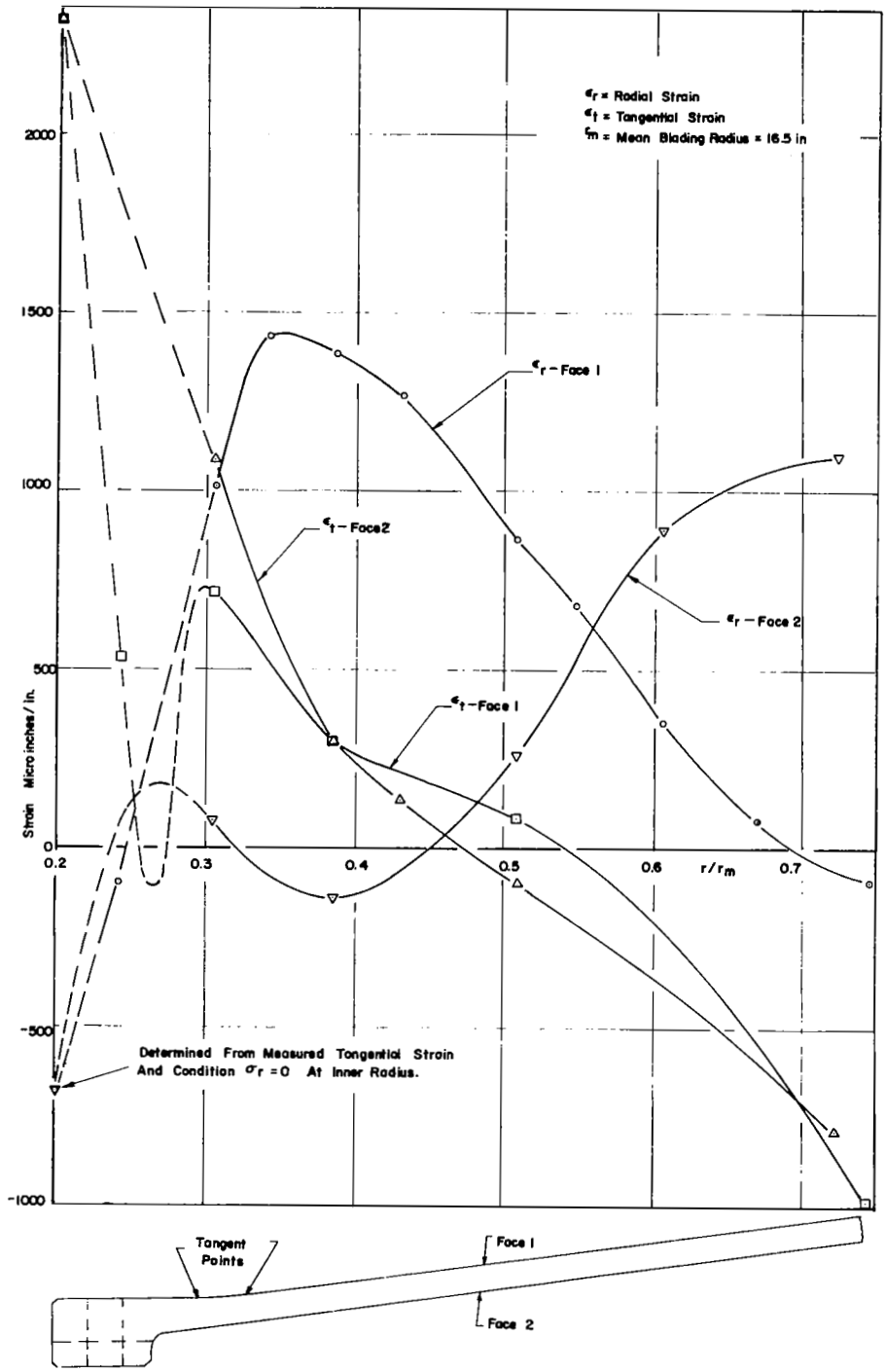


FIG. 32 THERMAL STRAINS ON FIRST-STAGE DISK AFTER 2.0 HOURS AT 6 KW (Broken lines in hub region represent approximate strain distributions estimated from a limited number of data points.)

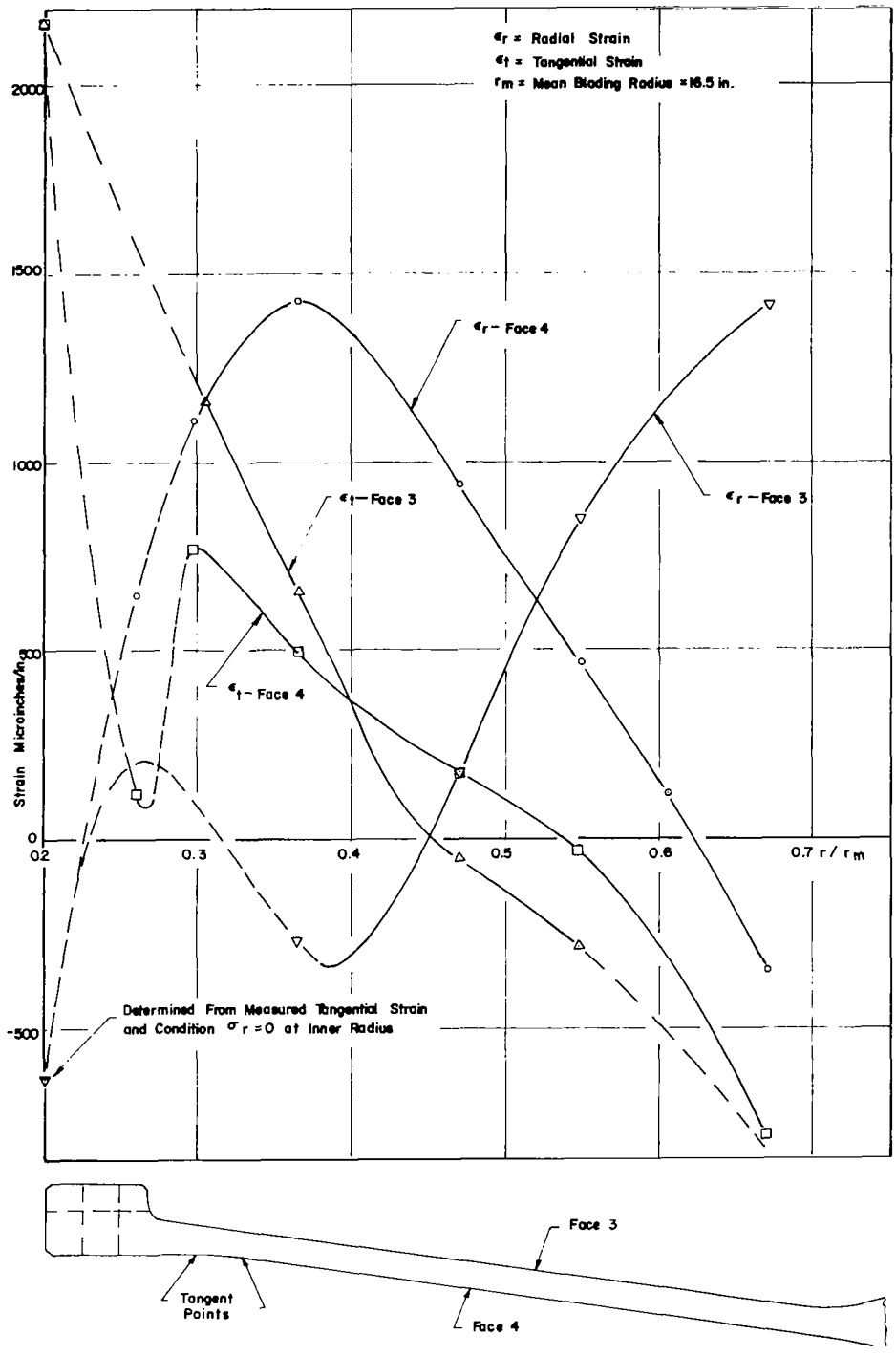


FIG. 33 THERMAL STRAINS ON SECOND-STAGE DISK AFTER 2.0 HOURS AT 6 KW (Broken lines in hub region represent approximate strain distributions estimated from a limited number of data points.)

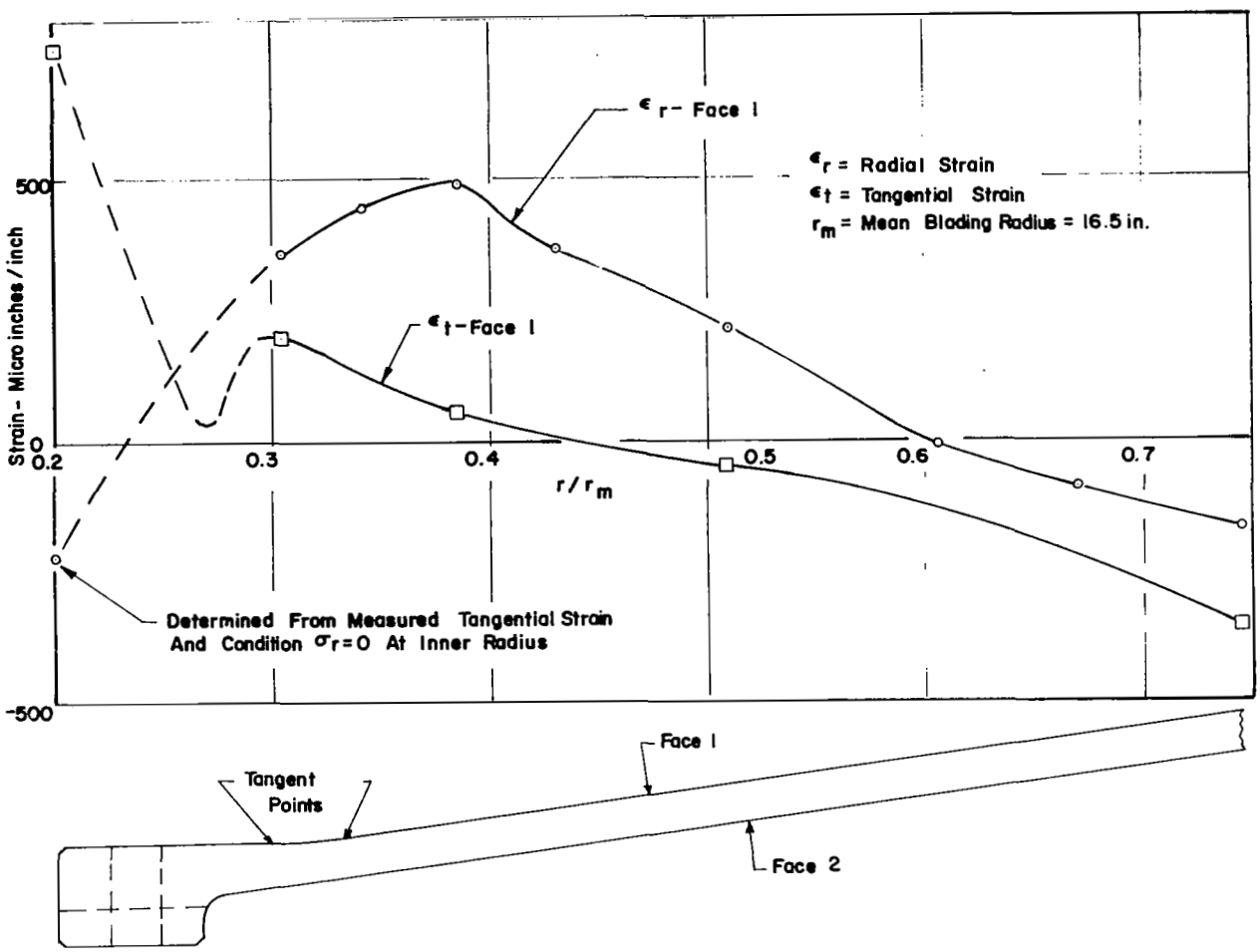


FIG. 34 THERMAL STRAINS ON FIRST-STAGE DISK AFTER 2.0 HOURS AT 6 KW PLUS 1.0 HOUR AT 0 KW (Broken lines in hub region represent approximate strain distributions estimated from a limited number of data points.)

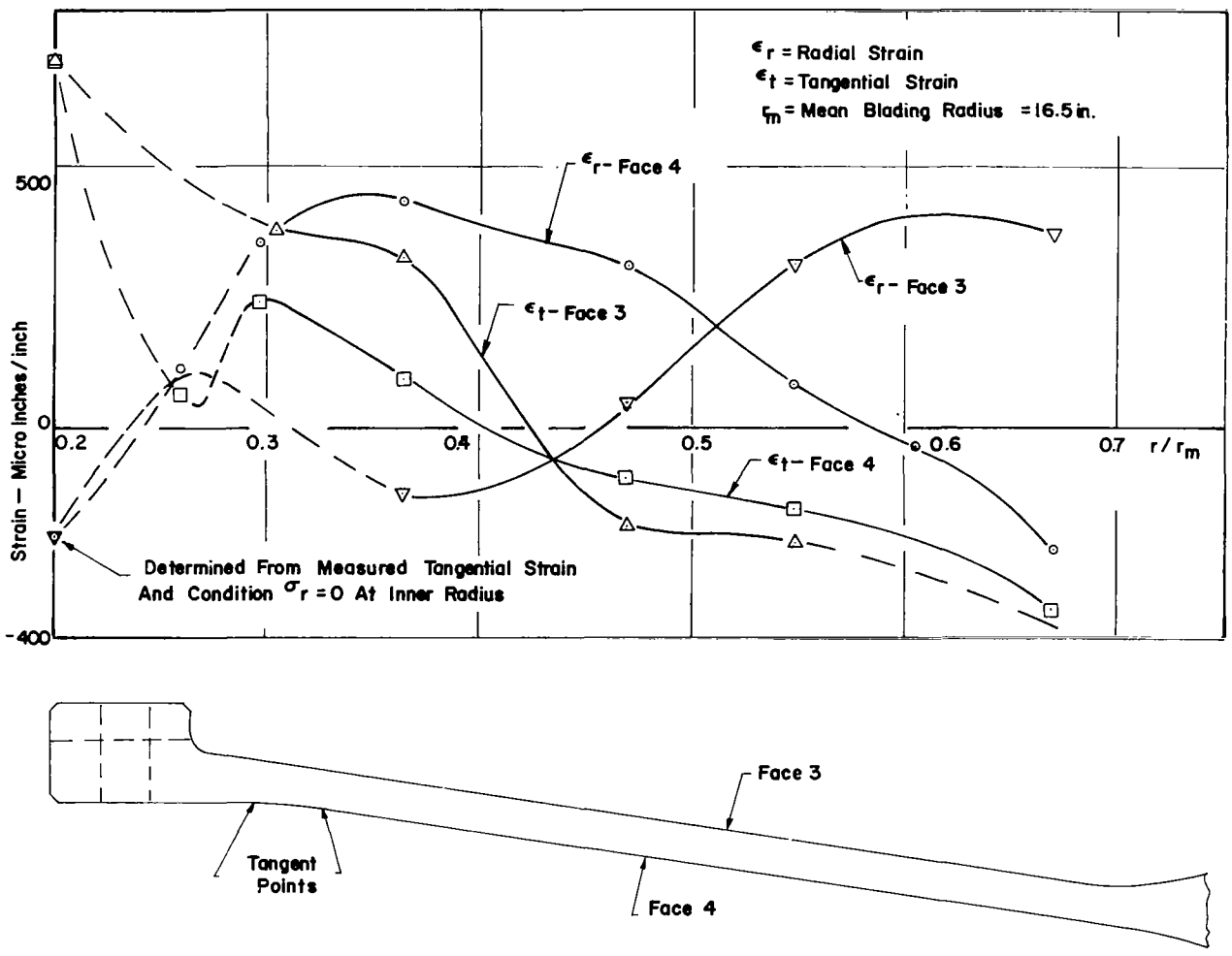


FIG. 35 THERMAL STRAINS ON SECOND-STAGE DISK AFTER 2.0 HOURS AT 6 KW PLUS 1.0 HOUR AT 0 KW (Broken lines in hub region represent approximate strain distributions estimated from a limited number of data points.)

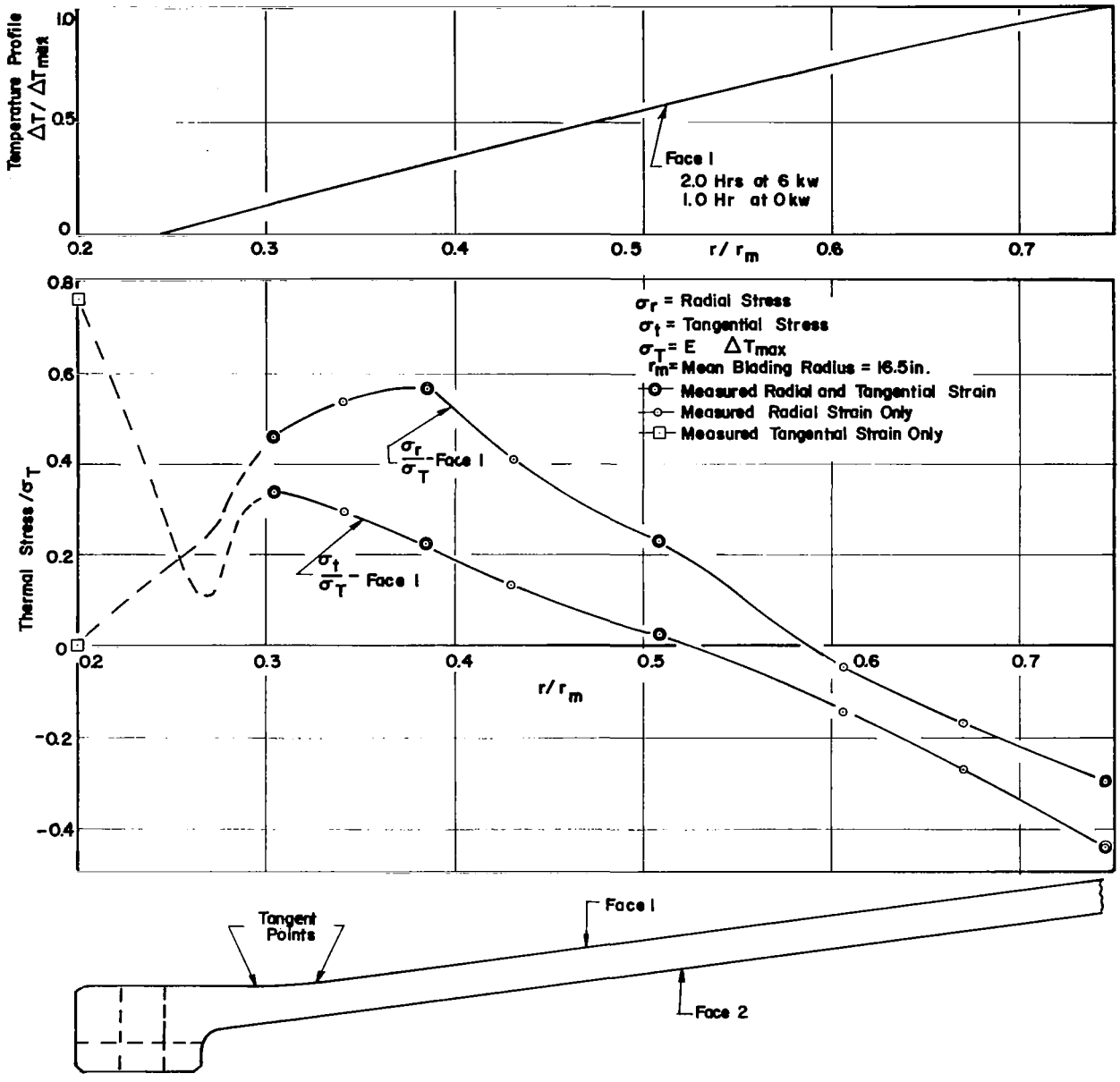


FIG. 36 DIMENSIONLESS THERMAL STRESSES ON FIRST-STAGE DISK AFTER 2.0 HOURS AT 6 KW (Stress distributions based on estimated strains are shown by broken lines.)

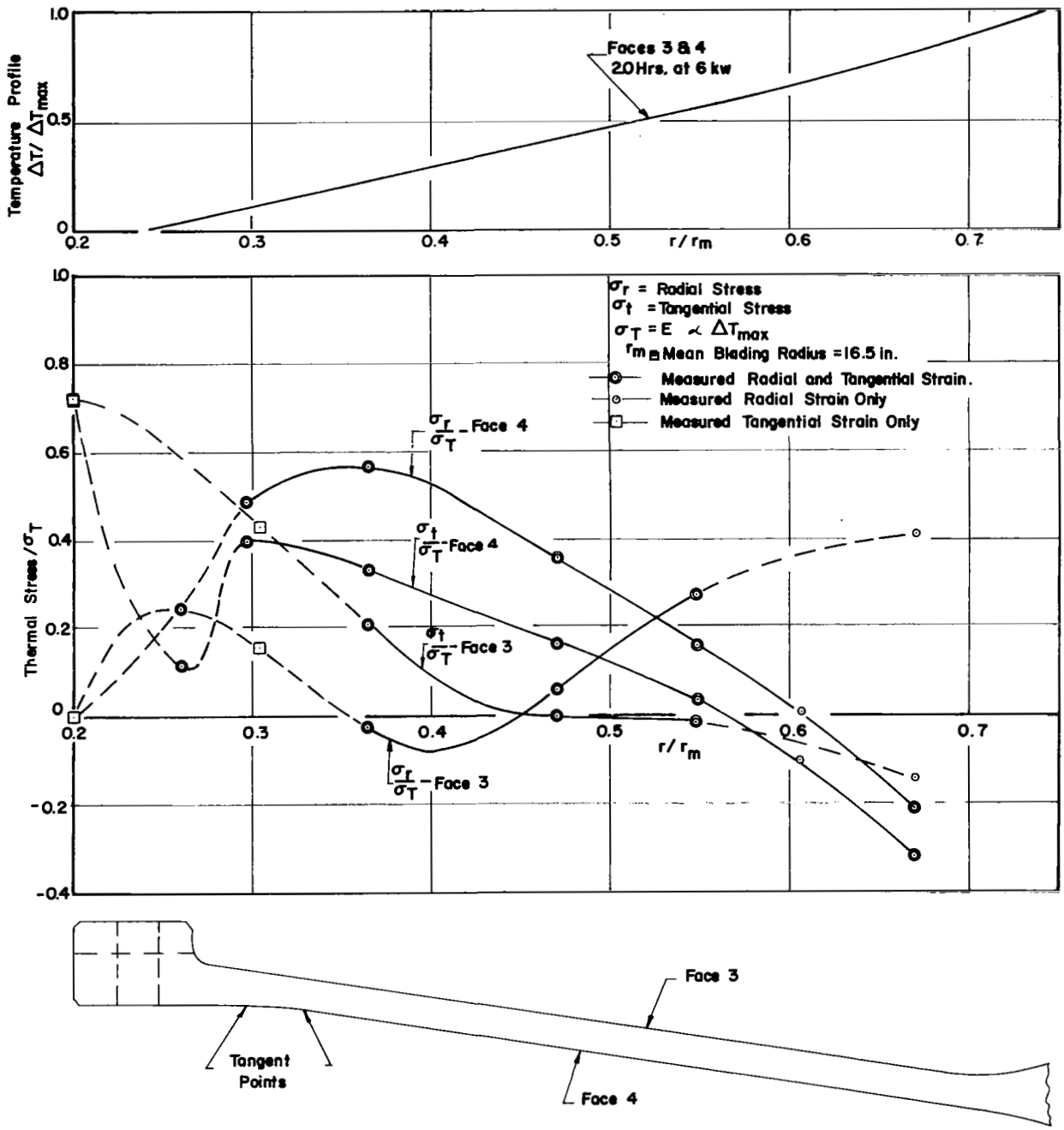


FIG. 37 DIMENSIONLESS THERMAL STRESSES ON SECOND-STAGE DISK AFTER 2.0 HOURS AT 6 KW (Stress distributions based on estimated strains are shown by broken lines.)

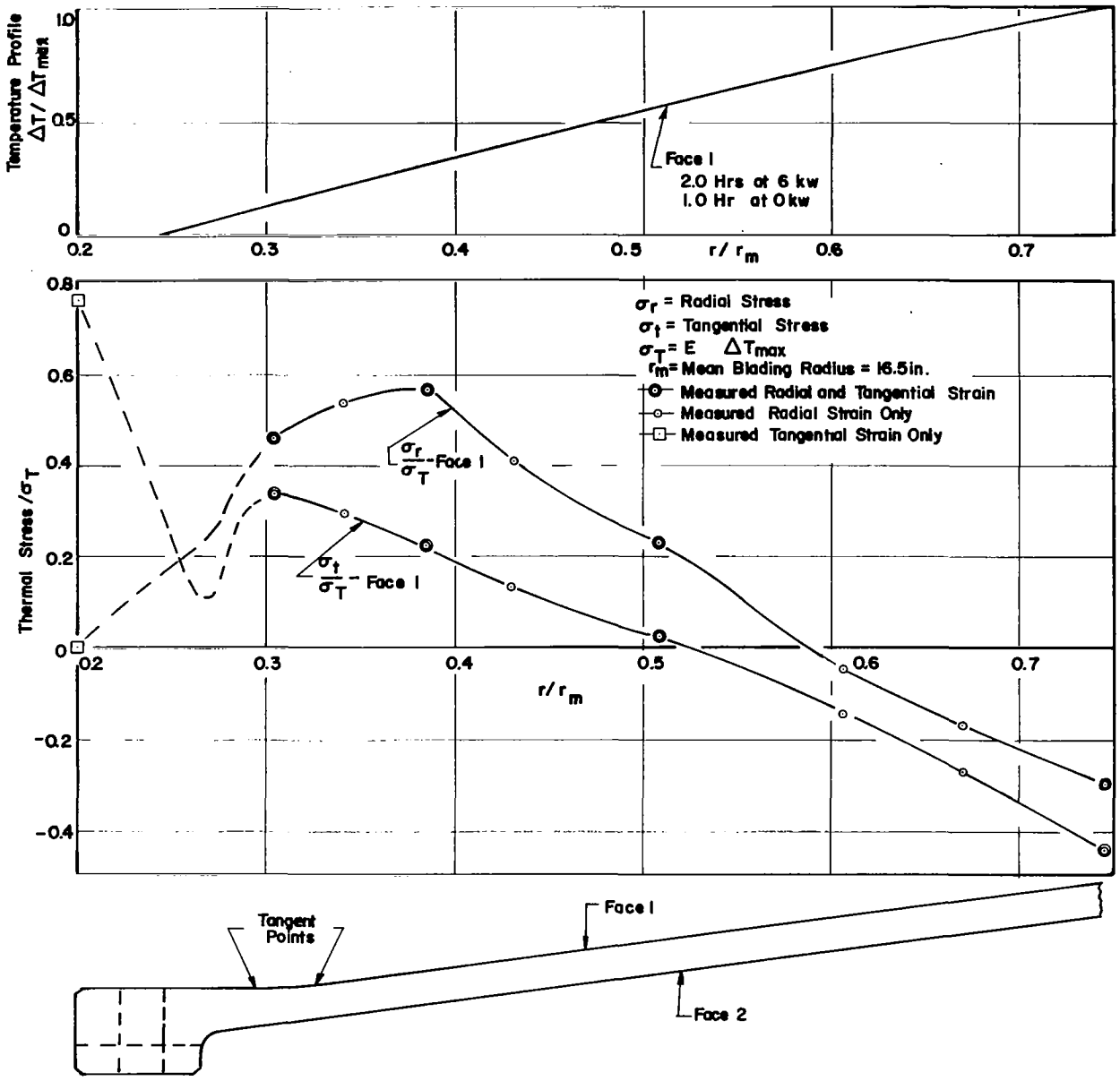


FIG. 38 DIMENSIONLESS THERMAL STRESSES ON FIRST-STAGE DISK AFTER 2.0 HOURS AT 6 KW PLUS 1.0 HOUR AT 0 KW (Stress distributions based on estimated strains are shown by broken lines.)

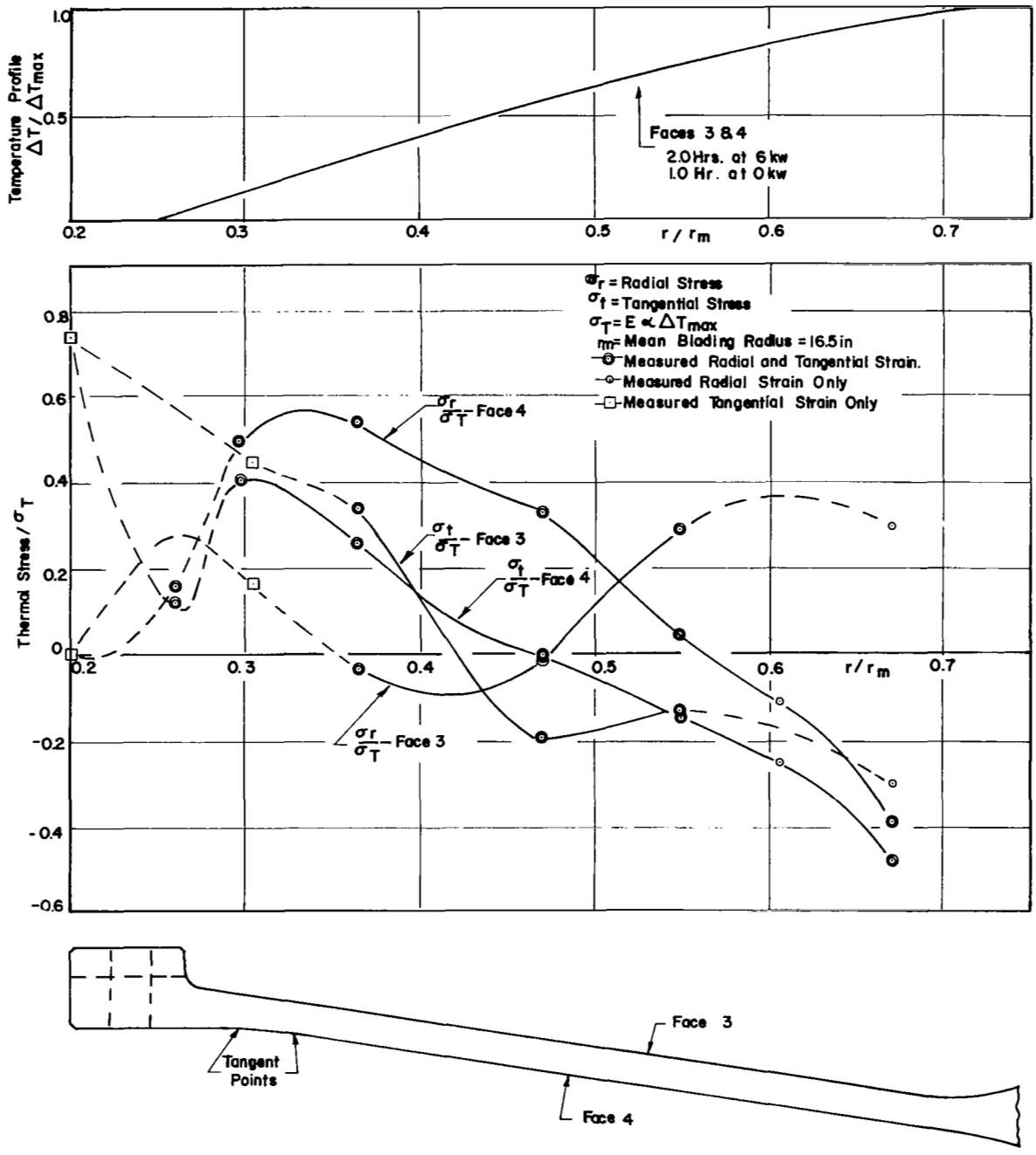


FIG. 39 DIMENSIONLESS THERMAL STRESSES ON SECOND-STAGE DISK AFTER 2.0 HOURS AT 6 KW PLUS 1.0 HOUR AT 0 KW (Stress distributions based on estimated strains are shown by broken lines.)

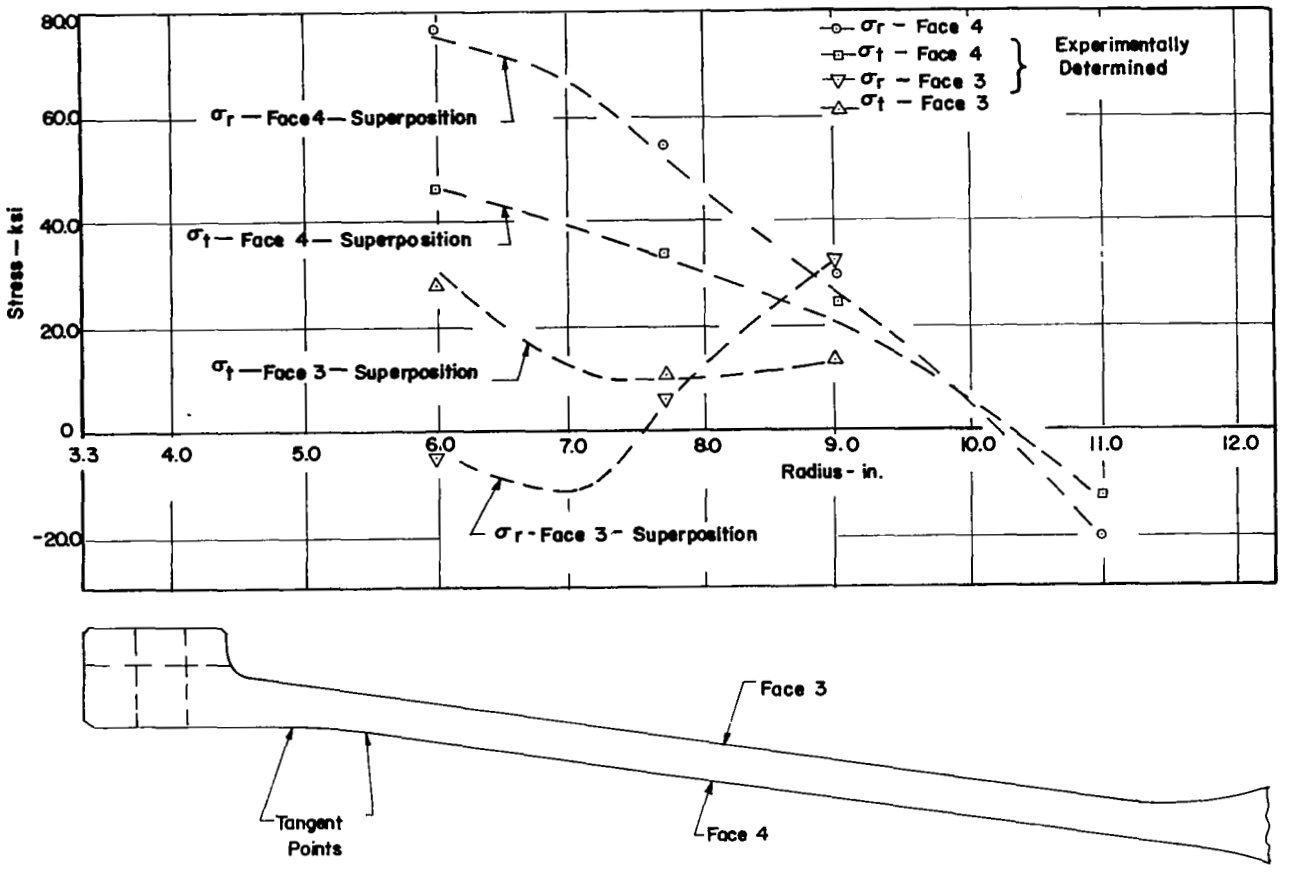


FIG. 40 STRESSES ON SECOND-STAGE DISK DUE TO COMBINED THERMAL AND CENTRIFUGAL LOADS OF 2.0 HOURS AT 6 KW AND 3,000 RPM (Data points denote stresses determined from experimental strains measured during combined-load tests. Broken lines denote stress distributions determined by superposition of separate high-temperature and spin test results.)

| GAGE NO. | GAGE LOCATION | | | | STRAIN AT 4000 RPM Microinches/inch | | |
|---|---|---|---|---|---|---|---|
| | Stage 1-1st 2-2nd | Surface O=Outer I=Inner | Direction Radial Tangential | Radius Inches | Maximum | Minimum | Average |
| 1 | 1 | Hub | T | 3.300 | 2095 | 1840 | 2017 |
| 2 | 1 | 0 | T | 12.473 | no | data | available |
| 3 | 1 | 0 | R | 12.473 | -295 | -180 | -235 |
| 4 | 1 | 0 | T | 6.350 | 595 | 540 | 567 |
| 5 | 1 | 0 | R | 6.350 | 1510 | 1405 | 1457 |
| 6 | 1 | 0 | T | 8.387 | 1055 | 870 | 979 |
| 7 | 1 | 0 | R | 8.387 | 1145 | 920 | 1112 |
| 8 | 1 | 0 | T | 3.922 | 615 | 405 | 539 |
| 9 | 1 | 0 | R | 3.922 | 155 | 80 | 117 |
| 10 | 1 | Rim | T | 13.000 | 825 | 800 | 806 |
| 11 | 1 | I | T | 11.905 | 880 | 810 | 831 |
| 12 | 1 | I | R | 11.905 | 1355 | 995 | 1195 |
| 13 | 1 | I | T | 9.100 | 725 | 565 | 637 |
| 14 | 1 | I | R | 9.100 | 365 | 280 | 322 |
| 15 | 1 | I | T | 5.696 | 1485 | 1100 | 1244 |
| 16 | 1 | I | R | 5.696 | -475 | -470 | -472 |
| 17 | 1 | I | T | 4.875 | 1540 | 1440 | 1509 |
| 18 | 1 | I | R | 4.875 | 605 | 355 | 480 |
| 19 | 2 | Hub | T | 3.300 | 1755 | 1395 | 1642 |
| 20 | 2 | 0 | R | 11.547 | -540 | -505 | -519 |
| 21 | 2 | 0 | T | 11.547 | 975 | 875 | 916 |
| 22 | 2 | 0 | R | 9.079 | 690 | 470 | 614 |
| 23 | 2 | 0 | T | 9.079 | 965 | 945 | 953 |
| 24 | 2 | 0 | R | 5.743 | 1520 | 1215 | 1304 |
| 25 | 2 | 0 | T | 5.743 | 770 | 485 | 667 |
| 26 | 2 | 0 | R | 4.290 | 270 | 145 | 182 |
| 27 | 2 | 0 | T | 4.290 | 610 | 480 | 547 |
| 28 | 2 | Rim | T | 13.000 | 845 | 760 | 792 |
| 29 | 2 | I | T | 11.131 | 835 | 760 | 805 |
| 30 | 2 | I | R | 11.131 | 1070 | 955 | 1036 |
| 31 | 2 | I | T | 8.787 | 770 | 670 | 717 |
| 32 | 2 | I | R | 8.787 | 820 | 260 | 411 |
| 33 | 2 | I | T | 5.709 | 1025 | 935 | 985 |
| 34 | 2 | I | R | 5.709 | -425 | -285 | -325 |
| 35 | 2 | I | T | 4.903 | 1330 | 1280 | 1290 |
| 36 | 2 | I | R | 4.903 | no | data | available |

NOTE - Gage numbers correspond to Drawing 2007-2A, Appendix D

Table 1 STRAIN DATA FROM PRELIMINARY SPIN TESTS

| MEASURING STATIONS | DIMENSIONAL CHANGE IN INCHES | | | | |
|---|---|---|---|---|---|
| | PERIPHERAL POSITION OF WHEEL | | | | |
| | I | II | III | IV | AVERAGE |
| 1A & 1B | -.001 | -.004 | -.005 | -.003 | -.00325 |
| 2A & 2B | -.001 | -.002 | -.001 | -.002 | -.0015 |
| 3A & 3B | .001 | -.002 | .001 | .001 | .00025 |
| 4A & 4B | -.002 | -.004 | -.006 | -.005 | -.00425 |
| 5A & 5B | -.004 | -.005 | -.005 | -.004 | -.0045 |
| 6A & 6B | .008 | .006 | .005 | .006 | .00625 |
| 7A & 7B | .004 | .003 | .002 | .004 | .00325 |
| 8A & 8B | .003 | -.001 | .001 | .000 | .00075 |
| 13A & 12B | .008 | .001 | .000 | .006 | .00375 |
| Actual Spacing Between Rims at Spacer Drum | .0015 | .003 | .002 | .001 | .002 |

NOTES - Measuring stations correspond to Drawing 2022, Appendix D.

- Dimensions listed oposite the respective measuring stations indicate a change in the distance between the outer surfaces of the two rotors. A negative sign indicates the distance has decreased.

Table 2 TEST ROTOR DIMENSIONAL CHANGES AFTER 6000 RPM SPIN TEST FOR FABRICATION EVALUATION

| | 0.2% Yield Strength ksi | Ultimate Tensile Strength ksi | Young's modulus psi x $10^{-6}$ | Percent Reduction of Area |
|---|---|---|---|---|
| Certified test by material supplier - heat treated | 165.0 | 198.5 | --- | 37.0 |
| Average of hub bolt tests (Table C1) - annealed specimen | --- | 113.9 | --- | 30.0 |
| Tensile test specimen - annealed | 69.1 | 114.3 | 24.3 | 35.6 |
| Tensile test specimen - heat treated | 142.8 | 185.2 | 29.1 | 19.4 |

- Heat treatment consisted of 10 hrs at 1400°F, furnace cooling to 1200°F, holding at 1200°F until total aging time was approximately 20 hrs, and air cooling to ambient.

- Details of tensile tests are given in Appendix C.

- 0.2% Yield Strength and Ultimate Tensile Strength are based on original areas (i.e. are engineering values).

Table 3 SUMMARY OF TENSILE TEST RESULTS FOR ANNEALED AND HEAT TREATED IN 718 HUB BOLTS AND TENSILE SPECIMENS

| GAGE LOCATION | | CENTRIFUGAL TESTS | | ELEVATED TEMPERATURE TESTS (200 rpm) | | | |
|---|---|---|---|---|---|---|---|
| | | Strain at 4000 rpm | | Strain after 2hrs at 6KW | | Strain after 2hrs at 6KW + 1 hr at 0KW | |
| Face | Radius in | Radial microin/in | Tangential microin/in | Radial microin/in | Tangential microin/in | Radial microin/in | TTangential microin/in |
| 1 | 3.300 | -539** | 1860 | -672** | 2316 | -216** | 747 |
| | 4.000 | -117 | 496 | - 94 | 530 | no data | no data |
| | 5.020 | 700 | 695 | 1010 | 714 | 353 | 199 |
| | 5.625 | 1165 | no gage | 1433 | no gage | 444 | no gage |
| | 6.350 | 1095 | 550 | 1387 | 297 | 490 | 56 |
| | 7.100 | 1100 | no gage | 1270 | no gage | 364 | no gage |
| | 8.387 | 850 | 715 | 865 | 84 | 220 | - 43 |
| | 9.037 | 715 | no gage | 680 | no gage | no data | no gage |
| | 10.000 | 450 | no gage | 353 | no gage | - 5 | no gage |
| | 11.020 | 80 | no gage | 80 | no gage | - 88 | no gage |
| | 12.300 | -210 | 730 | - 90 | -982 | -164 | -351 |
| 2 | 5.020 | 15 | 1330 | 78* | 1083* | no data | no data |
| | 6.350 | -295 | 795 | -140* | 303* | no data | no data |
| | 7.100 | no gage | 620 | no gage | 133* | no data | no data |
| | 8.387 | - 70 | 510 | 260* | - 95* | no data | no data |
| | 10.000 | 310 | no gage | 892* | no gage | no data | no data |
| | 11.925 | 820 | 630 | 1100* | -790* | no data | no data |
| 3 | 5.020 | no data | 1195 | no data | 1157 | no data | 380 |
| | 6.013 | -300 | 790 | -271 | 651 | -125 | 328 |
| | 7.750 | -130 | 575 | 176 | - 54 | 44 | -185 |
| | 9.037 | 265 | 650 | 844 | -284 | 313 | -212 |
| | 11.020 | 1015 | 810 | 1412 | no data | 370 | |
| 4 | 3.300 | -474** | 1635 | -627** | 2163 | -203** | +700 |
| | 4.290 | 525 | - 30 | 642 | 120 | 115 | 68 |
| | 4.903 | 725 | 590 | 1110 | 767 | 355 | 241 |
| | 6.013 | 1210 | 580 | 1423 | 494 | 436 | 95 |
| | 7.750 | 920 | 730 | 934 | 170 | 310 | - 97 |
| | 9.037 | 450 | 826 | 462 | - 36 | 87 | -154 |
| | 10.000 | 145 | no gage | 115 | no gage | - 34 | no gage |
| | 11.020 | -410 | 875 | -350 | -784 | -236 | -350 |

NOTES + = Tension
- = Compression
* = Unverified data taken prior to loss of Face 2 instrumentation
** = Calculated from Condition $\sigma_r = 0$ at disk hub bore

Tabel 4 CORRECTED STRAIN DATA FROM ROOM TEMPERATURE SPIN TESTS AND ELEVATED TEMPERATURE TESTS

| | Time From Room Temperature and Heater Input | | | | |
|---|---|---|---|---|---|
| | 2 hrs at 6 kw | 2.5 hrs at 6 kw | 2.5 hrs at 6 kw + 1 hr at 3.8kw | 1 hr at 10 kw | 3 hr at 5 kw |
| Temperature at radius = 13.0 in.-°F | 566 | 604 | 600 | 576 | 571 |
| Temperature at radius = 4.0 in.-°F | 210 | 256 | 355 | 146 | 254 |
| ΔT | 356 | 348 | 245 | 430 | 317 |
| Rate of temperature change during data recording °F/min | 4 | 4 | 3 | 14 | 4 |

NOTE - 2 hrs at 6 kw chosen as optimum. Other combinations exhibit either inadequate ΔT or excessive temperature change during data recording.

Table 5 CHARACTERISTICS OF DISK TEMPERATURE PROFILES FOR SEVERAL HEATER POWER INPUTS

## REFERENCES


1. Beer, R., AERODYNAMIC DESIGN AND ESTIMATED PERFORMANCE OF A TWO-STAGE CURTIS TURBINE FOR THE LIQUID OXYGEN TURBOPUMP OF THE M-1 ENGINE, NASA Report No. CR 54764, 19 November 1965.
2. Roesch, E., MECHANICAL DESIGN OF A CURTIS TURBINE FOR THE OXIDIZER TURBINE OF THE M-1 ENGINE, NASA Report No. CR 54815, 15 June 1966.
3. Beer, R., FABRICATION OF LIGHTWEIGHT TURBINE COMPONENTS USING ELECTRON-BEAM WELDING FOR THE ATTACHMENT OF SHEET METAL BLADES TO DISCS AND SHROUDS, NASA Report No. CR 54814, 15 October 1966.
4. Zlatin, N., Field, M., Koster, W., FINAL REPORT ON MACHINABILITY OF MATERIALS, Contract AF 33(615) - 5262.
5. Harshberger, R., Troutman, D., CENTRIFUGAL STRESSES IN CONICAL ROTORS AND ROTORS OF ARBITRARY CROSS SECTION, Masters Thesis, Naval Postgraduate School, May 1966.
6. Vavra, M., AGARD-VKI LECTURE SERIES ON FLOW IN TURBINES, - RADIAL TURBINES, Lecture Series 6, Part 4C, March 1968.
7. Dovey, D., Gadd, E., Mitchell, E., HEAT TREATMENT OF METALS, London: Addison-Wesley Publishing Company, Inc., 1963.

## APPENDIX A

## DESIGN OF SPECIAL EQUIPMENT

### 1. Rotor Suspension System

The 8 inch Barbour-Stockwell turbine, can have a maximum spindle diameter of 0.625 inch. With a 5/8 -32- Class 2 thread the minimum outer spindle diameter can be 0.57 inch. Thus, with a spindle central bore of 0.407 inch, the minimum cross sectional spindle area is 0.125 inch$^2$. The weight of the turbine rotor is about 380 pounds giving a maximum tensile stress of 3040 psi. With a spindle material having a yield stress of about 90.0 ksi, or a permissible shear stress of about 45.0 ksi, the maximum torque, $M_t$, that can be transmitted by the spindle is

$$M_t = \frac{\pi}{16}\left(\frac{.57^4 - .407^4}{.57}\right) \quad (45{,}000) = 1210 \text{ in-lb}$$

For a yield stress of 90.0 ksi, the maximum bending moment, $M_B$, that can be exerted on the spindle is equal to $M_t$, since

$$M_B = \frac{\pi}{32}\left(\frac{.57^4 - .407^4}{.57}\right) \quad (90{,}000) = 1210 \text{ in-lb}$$

Drawing 2007-2A of Appendix D shows that the C.G. of the turbine is located about 15 inches below the point where the spindle is attached to the arbor support. If the arbor were connected rigidly to the support an eccentricity, e, of the turbine rotor would produce a moment M of

$$M = m\,\omega^2\, e(15)$$

where

$m$ = mass of turbine rotor $= \frac{380}{32.2} = 11.8$ slug

$\omega = \frac{\pi}{30}(7000) = 730$ rad/sec at 7000 rpm, the maximum anticipated spin speed

$e$ = eccentricity (inch)

or

$$M = (11.8)(53.3)\,10^4(15)\,e = 9.44(10^7)e.$$

for $M = M_B = 1210$ in-lb the permissible eccentricity would be limited to

$$e = \frac{1.21 \times 10^3}{9.44 \times 10^7} = \frac{1.28}{10^5} \text{ inch}$$

Since it would not be possible to maintain such a small eccentricity, it was decided to suspend the arbor by a self-aligning ball bearing, Fafnir Type 304 S, which has a carrying capacity of about 1500 pounds. The torque is transmitted by pin 2016-8 (Drawing 2007-2A) of 0.2 inch diameter. For a torque of 1210 pounds, the shear stress in the pin is 40.0 ksi.

Arbor 2018-1 was used also to balance the rotor assembly. For this reason it was equipped with surfaces to accommodate two self-aligning ball bearings, Fafnir Type 208S, with a bore of 1.57 inch, which are 8 inches apart. With its axis horizontal for balancing, the deflection, f, of the arbor is about

$$f = \frac{380}{IE}\frac{\ell^3}{48} = \frac{(380)(8^3)}{\frac{\pi}{64}(1.57)^4(30)(10^6)(48)} = \frac{0.45}{10^3} \text{ inch}$$

The other elements of the arbor attachment were calculated such that permissible stresses are not exceeded for either a torque of 1210 in-lb, or an axial load of 380 pounds.

As shown in paragraph A.2 the turbine rotor assembly has a polar mass moment of inertia of 141.2 in-lb-sec$^2$. In order to avoid damage to the hollow spindle, that is, to insure that the moment of 1210 in-lb which it can safely handle, is not exceeded, the accelerations or decelerations of the drive assembly must be limited. From

$$\theta_p \frac{d\omega}{dt} = M = 1210 \text{ in-lb},$$

$$\frac{d\omega}{dt} = \pm \frac{1210}{141.2} = 8.57 \frac{\text{rad/sec}}{\text{sec}},$$

the maximum possible time rate of speed N is

$$\frac{dn}{dt} = 4930 \frac{\text{rpm}}{\text{min}}$$

For safety reasons the unit was therefore not accelerated or decelerated by more than about 1000 rpm per minute

2. Measuring and Balancing Rig

a. Determination of Flexibility of Flexures. It was assumed that the natural frequency of the system with one bearing clamped and the other freely supported by the flexure would occur at a speed of 100 rpm. The natural frequency of the system of Fig. A1 was determined from the condition that the time rate of change of the angular momentums of the system must be equal to the moments that are exerted on it.

For deflections in the y-direction of Fig. A1, and with the C. G. of the rotor located halfway between the two supports, there are

$$\frac{d}{dt}(\theta_a \dot{\beta}) = M_z$$

and

$$\frac{d}{dt}(\theta_p \omega \beta) = M_y$$

where

$\theta_a$ = mass moment of inertia of rotor for a line perpendicular to shaft

$\beta$ = angle of deflection

$\dot{\beta} = \frac{d\beta}{dt}$

$\theta_p$ = polar mass moment of inertia

$M_z$ = moment about z-axis

$M_y$ = moment about y-axis

For a rotor without unbalance the moment $M_y$ is zero, and $M_z$ is produced by the spring force F. Let

$$F = c\, y$$

where c is the spring constant of one flexure. Then

$$M_z = - F \frac{L}{2} = - c \frac{L}{2} y$$

Further

$$\beta = \frac{y}{L} \text{ and } \dot{\beta} = \frac{\dot{y}}{L}$$

Then

$$\frac{d}{dt}\left(\theta_a \frac{\dot{y}}{L}\right) = - c\frac{L}{2}\, y = \frac{\theta_a}{L} \ddot{y}$$

or

$$\ddot{y} + \frac{cL^2}{2\theta_a} y = 0$$

The angular velocity $\omega_c$ at resonnance is then obtained from

$$y = A \cos(\omega_c t)$$

giving

$$\omega_c = \sqrt{\frac{cL^2}{2\theta_a}}$$

For 100 rpm the value of $\omega_c$ must be $\frac{\pi}{30}$ (100), or about 10 radians per second.

For bodies of revolution of the type shown in Fig. A2, whose meridional cross sectional area is symmetrical with respect to an axis parallel with the axis of symmetry, there are

$$\theta_p = 2\pi\rho R(R^2 A + 3I_m)$$

$$\theta_a = \pi\rho R(R^2 A + 3I_m + 2I_a)$$

where

$\theta_p$ = polar mass moment of inertia

$\theta_a$ = mass moment of inertia with respect to axis a-a perpendicular to axis of symmetry

$A$ = cross sectional area in meridional plane

$I_m$ = moment of inertia of A with respect to axis m-m of Fig. A2

$I_a$ = moment of inertia of A with respect to axis a-a of Fig. A2 = $I_n + A\,x^2$

$I_n$ = moment of inertia of A with respect to axis n-n of Fig. A2

$\rho$ = mass density of material

The turbine disks and the hub were replaced by 18 bodies of revolutions of the type for which the above-listed equations hold. For Inconel 718 with a specific weight of 0.297 lb/in$^3$, or $\rho = 0.297/(32.17 \times 12) = 7.69(10^{-4})$ lb/sec$^2$/in$^4$, the summation of the values for the individual cross-sectional areas gave:

$$\theta_p = 141.2 \text{ (in-lb) sec}^2$$

$$\theta_a = 73.2 \text{ (in-lb) sec}^2$$

The same replacement of the actual disk shape was used also to determine the weight w of the bladed turbine disks and the hub, and was found to be

$$w = 317 \text{ lb.}$$

For L = 8 in, $\theta_a = 73.2$ (in-lb) $\text{sec}^2$, the spring constant c of the flexure for $\omega_c = 10$ rad/sec is

$$c = \frac{2 w_c^2 \theta_a}{L^2} = 228 \text{ lb/in.}$$

b. Determination of Dimensions of Flexure. Design considerations established the length "$\ell$" and axial width "b" of the flexure (parts 2026-1 to 3 of Drawing 2022 Appendix D) as

$$\ell = 14 \text{ inches}$$

$$b = 2 \text{ inches}$$

It was then necessary to determine its thickness "t" to give the necessary spring constant. A check was made also to insure that the flexure is safe against buckling. Of interest is further the deflection $\Delta x$ of the flexure if an assumed force of 100 pounds is acting on it in the direction of the rotor axis. The flexures are made of Aluminum 6061-T651 with $E = 10(10^6)$ psi.

The critical buckling force $F_B$ is

$$F_B = \frac{\pi^2}{4} \frac{IE}{\ell^2} = \frac{\pi^2}{4} = \frac{b\, t^3}{12} \frac{E}{\ell^2}$$

Since one flexure has to support about 170 pounds, the safety factor $\upsilon$ against buckling is

$$\upsilon = F_B/170$$

Permissible forces acting on a column also depend on the slenderness ratio

$$\lambda = \frac{\ell}{i} = \frac{\ell}{I/A} ,$$

or the compressive stress, $\sigma_c = F_B/A$, must not exceed the elastic limit of the material, if the slenderness ratios are small. Fig. A3 shows the calculated data. For a spring constant c = 228 lb/in the flexure thickness t must be about 0.5 inch. A flexure of this thickness is safe against

buckling. Since an attainable speed of 100 rpm with the existing source of air was an assumption, and because of the simplifying assumptions made for the calculations (stiff shaft, ignoring of gyroscopic effect and bearing restraints) it was decided to manufacture two additional pairs of flexures with t = 0.28 inch, and t = 0.38 inch, giving values of c of 42 and 100 lb/in respectively. Other quantities remaining equal, the three sets of flexures would produce resonance conditions at $\omega_c$ = 100%, 66%, and 42%, for t = 0.5, 0.38, and 0.28 inch, respectively. Due to its large slenderness ratio the thinnest flexure will not buckle.

3. Rotor Handling Rig

The handling rig must be capable of supporting the rotor assembly whether its axis is horizontal or vertical. Its design must be such that it can be lifted by a crane, and that the rotor can be located above the flange of the spin pit for assembly purposes, and to assure that no damage will occur.

Drawing 2021-1 shows the design of the rig. The aluminum extrusions have dimensions of 1-3/4 x 3 x 1/8 inch wall thickness. The maximum and minimum moments of inertia are 1.3379 and 0.5564 $in^4$, with corresponding section moduli of 0.8919 and 0.6359 $in^3$, respectively.

For the rotor axis in vertical position, each of the three extrusions of 52 inch length must support 380/3 = 127 pounds, giving a bending moment of (127)(52)/4 = 1650 in-lb. The maximum bending stress is 1650/0.6359 = 2600 psi, and the deflections f of the members are

$$f = \frac{(127)(52)^3}{(0.5564)\ 10(10^6)48} = 0.067 \text{ inch}$$

The bending moment exerted on the 5/8 inch diameter pins, (2021-4), that hold the wooden blocks is about (127)(3) = 381 in-lb, giving a bending stress of 381/0.024 = 16,000 psi if one of the two pins carries all the load.

With the rotor axis horizontal, one of the three extruded members carries the whole rotor weight. The bending stress in the midsection of that member is then

$$\sigma_B = 2600 \times 3 \times \frac{0.6359}{0.8919} = 5600 \text{ psi}$$

and its deflection f becomes

$$f = 0.067 \times 3 \times \frac{0.5564}{1.3379} = 0.083 \text{ inch}$$

The material of the extrusions has a yield strength of about 35,000 psi, hence, even with a stress concentration factor of two because of the holes for steel pins, the safety factor of the rig is more than 2.5.

If the rig is suspended by a sling attached to rod 20? -13, that is inserted in spindle 2021-10 having a diameter of 0.75 inch, the diameter d of the rod is obtained from

$$\frac{\pi}{4}(0.75^2) - (0.75d) = \frac{Fk}{\sigma}$$

and

$$\frac{\pi}{4} d^2 \tau = \frac{F}{2}$$

where

F = load

k = stress concentration factor

$\sigma$ = tensile stress in spindle

$\tau$ = shear stress in rod

for equal utilization of the rod and spindle materials. For equal materials with $\tau = \sigma/2$ and $k = 2$

$$d = 0.343$$

Then, with F = 400 lb.

$$\tau = \frac{200}{\pi/4d^2} = 2{,}200 \text{ psi}$$

$$k\sigma \approx 2\tau 2 = 8{,}800 \text{ psi}$$

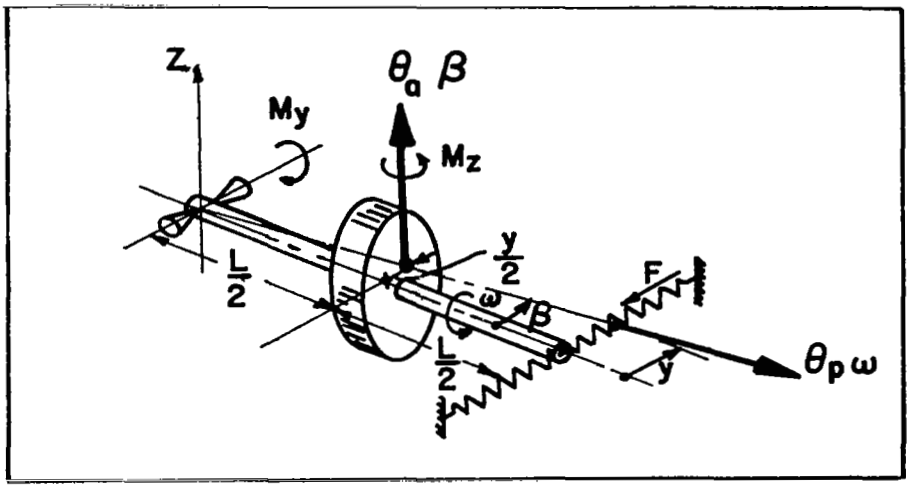


FIG. A1 PRINCIPLE OF ROTOR BALANCING SYSTEM

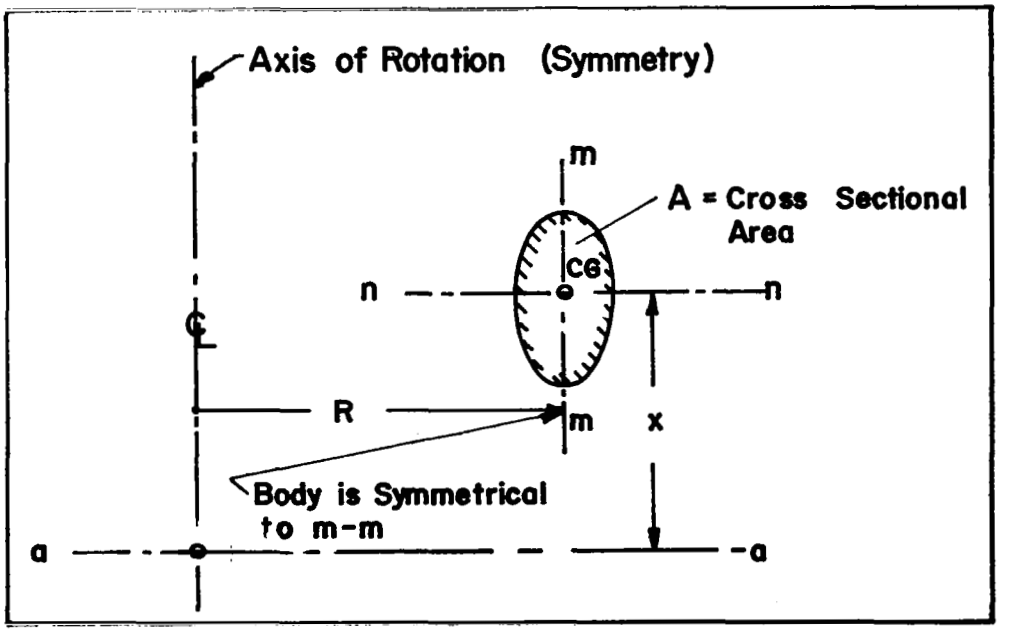


FIG. A2 MASS MOMENT OF INERTIA OF BODY OF REVOLUTION

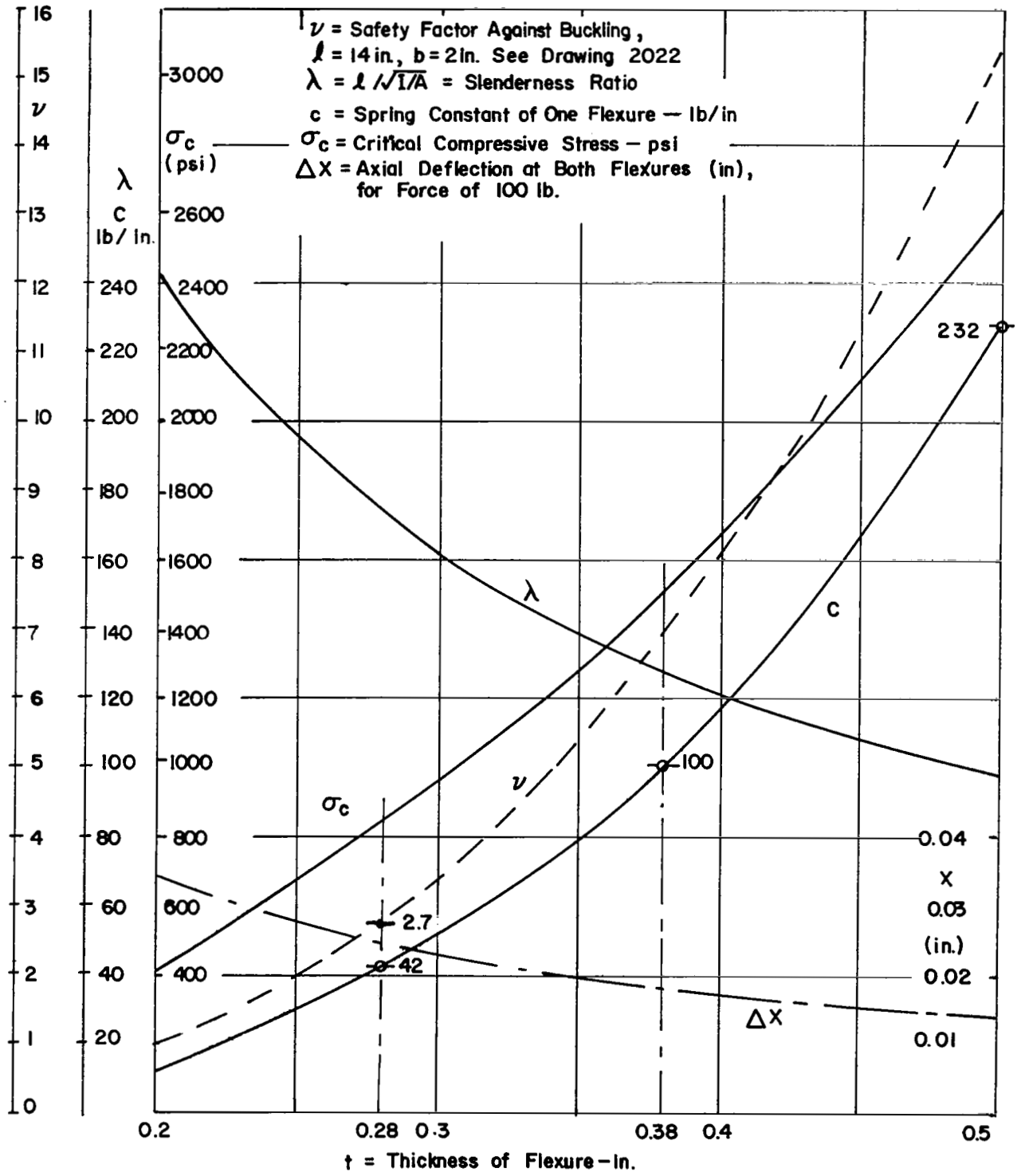


FIG. A3 EVALUATION OF BEARING FLEXURES

## APPENDIX B

## STRESS CALCULATIONS

### 1. Centrifugal Stress Due to Balance Weights

Figure B1 is a simplified model of s stage 2 single blade segment with balance weight. Figure 1 shows an actual balance weight mounted on the test rotor. The model was assumed in order to estimate the effect of balance weight on $\sigma_{rim}$, the total centrifugal stress at the disk rim, as indicated below.

$$\sigma_{rim} = \sigma_s + \sigma_b + \sigma_{bw} \qquad B(1)$$

$\sigma_s$ = centrifugal stress due to shroud - psi

$\sigma_b$ = centrifugal stress due to blade - psi

$\sigma_{bw}$ = centrifugal stress due to balance weight - psi

$$\sigma_s = F_s/A_b \qquad B(2)$$

$F_s$ = centrifugal force due to shroud - lb

$A_b$ = blade cross sectional area - $in^2$

Similarly,

$$\sigma_b = F_b/A_b \qquad B(3)$$

$$\sigma_{bw} = F_{bw}/A_b \qquad B(4)$$

In general,

$$F_{centrifugal} = m\,\omega^2\,R \qquad B(5)$$

m = mass - slugs

$\omega$ = angular velocity - radians/second

R = radius - ft

Eq. B(5) into Eqs. B(2), B(3) and B(4) gives (with Fig. B1)

$$\sigma_s = \frac{m_s \omega^2}{A_b}\,(R_o + t/2) \approx \frac{m_s \omega^2 R_o}{A_b} \qquad B(6)$$

where $m_s$ = mass of shroud segment

$= \rho\,(t)(s)(\ell)$ with $\rho$ = mass density = 15.95 lbf - $sec^2$ - $ft^{-4}$

for Inconel 718, and t, s, and $\ell$ in units of ft.

$$\text{or} \quad \sigma_s \approx \frac{(\rho)(t)(s)(\ell)\ \omega^2\ R_o}{A_b} \qquad \text{B(7)}$$

$$\sigma_{bw} = \frac{m_{bw}\ \omega^2}{A_b}\ (R_o - h/2) \approx \frac{m_{bw}\ \omega^2\ R_o}{A_b} \qquad \text{B(8)}$$

$$\text{or, with Eq. B(6),} \quad \sigma_{bw} \approx \frac{m_{bw}}{m_s}\ \sigma_s \qquad \text{B(9)}$$

$$\sigma_b = \frac{m_b\ \omega^2\ R_m}{A_b} \qquad \text{B(10)}$$

where $m_b$ = mass of blade = $\rho\ A_b\ H$ with H and $A_b$ in units of ft and $ft^2$ respectively

or

$$\sigma_b = \frac{\rho\ H\ \omega^2\ R_m}{144} \qquad \text{B(11)}$$

For the second stage disk, the following dimensions (shown in proper units) were obtained from Ref. 3.

$A_b = 0.241\ in^2 = 1.67\ (10^{-3})ft^2$
$t = 1.67\ (10^{-2})ft$
$R_o = 1.60$ ft
$R_m = 1.375$ ft
$H = 0.45$ ft
$\ell = 0.15$ ft

The balance weight mass per blade was found by weighing to be 7.71 grams, or $0.528 \times 10^{-3}$ slug. For the 94 blades of the second stage, s was obtained as:

$$s = R_o\ (\frac{360}{94})\ (\frac{\pi}{180}) = 0.167 \text{ ft}$$

For N = 6100 rpm,

$$\omega = \frac{\pi N}{30} = 638.47 \text{ radians/sec.}$$

Substitution into B(7), B(9), B(11), and B(1) yielded the stresses shown in Column A of Table B1.

Stainless steel balance weights, of maximum total mass 39.78 grams, were considered for the high temperature spin tests. Hence a second calculation was made to establish the effect of a stainless weight not

in uniform contact with the shroud. Nonuniform contact could occur with stainless steel weights due to slight curvature differences between the weight and the shroud and due to the inability of relatively stiff stainless steel to deform and match the shroud curvature at speed.

For the calculation it was assumed that the balance weight was concentrated at two points on the shroud giving 19.89 grams, or 1.36 ($10^{-3}$) slug, per blade. The results for the maximum speed of 4000 rpm are shown in Column B of Table B1.

2. Stress Distribution in a Straight Replacement Model of the Second Stage Rotor

The procedure for theoretical calculation of the centrifugal and thermal stress distributions in a conventional straight disk is given in this paragraph. The disk chosen is a model of the second stage rotor disk, as shown in Fig. B2. The results of this calculation, when compared to the experimental results obtained for the test rotor, permit qualitative assessment of the influence of the conical shape of the rotor.

a. Centrifugal Stress Distribution. Assuming that the centrifugal force of the shroud is equally supported by the 94 blades of the second stage, there are from Fig. B2.

$r_s$ = mean radius = $\frac{r_4 + r_5}{2}$

$t_s$ = thickness = $r_5 - r_4$

$\ell_s$ = length = $\frac{2\pi r_s}{94}$

$b_s$ = width

$m_s$ = mass = $\rho(t_s)(b_s)(\ell_s)$ where $\rho$ = mass density for Inconel 718

Then $F_s$, the centrifugal force produced by one shroud segment is

$F_s = m_s \omega^2 r_s$ with $\omega$ = angular velocity, radians/sec.

For the rotor blade of cross-sectional area $A_b$,

mean radius $r_b = \frac{r_3 + r_4}{2}$,

height $h_b = r_4 - r_3$,

mass $m_b = \rho A_b h_b$,

the centrifugal force, $F_B$, is

$$F_b = m_b \omega^2 r_b$$

Then

$$F_s + F_b = \rho\omega^2 [(t_s)(b_s)(\ell_s)(r_s) + A_b h_b r_b]$$

The radial stress at the outer radius of the rim $r_3$ due to these forces is

$$\sigma_{r_3} = \frac{94(F_s + F_b)}{2\pi r_3 b_w} = \frac{94 \rho \omega^2}{2\pi r_3 b_w} [(t_s)(b_s)(\ell_s)(r_s)+(A_b)(h_b)(r_b)]$$

or

$$\frac{\sigma_{r_3}}{(\rho \omega^2 r_3^2)} = \frac{94}{2\pi r_3^3 b_w} [(t_s)(b_s)(\ell_s)(r_s)+(A_b)(h_b)(r_b)]. \quad B(12)$$

For the geometry of Fig. B2 using Eq. B(12)

$$\frac{\sigma_{r_3}}{\rho \omega^2 r_3^2} = 0.1002 \quad B(13)$$

Equations C(70) and C(71) of Ref. 6 give the stresses in a rotating ring of constant thickness. These equations applied to the rim give

$$\frac{(\sigma_r)_R}{\rho \omega^2 r_3^2} = - A\left(\frac{r}{r_3}\right)^2 + C_1 - \frac{C_2}{(r/r_3)^2} \quad B(14)$$

$$\frac{(\sigma_t)_R}{\rho \omega^2 r_3^2} = - B\left(\frac{r}{r_3}\right)^2 + \frac{C_2}{(r/r_3)^2} \quad B(15)$$

with $A = \frac{3+\nu}{8}$ , $B = \frac{1+3\nu}{8}$

$\nu$ = Poisson's Ratio = 0.29 for Inconel 718

$C_1$ & $C_2$ are constants to be determined from the boundary conditions.

Eq. B(14) and B(15) may be written as

$$\frac{(\sigma_r)_R}{\rho\,\omega^2\,r_2^2} = \left[-A\left(\frac{r}{r_3}\right)^2 + C_1 - \frac{C_2}{(r/r_3)^2}\right]\left(\frac{r_3}{r_2}\right)^2 \qquad \text{B(16)}$$

$$\frac{(\sigma_t)_R}{\rho\,\omega^2\,r_2^2} = \left[-B\left(\frac{r}{r_3}\right)^2 + C_1 + \frac{C_2}{(r/r_3)^2}\right]\left(\frac{r_3}{r_2}\right)^2 \qquad \text{B(17)}$$

Also Eq. B(13) may be written as

$$\frac{\sigma_{r_3}}{\rho\,\omega^2\,r_2^2} = (0.1002)\left(\frac{r_3}{r_2}\right)^2 \qquad \text{B(18)}$$

The boundary conditions for the rim are

$\sigma_r = \sigma_{r_3}$ at $r = r_3$

$\sigma_r = (\sigma_{r_2})_R$ at $r = r_2$

Substituting into Eq. B(16) with Eq. B(18)

$$0.1002 = -A + C_1 - C_2 \qquad \text{B(19)}$$

$$\frac{(\sigma_{r_2})_R}{\rho\,\omega^2\,r_2^2} = \left[-A\left(\frac{r_2}{r_3}\right)^2 + C_1 - \frac{C_2}{(r_2/r_3)^2}\right]\left(\frac{r_3}{r_2}\right)^2 \qquad \text{B(20)}$$

Eq. B(19) and B(20) contain 3 unknown quantities, hence they are not sufficient for evaluation of the constants $C_1$ and $C_2$.

Applying Eqs. C(70) and C(71) of Ref. 6 to the disk of Fig. B2 gives

$$\frac{(\sigma_r)_D}{\rho\,\omega^2\,r_2^2} = -A\left(\frac{r}{r_2}\right)^2 + D_1 - \frac{D_2}{(r/r_2)^2} \qquad \text{B(21)}$$

$$\frac{(\sigma_t)_D}{\rho\,\omega^2\,r_2^2} = -B\left(\frac{r}{r_2}\right)^2 + D_1 + \frac{D_2}{(r/r_2)^2} \qquad B(22)$$

where $D_1$ and $D_2$ are constants.

The boundary conditions for the disk are

$$\sigma_r = (\sigma_{r_2})D \quad \text{at } r = r_2$$

$$\sigma_r = 0 \quad \text{at } r = r_1$$

Substituting into Eq. B(21)

$$\frac{(\sigma_{r_2})_D}{\rho\,\omega^2 r_2^2} = -A + D_1 - D_2 \qquad B(23)$$

$$0 = -A\left(\frac{r_1}{r_2}\right)^2 + D_1 - \frac{D_2}{(r_1/r_2)^2} \qquad B(24)$$

Equations B(19), B(20), B(23), and B(24) contain six unknowns and are not sufficient for evaluation of the unknown constants. However additional equations are obtained by writing equilibrium and deformation expressions at $r = r_2$. (see Fig. B3).

At $r_2$,

$$\Sigma F_y = 0 = (\sigma_{r_2})_D\, b_D - (\sigma_{r_2})_R\, b_R$$

or

$$(\sigma_{r_2})_D = (\sigma_{r_2})_R \left(\frac{b_R}{b_D}\right) \qquad B(25)$$

Also at $r_2$

$$u_R = u_D \qquad B(26)$$

However, $\epsilon_t = \frac{u}{r} = \frac{1}{E}(\sigma_t - \nu\,\sigma_r)$

Hence

$$\frac{E\,u_R}{r_2} = (\sigma_{t_2})_R - \nu\,(\sigma_{r_2})_R$$

$$\frac{E\,u_D}{r_2} = (\sigma_{t_2})_D - \nu\,(\sigma_{r_2})_D$$

and from Eq. B(26)

$$(\sigma_{t_2})_R - \nu\,(\sigma_{r_2})_R = (\sigma_{t_2})_D - \nu\,(\sigma_{r_2})_D \qquad \text{B(27)}$$

where $(\sigma_{t_2})_R$ and $(\sigma_{t_2})_D$ can be expressed in terms of $C_1$, $C_2$, and $D_1$, $D_2$ respectively using Eqs. B(17) and B(22).

Thus, by Eqs. B(25) and B(27), with Eqs. B(19), B(20), B(23), and B(24), a system of six equations with six unknowns is obtained. These equations when solved simultaneously for the geometry of Fig. B2 give

$$C_1 = 0.7225 \qquad C_2 = 0.2113$$

$$D_1 = 1.4648 \qquad D_2 = 0.1479$$

Substitution into Eq. B(16), B(17), B(21), and B(22) gives the following solutions for the centrifugal stress distributions in the uniform disk of Fig. B2.

$$\frac{(\sigma_r)_R}{\rho\,\omega^2\,r_2^2} = \left[-0.4112\left(\frac{r}{r_3}\right)^2 + 0.7225 - \frac{0.2113}{(r/r_3)^2}\right]\left(\frac{r_3}{r_2}\right)^2$$

$$\frac{(\sigma_t)_R}{\rho\,\omega^2\,r_2^2} = \left[-0.2340\left(\frac{r}{r_3}\right)^2 + 0.7225 + \frac{0.2113}{(r/r_3)^2}\right]\left(\frac{r_3}{r_2}\right)^2$$

$$\frac{(\sigma_r)_D}{\rho\,\omega^2\,r_2^2} = \left[-0.4112\left(\frac{r}{r_2}\right)^2 + 1.4648 - \frac{0.1479}{(r/r_2)^2}\right]$$

$$\frac{(\sigma_t)_D}{\rho\,\omega^2\,r_2^2} = \left[-0.2340\left(\frac{r}{r_2}\right)^2 + 1.4648 + \frac{0.1479}{(r/r_2)^2}\right]$$

These four equations can be multiplied by the ratio $(r_2/r_m)^2$, where $r_m$ = mean blade radius = 16.5 inches, to allow direct comparison with the results of Section VI. Thus

$$\frac{(\sigma_r)_R}{\sigma_R} = -0.2875\left(\frac{r}{r_3}\right)^2 + 0.5054 - \frac{0.1478}{(r/r_3)^2} \qquad \text{B(28)}$$

$$\frac{(\sigma_t)_R}{\sigma_R} = -0.1637\left(\frac{r}{r_3}\right)^2 + 0.5054 + \frac{0.1478}{(r/r_3)^2} \qquad B(29)$$

$$\frac{(\sigma_r)_D}{\sigma_R} = -0.2332\left(\frac{r}{r_2}\right)^2 + 0.8273 - \frac{0.0835}{(r/r_2)^2} \qquad B(30)$$

$$\frac{(\sigma_t)_D}{\sigma_R} = -0.1322\left(\frac{r}{r_2}\right)^2 + 0.8273 + \frac{0.0835}{(r/r_2)^2} \qquad B(31)$$

where $\sigma_R = \rho\,\omega^2\,r_m^2$

Equations B(28) through B(31) are the solution for the radial and tangential centrifugal stress distributions in the straight replacement model of Fig. B2. They are shown by the solid lines of Fig. B4.

b. Thermal Stress Distribution. Equations C(98) and C(99) of Ref. 6 give the thermal stresses in a stationary ring of constant thickness whose material properties are independent of temperature, when subjected to a temperature distribution expressed by $T = T_m + \Delta T_o (r/r_o)^n$. For the linear temperature profile of Fig. B2, chosen to approximate the 2.0 hours at 6 kw test point of the experimental program, there is n = 1. Then,

$$\frac{(\sigma_r)_R}{\alpha\, E(\Delta T_o)_R} = -\frac{1}{3}\left(\frac{r}{r_3}\right) + K_1 - \frac{K_2}{(r/r_3)^2} \qquad B(32)$$

$$\frac{(\sigma_t)_R}{\alpha\, E(\Delta T_o)_R} = -\frac{2}{3}\left(\frac{r}{r_3}\right) + K_1 + \frac{K_2}{(r/r_3)^2} \qquad B(33)$$

where $(\Delta T_o)_R = T_{r_3} - T_m$

$T_m$ = temperature at r = 0 = 46°F

$K_1$ & $K_2$ = unknown constants to be determined.

The boundary conditions for the rim are

$$\sigma_r = 0 \text{ at } r = r_3$$

$$\sigma_r = (\sigma_{r_2})_R \text{ at } r = r_2$$

Substitution into Eq. B(32) gives

$$0 = -1/3 + K_1 - K_2 \qquad \text{B(34)}$$

$$\frac{(\sigma_{r_2})_R}{\alpha E(\Delta T_o)_R} = -\frac{1}{3}\left(\frac{r_2}{r_3}\right) + K_1 - \frac{K_2}{(r_2/r_3)^2} \qquad \text{B(35)}$$

Applying Eqs. C(98) and C(99) of Ref. 6 to the disk

$$\frac{(\sigma_r)_D}{\alpha E(\Delta T_o)_D} = -\frac{1}{3}\left(\frac{r}{r_2}\right) + J_1 - \frac{J_2}{(r/r_2)^2} \qquad \text{B(36)}$$

$$\frac{(\sigma_t)_D}{\alpha E(\Delta T_o)_D} = -\frac{2}{3}\left(\frac{r}{r_2}\right) + J_1 + \frac{J_2}{(r/r_2)^2} \qquad \text{B(37)}$$

where $(\Delta T_o)_D = T_{r_2} - T_m$. The boundary conditions are

$$\sigma_r = (\sigma_{r_2})_D \quad \text{at } r = r_2$$

$$\sigma_r = 0 \quad \text{at } r = r_1$$

Substitution into Eq. B(36)

$$\frac{(\sigma_{r_2})_D}{\alpha E(\Delta T_o)_D} = -1/3 + J_1 - J_2 \qquad \text{B(38)}$$

$$0 = -1/3\left(\frac{r_1}{r_2}\right) + J_1 - \frac{J_2}{(r_1/r_2)^2} \qquad \text{B(39)}$$

Equations B(25) and B(27), the equilibrium equations at $r = r_2$, can also be applied to the case of thermal loads to complete the set of six equations with six unknowns.

Simultaneous solution of Eq. B(34), B(35), B(38), B(39), B(25), and B(27) yields

$$K_1 = 0.3902 \qquad K_2 = 0.0569$$

$$J_1 = 0.5021 \qquad J_2 = 0.0411$$

Substituting these values into Eqs. B(32), B(33), B(36), and B(37) gives

$$\frac{(\sigma_r)_R}{\sigma_T} = -0.3710\left(\frac{r}{r_3}\right) + 0.4343 - \frac{0.0633}{(r/r_3)^2} \qquad B(40)$$

$$\frac{(\sigma_t)_R}{\sigma_T} = -0.7419\left(\frac{r}{r_3}\right) + 0.4343 + \frac{0.0633}{(r/r_3)^2} \qquad B(41)$$

$$\frac{(\sigma_r)_D}{\sigma_T} = -\frac{1}{3}\left(\frac{r}{r_2}\right) + 0.5021 - \frac{0.0411}{(r/r_2)^2} \qquad B(42)$$

$$\frac{(\sigma_t)_D}{\sigma_T} = -\frac{2}{3}\left(\frac{r}{r_2}\right) + 0.5021 + \frac{0.0411}{(r/r_2)^2} \qquad B(43)$$

where $\sigma_T = \alpha E(\Delta T_o)_D$ and $(\Delta T_o)_R$ of Eqs. B(32) and B(40) is converted to $(\Delta T_o)_D$ by multiplication of the right hand sides by $r_3/r_2$. Equations B(40) through B(43) are expressions for the thermal stresses which exist in the straight replacement model of Fig. B2 with the chosen linear temperature distribution. They are shown by the broken lines of Fig. B4.

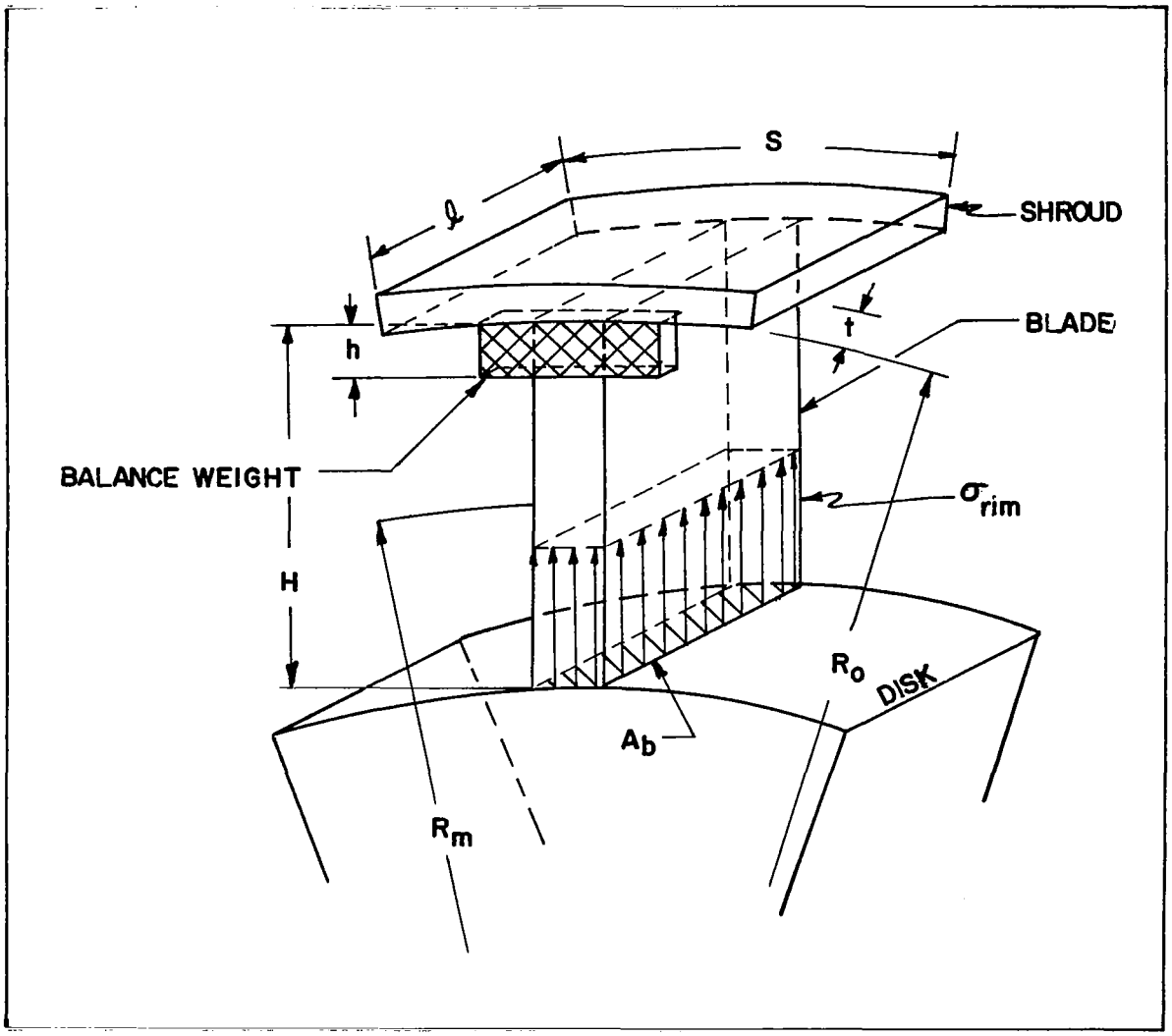


FIG. B1 MODEL OF BLADE SEGMENT WITH BALANCE WEIGHT ATTACHED

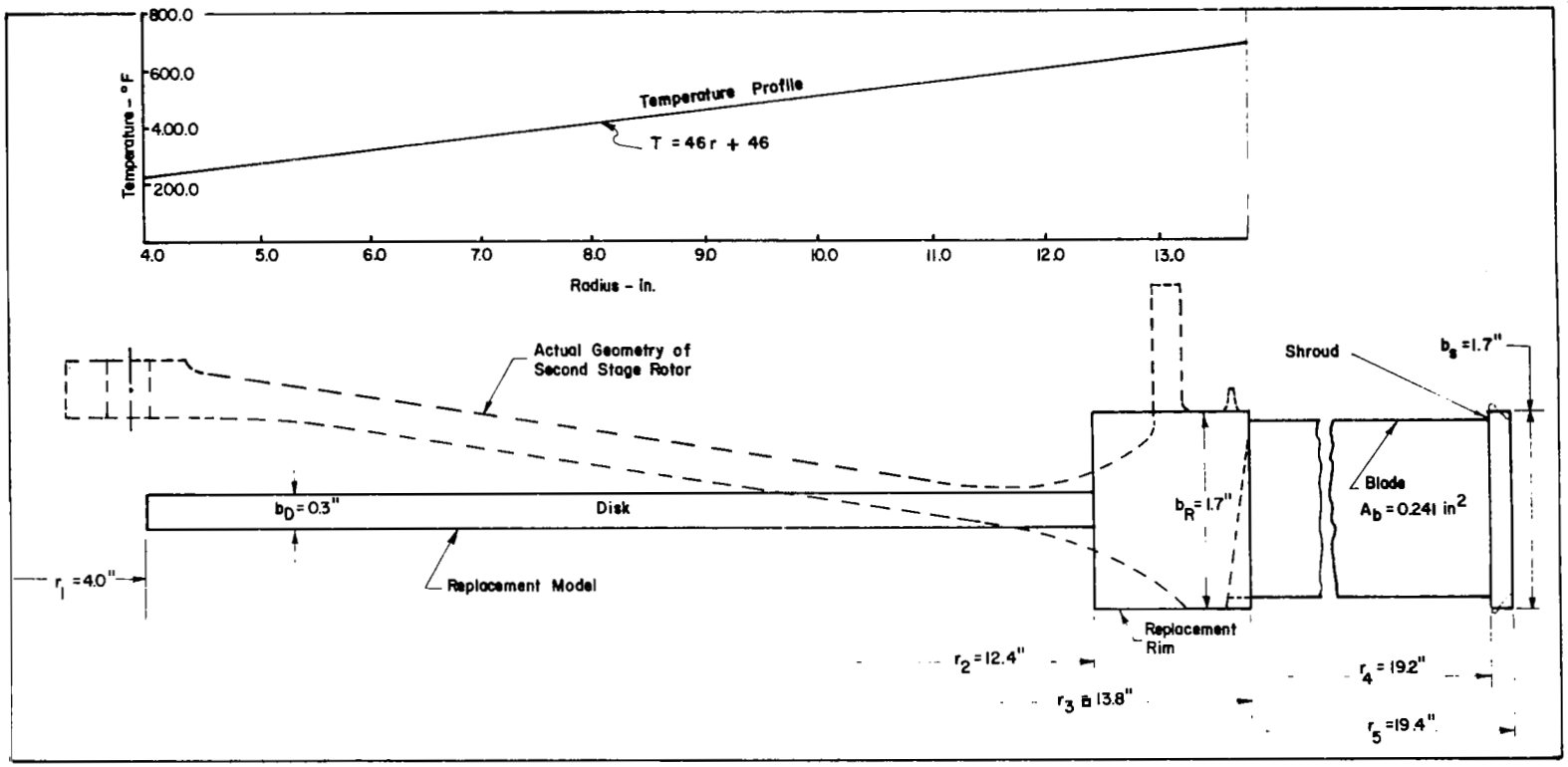


FIG. B2 CONSTANT CROSS SECTION MODEL OF SECOND STAGE DISK

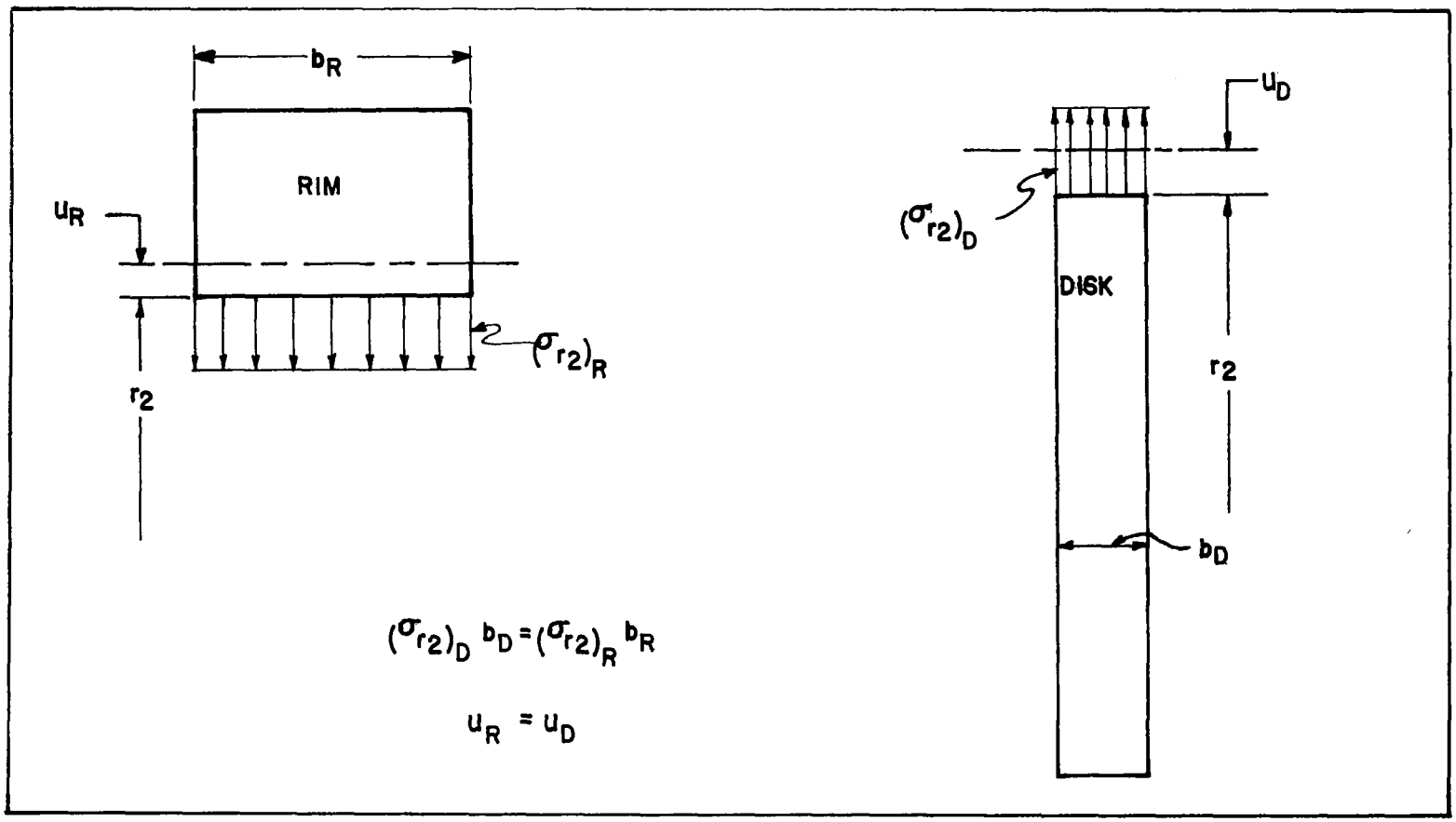


FIG. B3 EQUILIBRIUM CONDITIONS AT RADIUS $r_2$

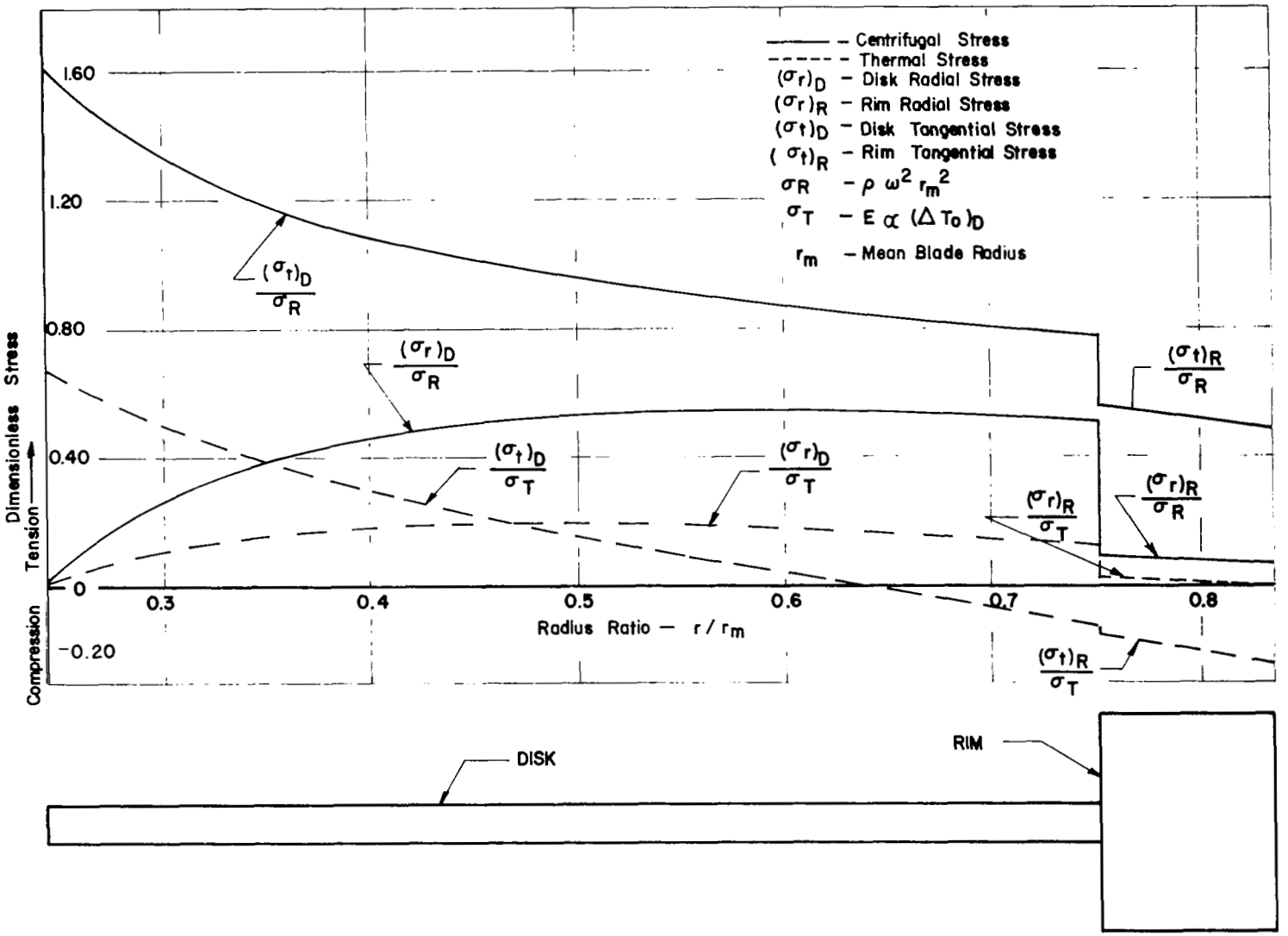


FIG. B4 CENTRIFUGAL AND THERMAL STRESS DISTRIBUTIONS IN REPLACEMENT MODEL OF SECOND STAGE ROTOR

| | A | B |
|---|---|---|
| $\sigma_s$ - psi | 11,600 | 5,000 |
| $\sigma_{bw}$ - psi | 1,400 | 1,600 |
| $\sigma_b$ - psi | 27,900 | 12,000 |
| $\sigma_{rim}$ - psi | 40,900 | 18,600 |
| $\frac{\sigma_{bw}}{\sigma_s + \sigma_b} \times 100$ - % | 3.54 | 9.41 |

NOTES - Column A is for balance weight of 7.71 grams per blade at 6100 rpm.

Column B is for balance weight of 19.8 grams grams per blade at 4000 rpm

Table B1 EFFECT OF BALANCE WEIGHT ON CENTRIFUGAL BLADE-DISK ATTACHMENT STRESS ($\sigma_{rim}$) OF SECOND STAGE DISK

## APPENDIX C

## HUB BOLT TEST PROGRAM

The unexpected elongation of the hub attaching bolts described in Section IV.B.3 (Spin Test for Fabrication Evaluation) raised questions concerning the magnitude of forces which caused the bolts to stretch, and also concerning the strength of the Inconel 718 bolt material. Tensile tests were therefore conducted on all nine of the stretched hub bolts, on four unused spare bolts, and on an Inconel 718 tensile test specimen.

The fourteen tensile tests were made in two different machines; namely, six of the used bolts, two of the unused spare bolts and the tensile test specimen were loaded in a Riehle PS-300, 300,000 pound tensile test machine of the Department of Aeronautics, NPS. The output of this machine is an inked curve of load vs. strain. The remaining three used bolts and two unused bolts were tested in an Instron Model TT-D 20,000 lb Tensile Tester in the NPS Material Sciences Department. This machine plots a curve of load vs. elongation. The head travel rate for both test machines was approximately 0.05 inch per minute.

Figure C1 contrasts an unused hub bolt with one which has been stretched in a tensile test. The stretched bolt was removed from the tensile tester after necking was initiated but just before fracture. The solid curve of Fig. C2 is a load-elongation curve obtained from tensile tests of a typical used hub bolt. The curve is offset from the origin by 0.185 inch, corresponding to an elongation experienced by the bolt during spin testing. A portion of the plastic deformation range has been omitted in the figure.

Two significant items of information were obtained from the solid curve of Fig. C2 and from similar curves for the other eight used bolts. First, the "knee" of this curve, and the inception of plastic behavior, defines approximately the maximum load at which bolts stretched during spin tests. This statement is based on the fact that when a conventional material such as Inconel 718 is loaded into the plastic region, unloaded, and then loaded again, the second

loading curve will follow the unloading curve until it reaches, approximately the maximum load attained during the initial loading, at which time it will curve in the direction of the initial loading curve. To verify this, there is also shown in Fig. C2 the load-elongation curve obtained from a tensile test of an unused spare bolt (broken curve). The two curves nearly coincide beyond the region of elastic deformation of the used bolt. The combination of these curves allows one to reconstruct approximately the elongation history of the bolt during spin test. Elongation increased from zero, along the broken line as rpm increased, to a load of about 6600 pounds corresponding to 6100 rpm. Then, as rpm was reduced to zero the bolt contracted down the solid line to a residual plastic deformation of 0.185 inch. The maximum load of 6600 pounds converts to an engineering stress of 86.0 ksi, the stress which produced elongation of hub bolts during spin test to 6100 rpm. (See Drawing 2011, Appendix D for hub bolt dimensions.) The other significant information available from the load-elongation curves is the ultimate tensile test bolt load. For the used bolt of Fig. C2 the maximum load is 9025 pounds, giving an engineering ultimate tensile strength of 117.3 ksi. Curves similar to those of Fig. C2 were obtained for each of the nine used bolts and for the four unused spares. A summary of the results is shown in Table C1.

Based on the demonstrated weakness of hub bolts during spin and tensile tests, the hub bolt design was modified and a new set of ten bolts was ordered for the completion of rotor testing. The major bolt modification was a nominal diameter increase from 0.313 inch to 0.323 inch. Also ordered with these bolts were two tensile test specimens manufactured from the same material as the new bolts. These specimens were tested in order to establish properties of the Inconel 718 bolt material. Drawing 2011-A of Appendix C shows dimensions of the new bolts and of the tensile specimens.

One tensile specimen was pulled in the Riehle tester as received, and the result is shown in Fig. C3. From this Fig. the material properties were calculated to be:

0.2% Yield Strength = 69.1 ksi (based on original area)

Ultimate Tensile Strength = 114.3 ksi (based on original area)

Young's Modulus = 24.3 ($10^6$) psi

Reduction in Area = 35.6%

The ultimate tensile strength and percent area reduction were noted to be nearly the same as that reported in Table C1 for the original set of bolts.

Near the end of the program, in order to establish the effect of age hardening on the bolt material, the second tensile specimen was given a heat treatment prior to tensile test. The heat treatment consisted of 10 hours at 1400°F, furnace cool to 1200°F, holding at 1200°F until total aging time was approximately 20 hours, and air cooling to ambient. The load-strain curve from this test is shown as Fig. C4. Tensile properties of the heat specimen were

0.2% Yield Strength = 142.8 ksi (based on original area)

Ultimate Tensile Strength - 185.2 ksi (based on original area)

Young's Modulus = 29.1 ($10^6$) psi

Reduction in Area = 19.4%

Therefore, the properties significantly improved over those of previous tests and verify that hub bolt material as received was in the annealed condition and required an aging heat treatment to develop its strength potential. A summary of all tensile tests and of the certified test performed by the material supplier is given in Table 3.

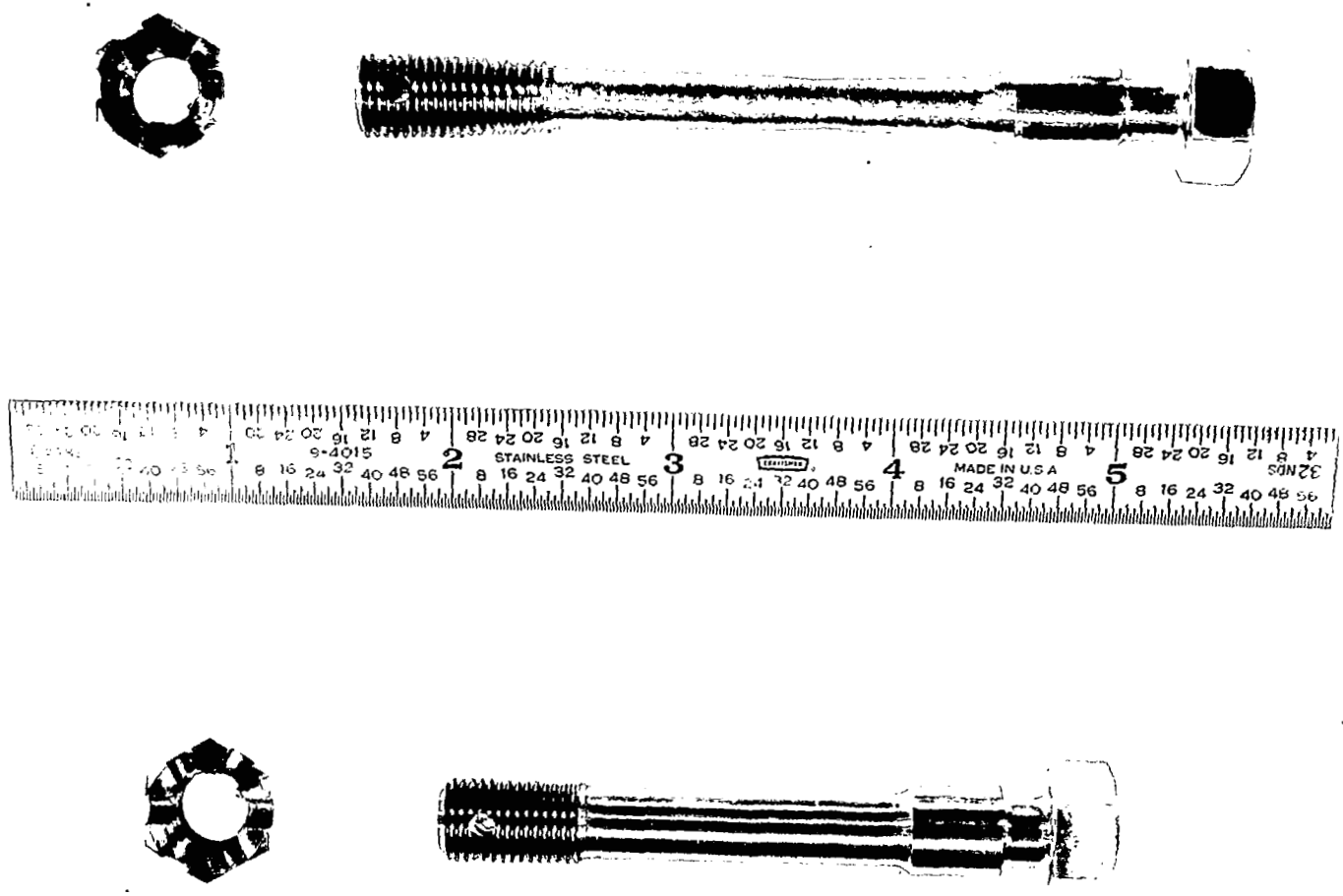


FIG. C1 COMPARISON OF HUB BOLTS BEFORE AND AFTER TENSILE TEST

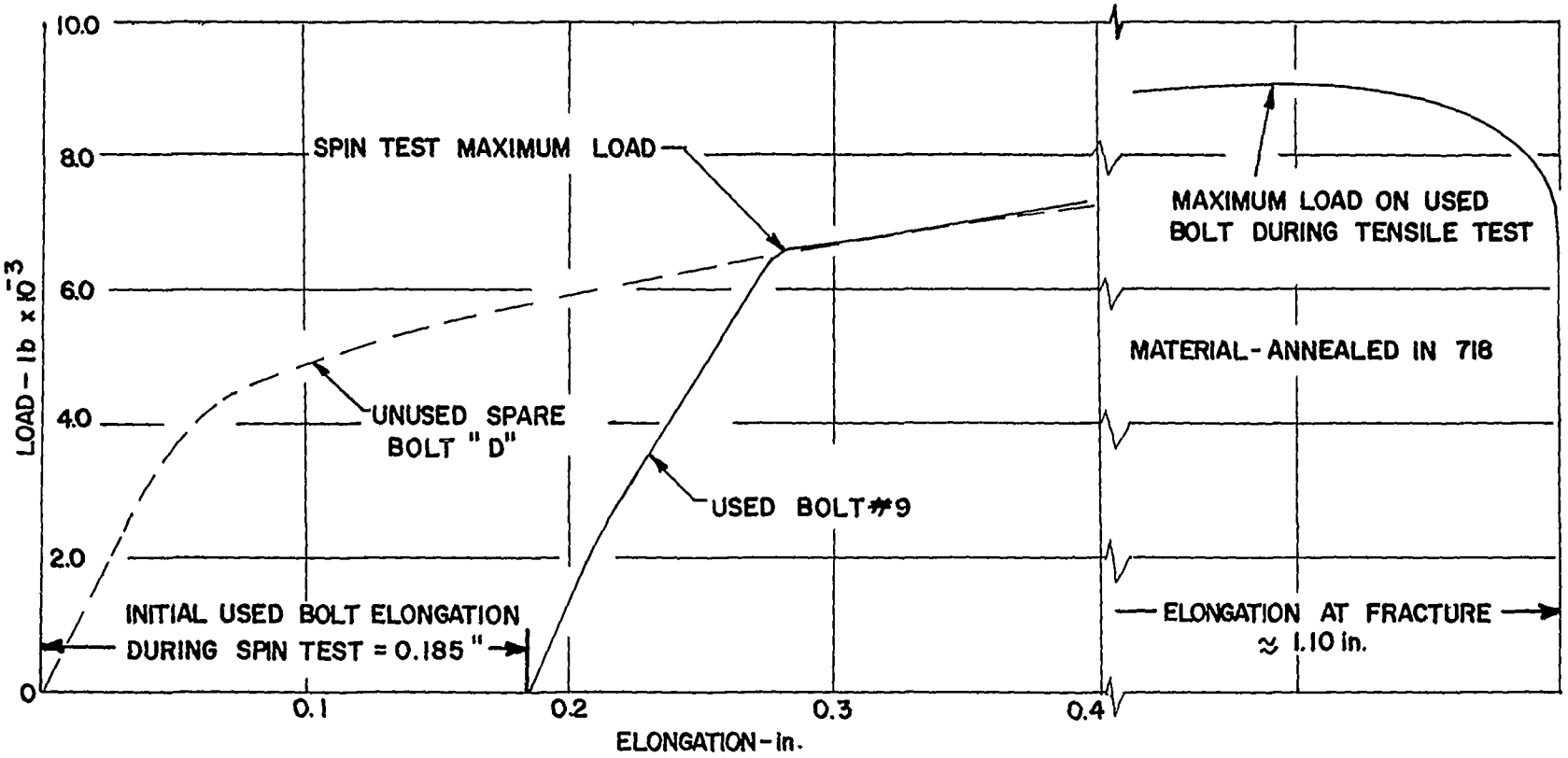


FIG. C2 LOAD-ELONGATION CURVES FROM TENSILE TESTS OF HUB BOLTS

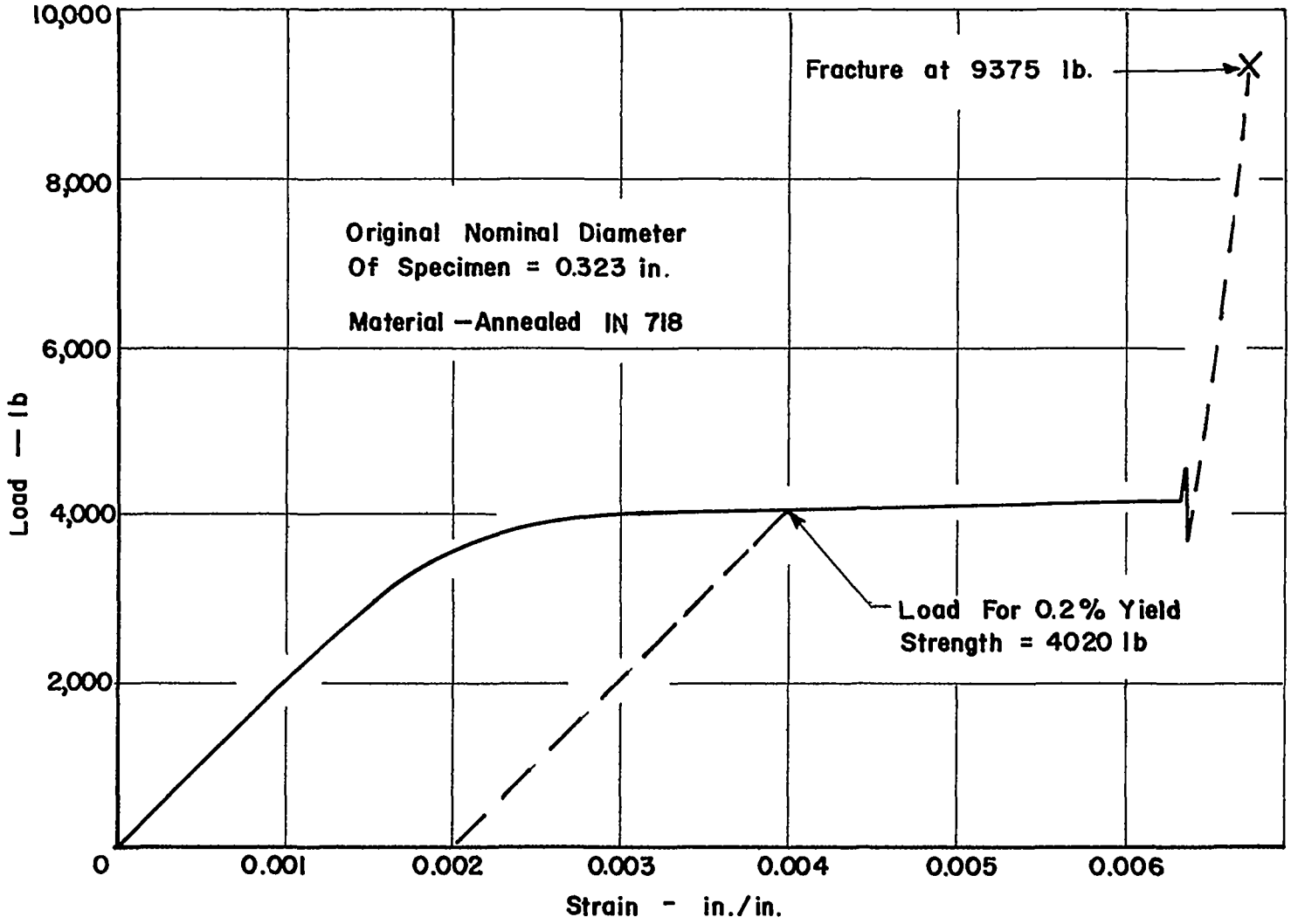


FIG. C3 LOAD-STRAIN CURVE FROM TENSILE TEST OF HUB BOLT MATERIAL SPECIMEN

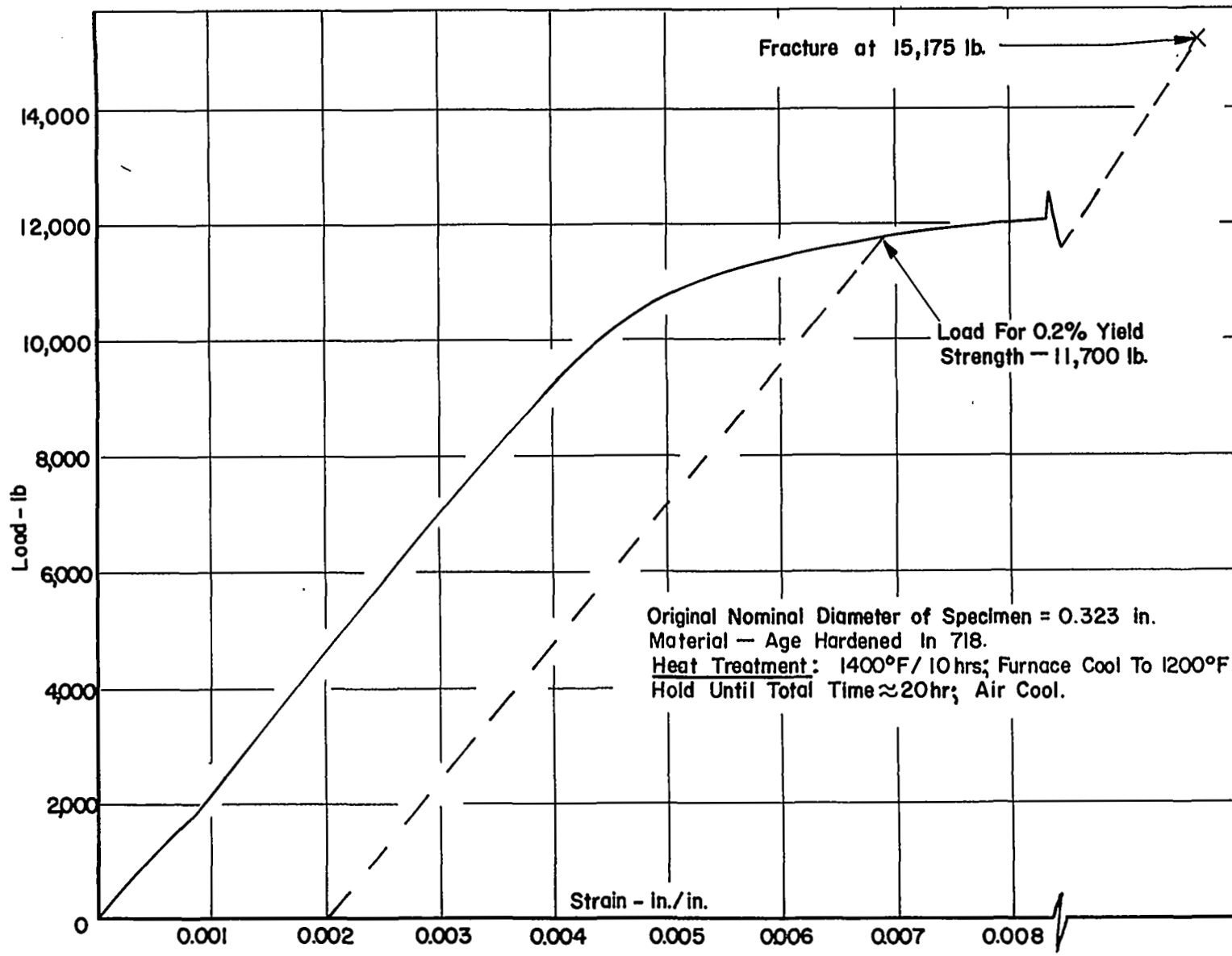


FIG. C4 LOAD-STRAIN CURVE FROM TENSILE TEST OF AGE HARDENED HUB BOLT MATERIAL SPECIMEN

| Bolt Identification | Type of Failure | Maximum Load lbs | Ultimate Tensile Strength ksi | Final Bolt Diameter in | Reduction in Area precent |
|---|---|---|---|---|---|
| Used Bolts | | | | | |
| 1 | Stripped Threads | 8550 | 111.1 | 0.262 | 29.9 |
| 2 | Stripped Threads | 8250 | 107.2 | 0.275 | 22.8 |
| 3 | Broke at cotter-pin holes | 7900 | 102.7 | 0.282 | 18.8 |
| 4 | Shaft necked down, ready to break | 8850 | 115.0 | 0.255 | 33.6 |
| 5 | No failure | 8250 | 107.2 | 0.276 | 22.2 |
| 6 | Shaft necked down, ready to break | 9075 | 117.9 | 0.255 | 33.6 |
| 7 | Broke at cotter-pin holes | 9000 | 117.0 | 0.262 | 29.9 |
| 8 | Broke at central shaft | 9100 | 118.3 | 0.256 | 33.1 |
| 9 | Broke at central shaft | 9025 | 117.3 | 0.256 | 33.1 |
| Unused Spare Bolts | | | | | |
| A | Broke at central shaft | 8975 | 116.6 | 0.255 | 33.6 |
| B | Broke at central shaft | 8850 | 115.0 | 0.259 | 31.5 |
| C | Broke at central shaft | 9080 | 118.0 | 0.255 | 33.6 |
| D | Shaft necked down, ready to break | 9000 | 117.0 | 0.253 | 34.7 |

NOTES - Ultimate tensile strength based on original bolt diameter of 0.313 in (see Drawing 2011, Appendix D).

- Load elongation charts (e.g. Figure C2) indicated that the maximum load on each bolt during the 6100 rpm test was approximately 6600 lbs.

Table C1 SUMMARY OF TENSILE TESTS ON HUB BOLTS

APPENDIX D

DRAWINGS

| Number* | Title |
|---|---|
| 2007-1 | Assembly - Upper part |
| 2007-2A | Assembly - Lower part |
| 2011-A | Disk Bolts and Nuts |
| 2015 | Drive Spindle with Nut and Lock Washer |
| 2018 | Arbor |
| 2021 | Rotor Handling Rig |
| 2022 | Balancing and Measuring Rig |

*NPS File Number

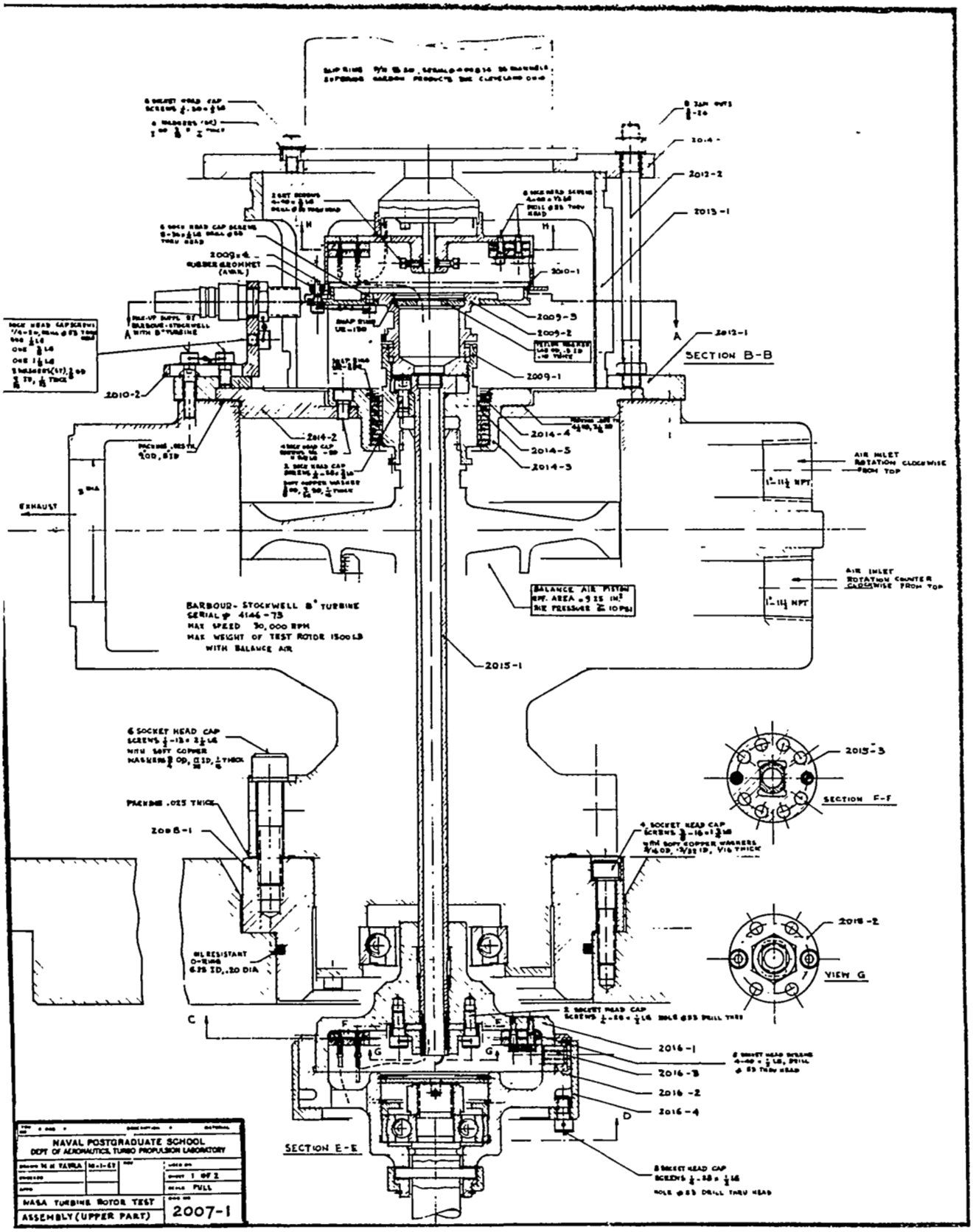
SECTION B-B
SECTION E-E
SECTION F-F
VIEW G
EXHAUST
AIR INLET ROTATION CLOCKWISE FROM TOP
AIR INLET ROTATION COUNTER CLOCKWISE FROM TOP
BARBOUR-STOCKWELL 8" TURBINE
SERIAL # 4146-73
MAX SPEED 30,000 RPM
MAX WEIGHT OF TEST ROTOR 1500 LB
WITH BALANCE AIR
BALANCE AIR PISTON
EFF. AREA = 9.25 IN²
AIR PRESSURE ≅ 10 PSI
2007-1
2009-4
2009-5
2009-2
2009-1
2010-1
2010-2
2012-1
2012-2
2013-1
2014-1
2014-2
2014-3
2014-4
2014-5
2015-1
2015-3
2016-1
2016-2
2016-3
2016-4
2018-1
2018-2
NAVAL POSTGRADUATE SCHOOL
DEPT OF AERONAUTICS, TURBO PROPULSION LABORATORY
NASA TURBINE ROTOR TEST
ASSEMBLY (UPPER PART)
2007-1
SHEET 1 OF 2
SCALE FULL

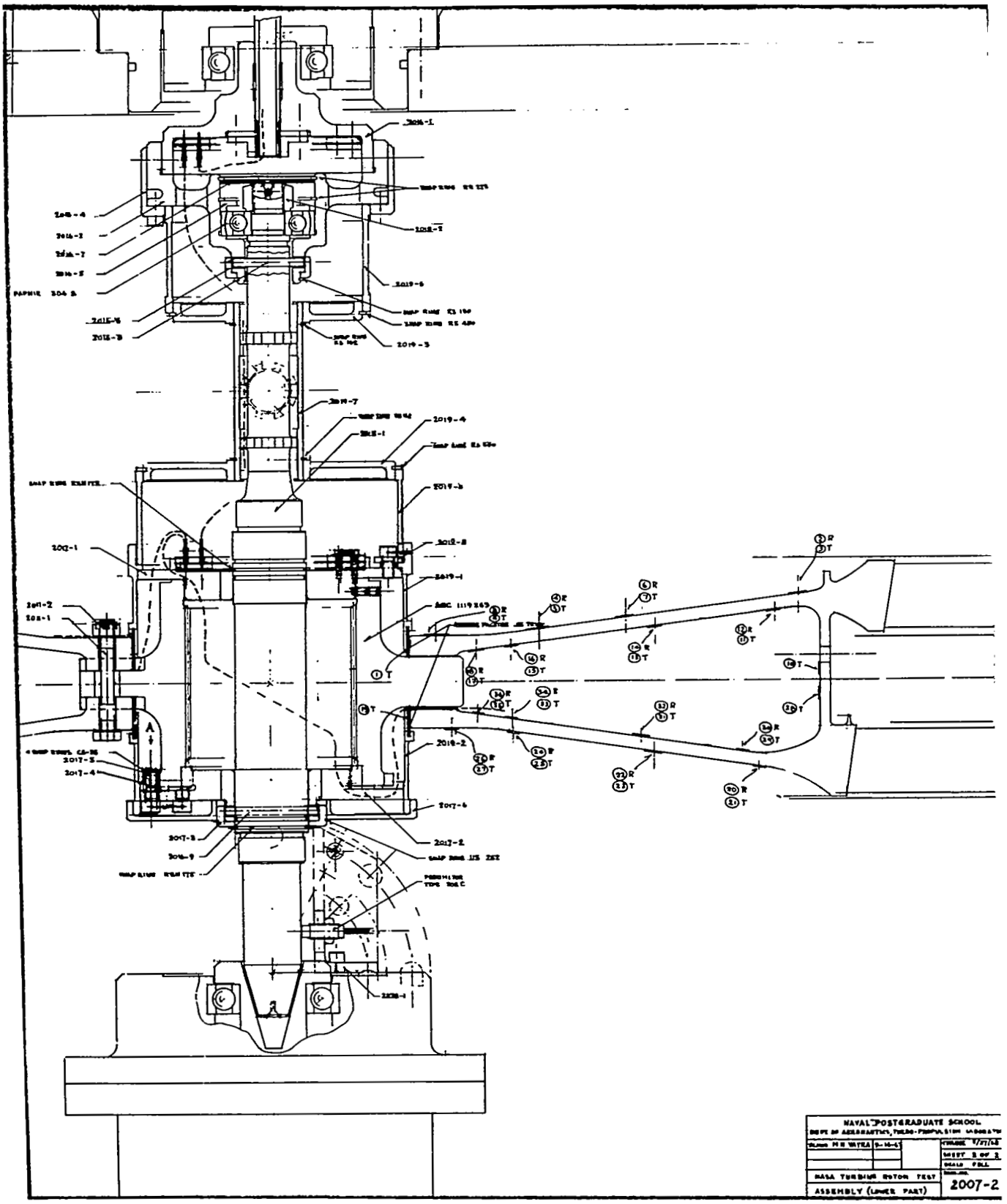
NAVAL POSTGRADUATE SCHOOL
MASA TURBINE ROTOR TEST
ASSEMBLY (LOWER PART)
2007-2

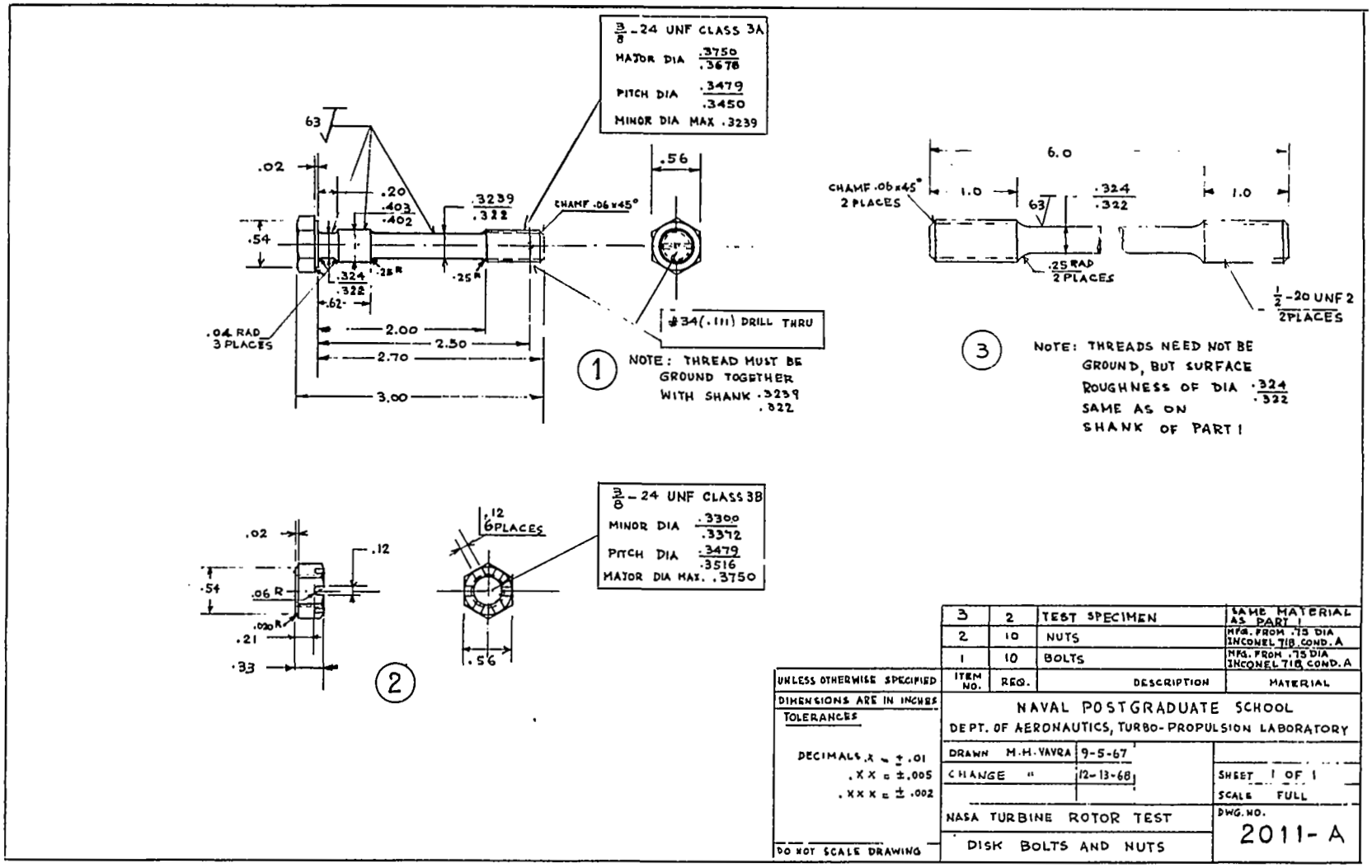


| ITEM NO. | REQ. | DESCRIPTION | MATERIAL |
|---|---|---|---|
| 3 | 2 | TEST SPECIMEN | SAME MATERIAL AS PART 1 |
| 2 | 10 | NUTS | MFG. FROM .75 DIA INCONEL 718 COND. A |
| 1 | 10 | BOLTS | MFG. FROM .75 DIA INCONEL 718 COND. A |

UNLESS OTHERWISE SPECIFIED
DIMENSIONS ARE IN INCHES
TOLERANCES
DECIMALS .X = ±.01
.XX = ±.005
.XXX = ± .002
DO NOT SCALE DRAWING

NAVAL POSTGRADUATE SCHOOL
DEPT. OF AERONAUTICS, TURBO-PROPULSION LABORATORY

DRAWN M.H. VAVRA 9-5-67
CHANGE " 12-13-68

SHEET 1 OF 1
SCALE FULL

NASA TURBINE ROTOR TEST
DISK BOLTS AND NUTS

DWG. NO. 2011-A

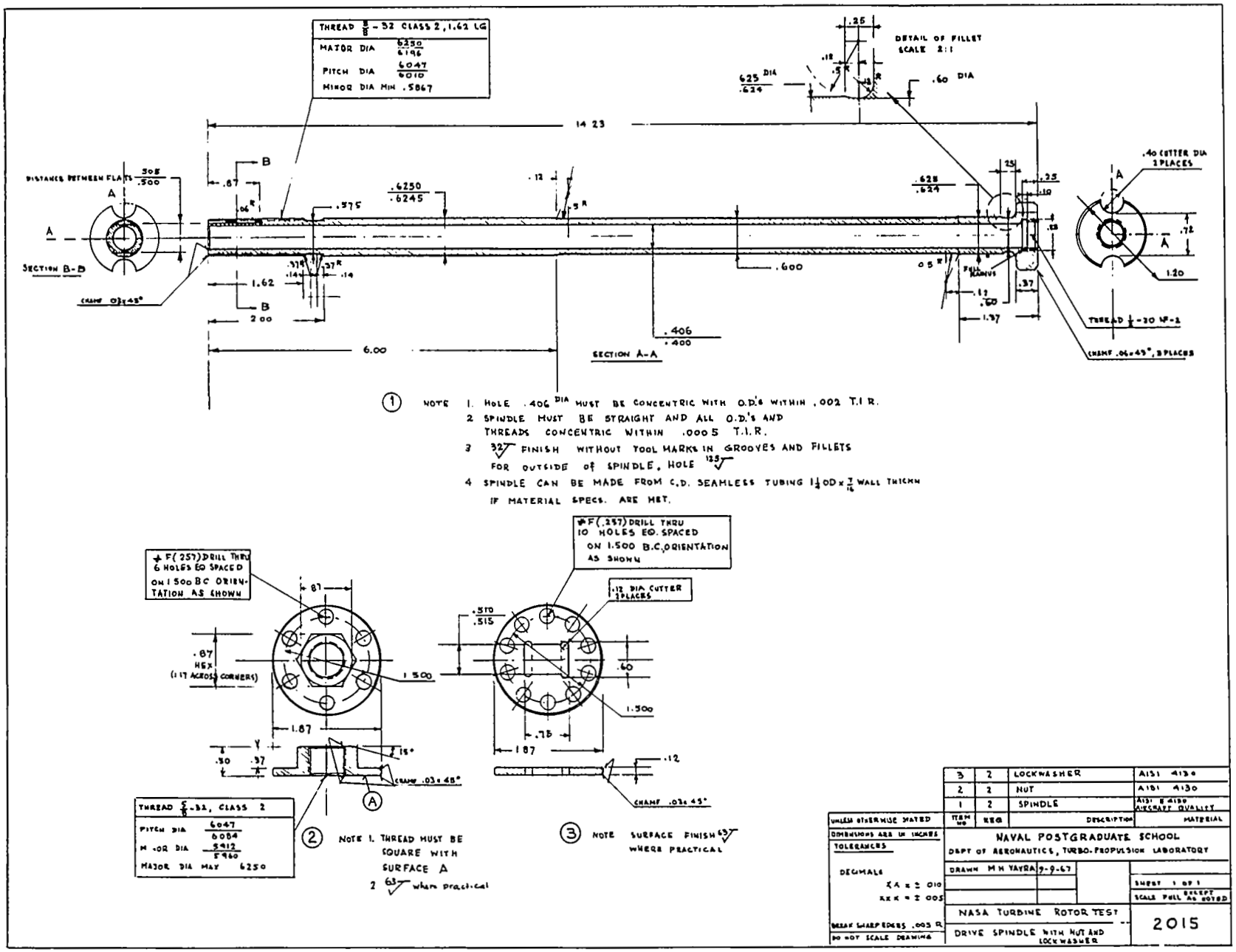
THREAD 5/8 - 32 CLASS 2, 1.62 LG
MAJOR DIA .6250 / .6196
PITCH DIA .6047 / .6010
MINOR DIA MIN .5867
DETAIL OF FILLET SCALE 2:1
.625 DIA / .624
.60 DIA
14.23
DISTANCE BETWEEN FLATS .508 / .500
.87
.06 R
.575
.6250 / .6245
.12
.5 R
.628 / .624
.25
.10
.40 CUTTER DIA 2 PLACES
.72
1.20
SECTION B-B
CHAMF .03 x 45°
1.62
2.00
.37 R
.14
.600
.05 R
FULL ROUNDS
.37
.50
1.37
THREAD 1/2 - 20 NF-2
CHAMF .06 x 45°, 3 PLACES
6.00
.406 / .400
SECTION A-A
NOTE 1. HOLE .406 DIA MUST BE CONCENTRIC WITH O.D.'s WITHIN .002 T.I.R.
2 SPINDLE MUST BE STRAIGHT AND ALL O.D.'s AND THREADS CONCENTRIC WITHIN .0005 T.I.R.
3 32 FINISH WITHOUT TOOL MARKS IN GROOVES AND FILLETS FOR OUTSIDE OF SPINDLE, HOLE 125
4 SPINDLE CAN BE MADE FROM C.D. SEAMLESS TUBING 1 1/4 OD x 7/16 WALL THICKN IF MATERIAL SPECS. ARE MET.
+F (.257) DRILL THRU 6 HOLES EQ SPACED ON 1.500 B.C. ORIENTATION AS SHOWN
+F (.257) DRILL THRU 10 HOLES EQ. SPACED ON 1.500 B.C. ORIENTATION AS SHOWN
.87
.87 HEX (1.17 ACROSS CORNERS)
1.500
.12 DIA CUTTER 3 PLACES
.510 / .515
.60
.75
15°
.30
.97
CHAMF .03 x 45°
THREAD 5/8 - 32, CLASS 2
PITCH DIA .6047 / .6084
MINOR DIA .5912 / .5960
MAJOR DIA MAX .6250
2 NOTE 1. THREAD MUST BE SQUARE WITH SURFACE A
2 63 when practical
3 NOTE SURFACE FINISH 63 WHERE PRACTICAL
3 2 LOCKWASHER AISI 4130
2 2 NUT AISI 4130
1 2 SPINDLE AISI 8 4130 AIRCRAFT QUALITY
ITEM NO | REQ | DESCRIPTION | MATERIAL
UNLESS OTHERWISE STATED
DIMENSIONS ARE IN INCHES
TOLERANCES
DECIMALS
XX ± .010
XXX ± .005
BREAK SHARP EDGES .005 R
DO NOT SCALE DRAWING
NAVAL POSTGRADUATE SCHOOL
DEPT OF AERONAUTICS, TURBO-PROPULSION LABORATORY
DRAWN M H YAYRA 9-9-67
SHEET 1 OF 1
SCALE FULL EXCEPT AS NOTED
NASA TURBINE ROTOR TEST
DRIVE SPINDLE WITH NUT AND LOCKWASHER
2015

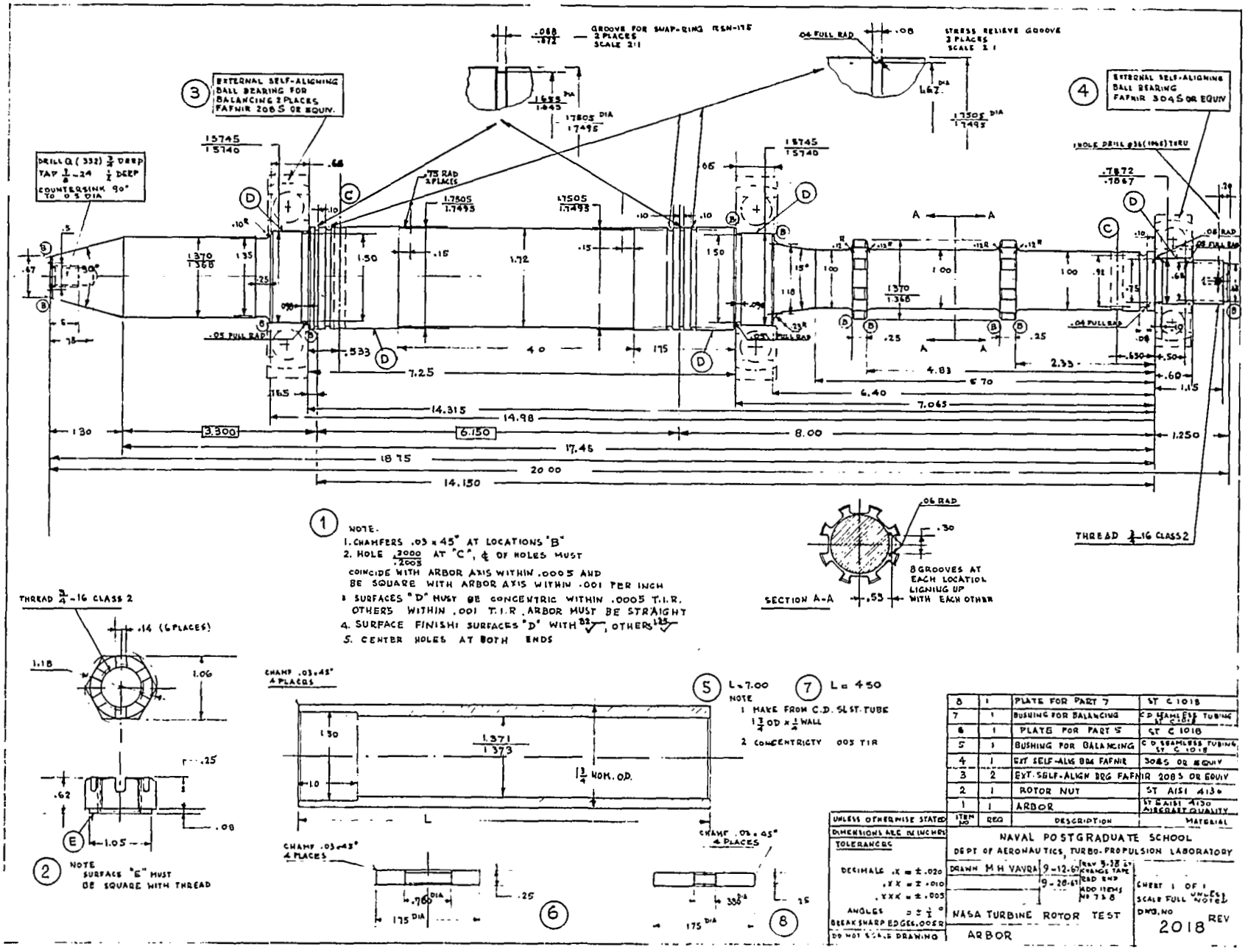


| ITEM NO | REQ | DESCRIPTION | MATERIAL |
|---|---|---|---|
| 8 | 1 | PLATE FOR PART 7 | ST C 1018 |
| 7 | 1 | BUSHING FOR BALANCING | C D SEAMLESS TUBING ST C 1018 |
| 6 | 1 | PLATE FOR PART 5 | ST C 1018 |
| 5 | 1 | BUSHING FOR BALANCING | C D SEAMLESS TUBING ST C 1018 |
| 4 | 1 | EXT SELF-ALIG BRG FAFNIR | 304S OR EQUIV |
| 3 | 2 | EXT. SELF-ALIGN BRG FAFNIR | 208S OR EQUIV |
| 2 | 1 | ROTOR NUT | ST AISI 4130 |
| 1 | 1 | ARBOR | ST AISI 4130 AIRCRAFT QUALITY |

UNLESS OTHERWISE STATED
DIMENSIONS ARE IN INCHES
TOLERANCES
DECIMALS .X = ± .020
.XX = ± .010
.XXX = ± .005
ANGLES = ± 1/2°
BREAK SHARP EDGES .005 R
DO NOT SCALE DRAWING

NAVAL POSTGRADUATE SCHOOL
DEPT OF AERONAUTICS, TURBO-PROPULSION LABORATORY

DRAWN M H VAVRA 9-12-67
REV 9-28-67 RAD END ADD ITEMS No 7 & 8
CHECKED
NASA TURBINE ROTOR TEST
ARBOR

SHEET 1 OF 1
SCALE FULL UNLESS NOTED
DWG. NO 2018 REV

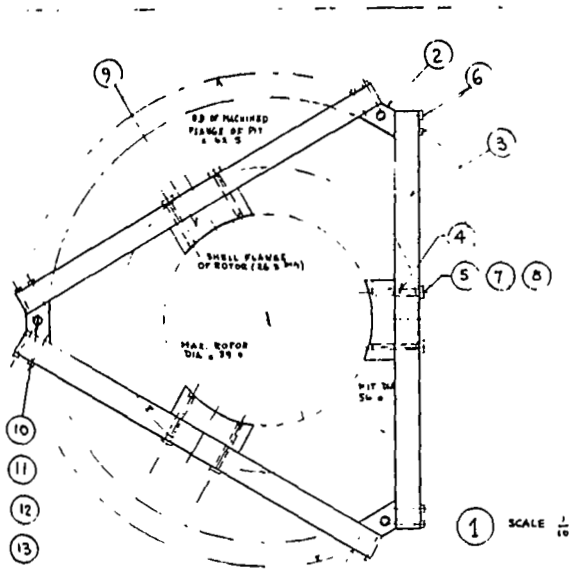


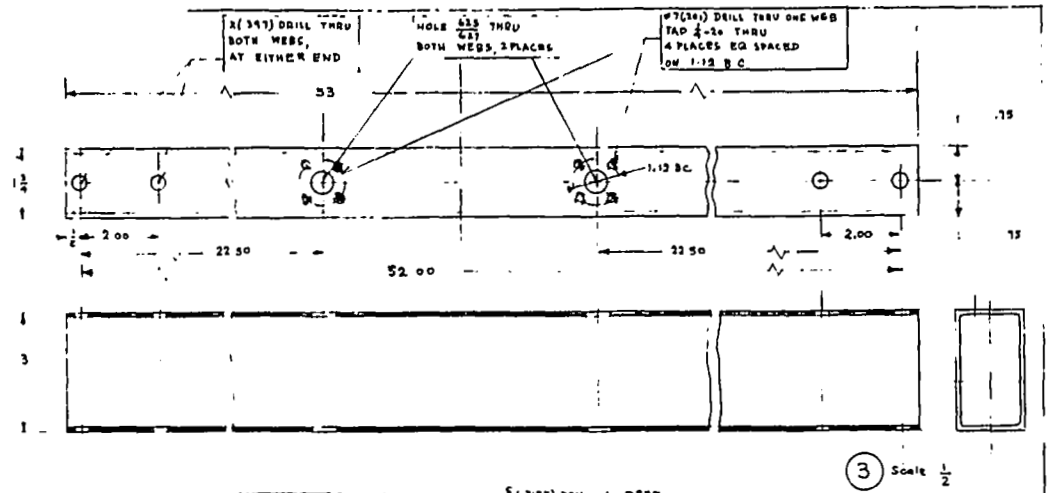


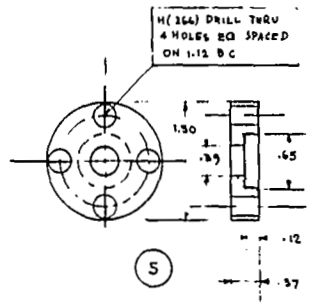


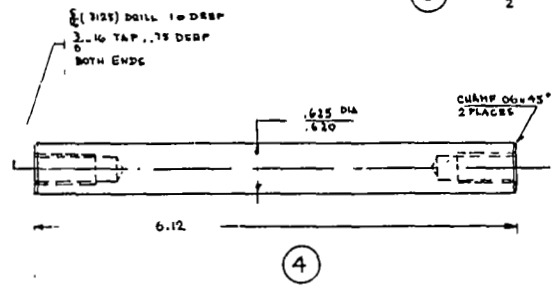


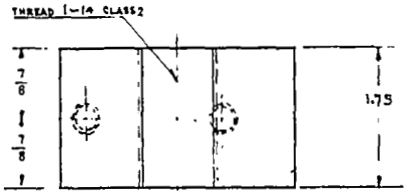


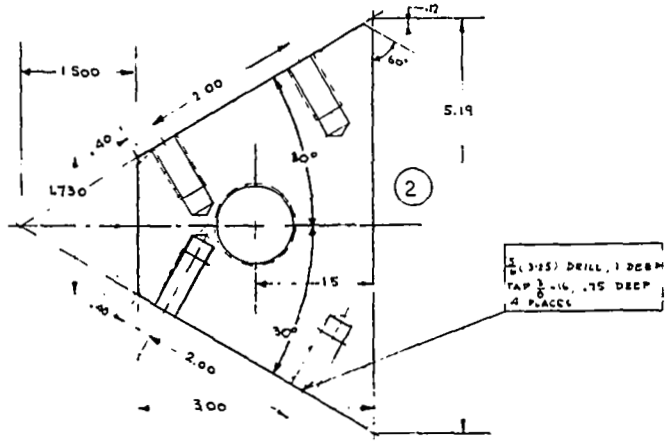


| ITEM NO | QTY | DESCRIPTION | MATERIAL |
|---|---|---|---|
| 8 | 24 | HEX SOCKET CAP SCREW 1/4 | 1/4-20 x 1/2 LG STEEL |
| 7 | 6 | HEX SOCKET CAP SCREW 3/8 | 3/8-16 x 1/2 LG STEEL |
| 6 | 12 | HEX SOCKET CAP SCREW 5/8 | 5/8-16 x 3 1/2 LG STEEL |
| 5 | 6 | FLANGE | STEEL |
| 4 | 6 | PIN | STEEL |
| 3 | 3 | BARS AL EXTRUS 1 1/2 x 3 x 1/2 | AL 6061-T6 |
| 2 | 3 | CORNERS | STEEL |
| 1 | 1 | ROTOR HANDLING RIG CONSISTING OF | |

UNLESS OTHERWISE STATED
DIMENSIONS ARE IN INCHES
TOLERANCES
FRACTIONS ± 1/16
DECIMALS .X ± .03
.XX ± .010
.XXX ± .005
ANGLES ± 1/2°
DO NOT SCALE DRAWING

NAVAL POSTGRADUATE SCHOOL
DEPT OF AERONAUTICS TURBO-PROPULSION LABORATORY
DRAWN M.H. YAYRA 9-15-67
SHEET 1 OF 2
SCALE FULL UNLESS NOTED
NASA TURBINE ROTOR TEST
DWG NO 2021-1
ROTOR HANDLING RIG

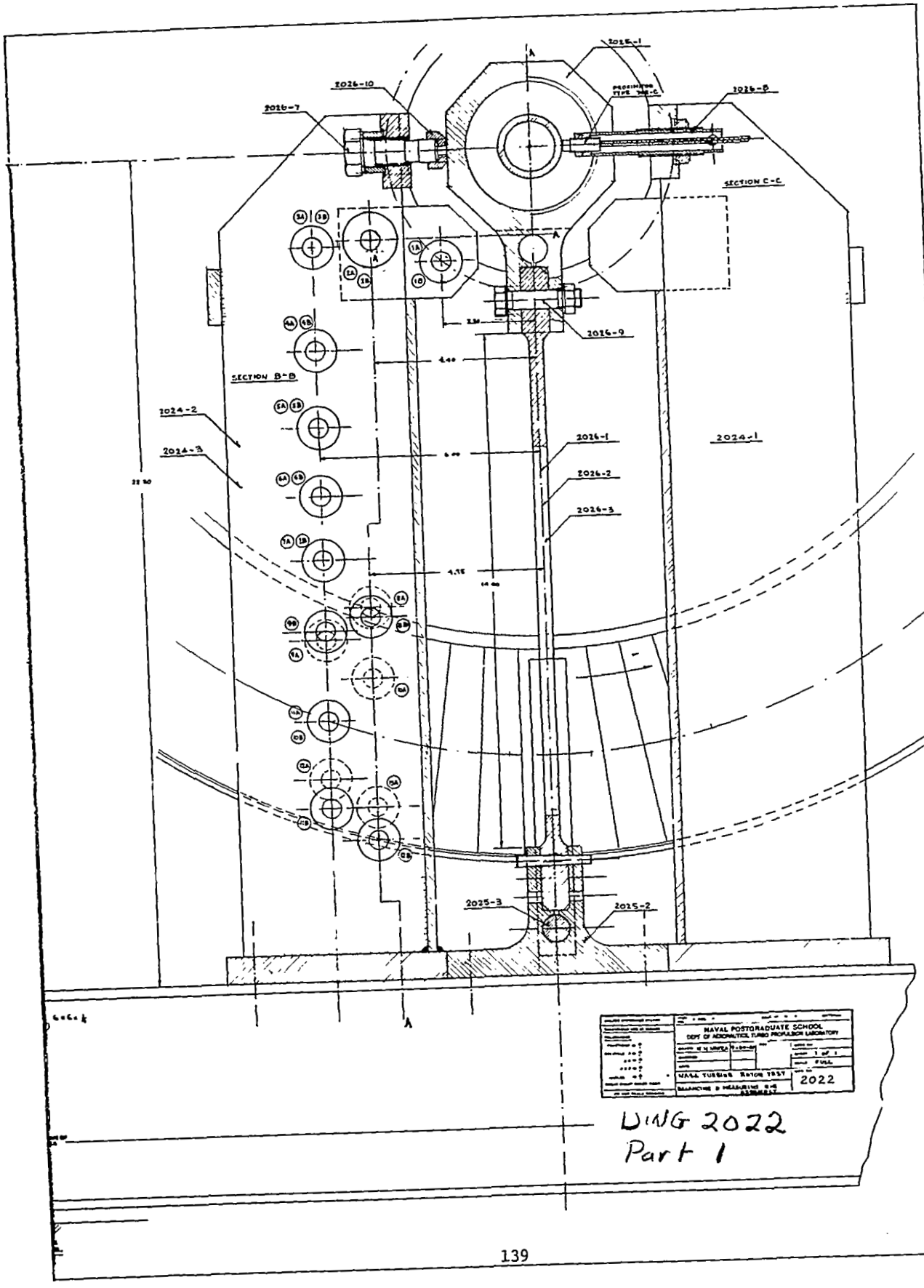


DWG 2022
Part 1

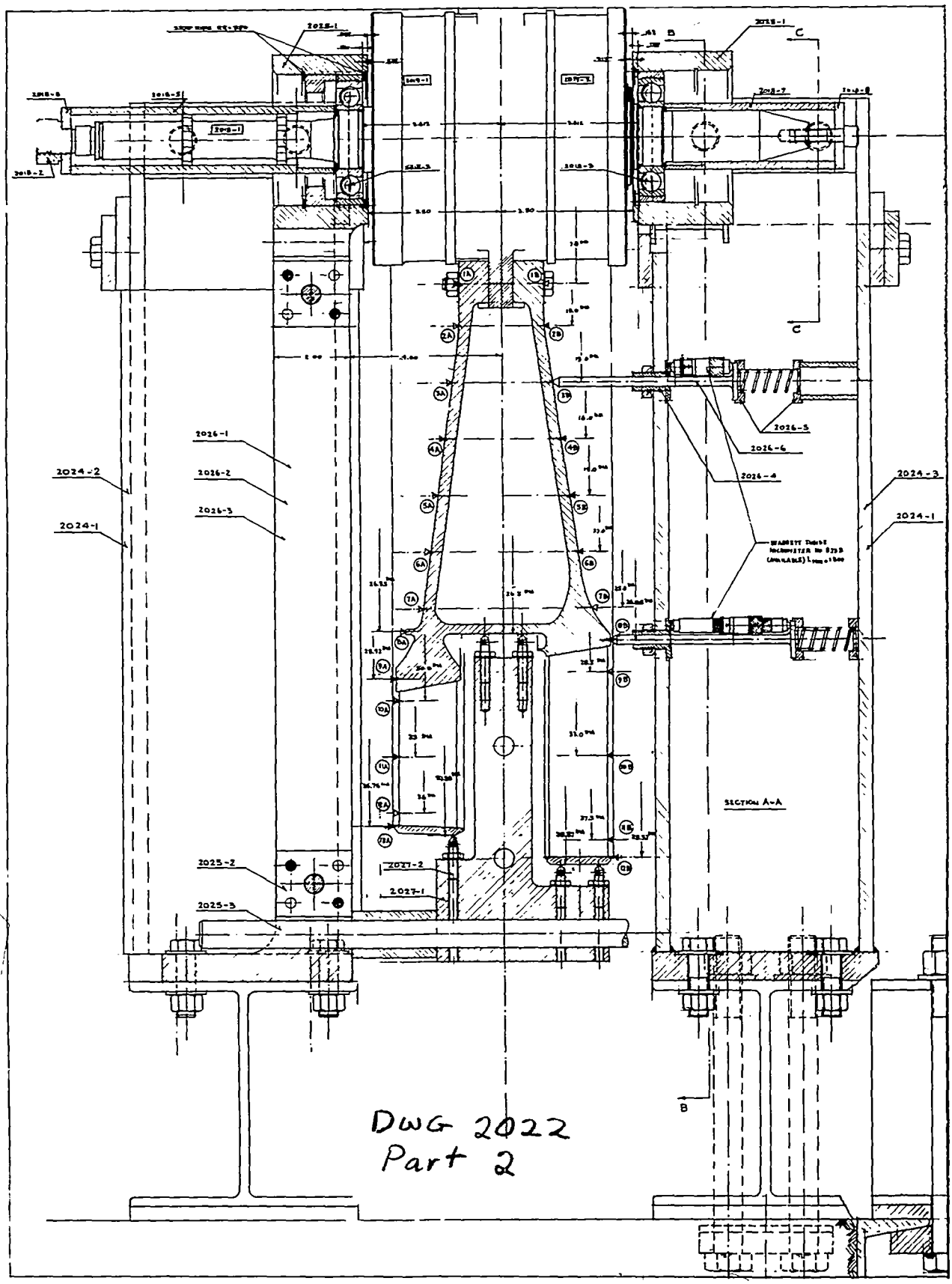


DWG 2022
Part 2



NASA-Langley, 1972 — 15 E-6629